Sound Velocities and Equation of State of iron-rich (Mg,Fe)O

Thesis by

June K. Wicks

In Partial Fulfillment of the Requirements

for the Degree of

Doctor of Philosophy

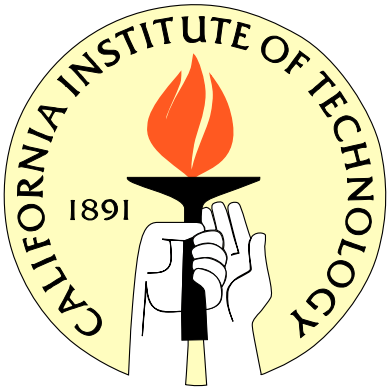

California Institute of Technology

Pasadena, California

2013

(Submitted)

Acknowledgements

First and foremost, I want to thank my advisor Jennifer Jackson. You've believed in me through this whole process, and pushed me to become a better version of myself. Under your mentorship I've grown both personally and intellectually. I wouldn't be here without you, and looking back I am amazed at how far we've come. I hope that someday I'll become as innovative and well-respected a scientist as you are today. You've been the best role model.

I am thankful to Paul Asimow and George Rossman for your friendship and mentorship, for helping me become a better teacher and a better scientist, and for always having your door open for me, even on weekends and holidays. Thank you George, for letting me hang out in the lab with you for hours at a time just for fun. Thank you Paul, for sharing your wife and kids with me, letting them be such an important part of my life.

Thank you, Mike Gurnis, for taking the time to be on my committee and including me in the CSEDI discussions. Thanks to you and Dan Bower, I could learn about and appreciate first hand the insight from dynamic models of the deep earth. This collaboration has taught me so much and has given me a different perspective on future projects.

I am grateful to Chi Ma, my mentor in the Analytical Facilities. Thanks for letting me putter around to learn the instruments, for letting me teach classes even though it was helping me more than it was helping the students, and for stepping back in and teaching me as well when I was in over my head. Thank you, John Beckett, for teaching me my way around the synthesis lab. Your thoughtful and thorough way of teaching gave me the good habits that I still have today. Thank you, Bin Chen, for the hours in the diamond anvil cell lab, teaching me the tricks you've learned along the way to make the successful cells.

I am so thankful to the great friendships that I have made, to those of you that supported me through this experience: Colette Caggiano, Lauren Edgar (roommate of 4+ years! longest relationship yet!), Melanie Channon, Andrew and Kelly Matzen, Danny and Dani Bower, Emily Hamecher, Aaron Wolf, Mike Baker, Dongzhou Zhang, Jeremy Boyce, and Jed Mosenfelder, and to the members of SSRG and secDEC, you know who you are. Thank you Kevin Lewis and John Bagert, for being my number one fans.

These measurements were made with the help of graduate students Dongzhou Zhang, Aaron Wolf, and Caitlin Murphy, post-doctorate Bin Chen and post-doctorate Hasan Yavas. At the Advanced Photon Source, thank you to my co-authors from GSECARS: Vitali Prakapenka, Kirill Zhuravlev, and Sergey Tkachev. I am particularly grateful to the nuclear resonant and inelastic X-ray scattering group: Jiyong Zhao, Tom Toellner, Ercan Alp, and especially Wolfgang Sturhahn, who has played a large role in my mentorship as well.

Support for this work was provided by the NSF-EAR 0711542 and CAREER EAR-0956166 (both awarded to JMJ) and CSEDI EAR-0855815 (awarded to MCG, DVH and JMJ). The Advanced Light Source is supported by the Director, Office of Science, Office of Basic Energy Sciences(BES), of the U.S. Department of Energy(DOE) under Contract No. DE-AC02-05CH11231. High temperature X-ray diffraction and neon loading was performed at GeoSoilEnviroCARS (Sector 13), Advanced Photon Source (APS), Argonne National Laboratory. GeoSoilEnviroCARS is supported by the National Science Foundation Earth Sciences (EAR-1128799) and Department of Energy Geosciences (DE-FG02-94ER14466). Sector 3 operations, where the nuclear resonant experiments were conducted, are partially supported by COMPRES (NSF EAR 06-49658). Use of the Advanced Photon Source was supported by the U.S. Department of Energy, Office of Science, Office of Basic Energy Sciences, under contract No. DE-AC02-06CH11357. Sample synthesis was carried out in the petrological facilities at Caltech. Microprobe analyses were carried out at the Caltech GPS Division Analytical Facility (funded in part by the MRSEC Program of the NSF under DMR-0080065).

Abstract

Ultralow-velocity zones (ULVZs) are small structures at the base of the mantle characterized by sound velocities up to 30% lower than those of surrounding mantle. In this thesis, we propose that iron-rich (Mg,Fe)O plays a key role in the observed sound velocities, and argue that chemically distinct, iron-enriched structures are consistent with both the low sound velocities and the measured shapes of ULVZs.

We have determined the room temperature Debye sound velocity (V_D) of $(Mg_{0.16}{}^{57}Fe_{0.84})O$ up to 121 GPa using nuclear resonant inelastic X-ray scattering. Using an estimate of the equation of state, the seismically relevant compressional (V_P) and shear (V_S) wave velocities were calculated from the V_Ds. We have also determined the room temperature V_D at multiple pressure points of $(Mg_{0.06}{}^{57}Fe_{0.94})O$ using nuclear resonant inelastic X-ray scattering and in-situ X-ray diffraction up to 80 GPa. The effect of the electronic environment of the iron sites on the velocities of both of these studies were tracked in-situ using synchrotron Mössbauer spectroscopy. We also present the pressure-volume-temperature equation of state of $(Mg_{0.06}{}^{57}Fe_{0.94})O$ determined up to pressures of 120 GPa and temperatures of 2000 K. We combine these studies with a simple Voigt-Reuss-Hill mixing model to predict the properties of a solid ULVZ and show that a small amount of iron-rich (Mg,Fe)O can greatly reduce the average sound velocity of an aggregate assemblage. When combined with a geodynamic model of a solid ULVZ (*Bower et al.*, 2011), we can directly correlate inferred sound velocities to mineralogy and predicted ULVZ shapes. Our combined geodynamic and mineral physics model of a solid ULVZ can be used to explore the relationship between the observed sound velocities and mineralogy of ULVZs with added insight into ULVZ morphology.

Contents

List of Figures

List of Tables

Chapter 1

Introduction

Study of the interior of the earth is crucial to understanding both the processes by which a planet was formed and the future impact of deep interior dynamics.

Much has been learned from seismic studies, probing the propagation of sound waves through the earth. Seismic reflectors deep in the earth such as those located at 410, 660 and 2900 km below the earth's surface have been interpreted as chemical boundaries or phase changes, supported by experimental studies of model compositions of primitive mantle material. The major discontinuities in the mantle are believed to correspond to phase changes, where olivine transforms to the high pressure polymorph wadsleyite at the 410 km discontinuity, then breaks down to form ferropericlase and perovskite at the 660 discontinuity (e.g. *Irifune*, 1994, Figure 1.1).

The mantle layer between the core-mantle boundary and the D" discontinuity spans a depth range in Earth's lower mantle from up to 350 km above the liquid outer core to the outer core itself, corresponding to a proposed temperature range of 3300-4300 K and 115 to 135 GPa. Intermittent detection of this discontinuity suggests that the core-mantle boundary (CMB) layer is compositionally distinct and/or represents a different phase assemblage (e.g. *Lay et al.*, 2008; *Sidorin et al.*, 1999).

1.1 Ultralow-Velocity Zones

At the base of the D" layer, 5-20 km thick patches have been observed in which the V_P and V_S sound velocities are reduced by 5-10% and 10-30% (*Thorne and Garnero*, 2004). Reduced seismic

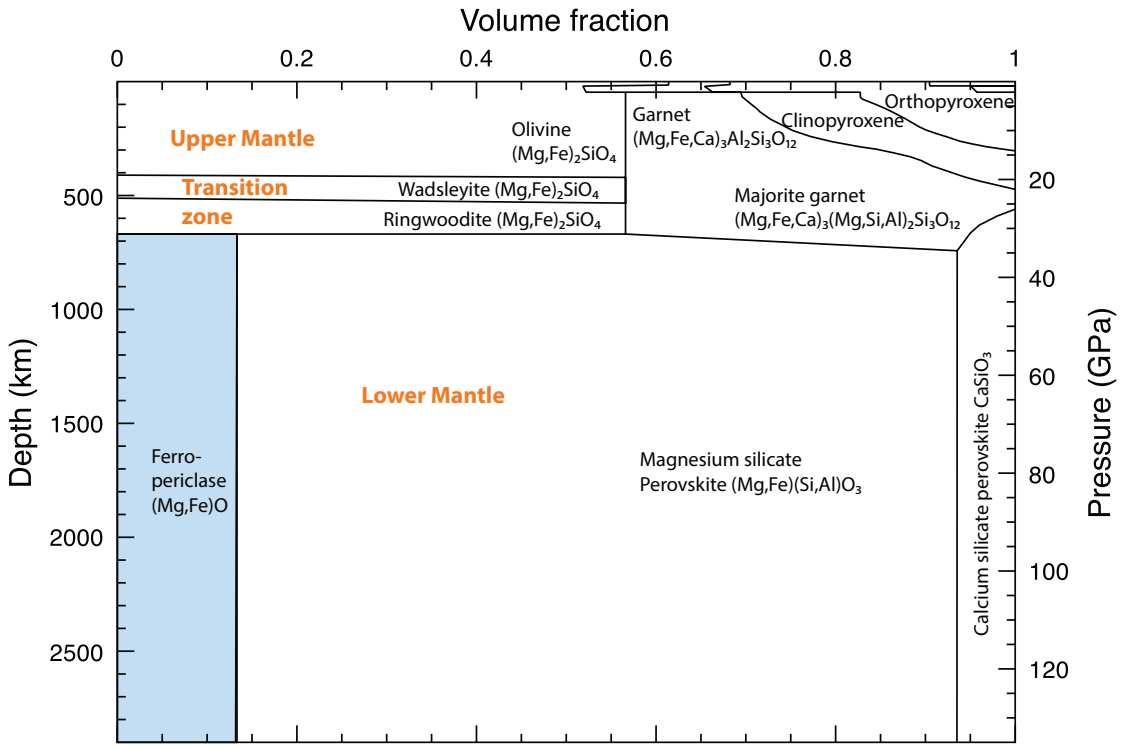

Figure 1.1: Modal mineralogy of the earth's mantle, assuming a pyrolite mantle. The upper mantle (0-440 km below the earth's surface) is mostly comprised of olivine garnet, and pyroxenes $(Mg,Fe)_2Si_2O_6$. The lower mantle (660 to 2900 km below the earth's surface) is comprised of Ca- and (Mg,Fe)- silicate perovskite and (Mg,Fe)O. Highlighted in blue is ferropericlase, the Fe-poor member of the MgO-FeO solid solution. Iron-rich members are named magnesiowüstite. Figure is adapted from (*Frost et al.*, 2004)

velocities in this ultra-low velocity zone, or ULVZ, were first attributed to partial melting due to drastic velocity reductions, sharp upper boundaries, and a strong correlation with hot spots on the surface (e.g. *Williams and Garnero*, 1996; *Williams et al.*, 1998; *Lay et al.*, 2004). A sound velocity decrement ratio $\partial V_P/\partial V_S$ of 1:3 has been shown to be consistent with partial melt (*Berryman*, 2000).

Numerous seismic studies of the core-mantle boundary indicate that ULVZ distribution is patchy and sometimes associated with edges or the interior of large low shear velocity provinces (*McNamara et al.*, 2010). Fine-scale one-dimensional structure of some ULVZs have been probed, finding a steep positive velocity gradient with depth, implying complex interior morphology (*Rost et al.*, 2006). Multiple concave-down ULVZs clustered together have been invoked to explain PKP precursors in

a two-dimensional study, giving the first seismic insight into ULVZ shape (*Wen and Helmberger*, 1998).

Partial melting of ambient mantle would require the fortuitous intersection of the mantle solidus with the base of the core-mantle boundary. Recent work into the equations of state of fayalite Fe_2SiO_4 liquid and subsequent analysis shows that partial melting of chondrite or peridotite liquid is unlikely to be gravitationally stable at the base of the mantle (*Thomas et al.*, 2012). It has been proposed that enriched residues of a crystallizing mantle could be depleted in Si and enriched in FeO enough to form ULVZs (*Labrosse et al.*, 2007; *Nomura et al.*, 2011).

Dynamic studies exploring the stability of partially-molten ULVZs show that the amounts of liquid required to reduce the velocities of an assemblage would percolate and pool at the base of the mantle rather than remain suspended in a ULVZ (*Hernlund and Tackley*, 2007). Partial melt can be maintained km's above the CMB if the ULVZ is stirred (*Hernlund and Jellinek*, 2010). Further studies of melt geometry explore mechanisms to retain greater melt fraction (*Wimert and Hier-Majumder*, 2012; *Hier-Majumder and Abbott*, 2010, e.g.). In the end, a seemingly simple explanation is complicated by large unknowns in grain boundary properties, melt viscosity, and melt sound velocities.

Solid ULVZs have also been considered in the literature, in the form of FeO/FeSi alloy (*Manga and Jeanloz*, 1996) or iron-enriched post-perovskite (*Mao et al.*, 2006), but are no longer considered stable in the hot core-mantle boundary regions in which ULVZs are found. In this thesis, we introduce and explore another alternative: iron-rich (Mg,Fe)O.

The partitioning behavior of iron between perovskite(Pv), post-perovskite(PPv), and (Mg,Fe)O varies widely based on experimental conditions. Recently, it has been suggested that iron preferentially partitions in (Mg,Fe)O in the presence of Pv and PPv based on analyses of quenched phase assemblages from pressures and temperatures of 100 GPa and ∼1800 K (*Auzende et al.*, 2008; *Sinmyo et al.*, 2008). An enhanced iron content and subsequent uptake by (Mg,Fe)O could result in a composition much more iron-rich than previously considered. Therefore, it is of interest to study the elasticity of iron-rich (Mg,Fe)O at core-mantle boundary conditions, as it may shed light on seismic

observations in this region.

1.2 Thesis Overview

This thesis is divided into three studies of iron-rich oxide, the experiments for which are summarized in Table 1.1. All of these studies are united by the use of X-ray scattering techniques using synchrotron radiation to measure the elasticity of iron-rich (Mg,Fe)O. We synthesized our own samples for this study, and describe the samples in Section A.1. Using a diamond anvil cell to create pressures approaching those of the core-mantle boundary and occasionally in-situ laser heating to create temperatures approaching those of the earth's interior, we measured material properties relevant to the study of the earth's mantle, namely sound velocities and densities.

Chapter 2 is a study of $(Mg_{.16}Fe_{.84})O$ using nuclear resonant inelastic X-Ray scattering (NRIXS) and synchrotron Mössbauer spectroscopy (SMS). Chapter 3 measured the sound velocities and magnetic state of $(Mg_{.06}Fe_{.94})O$ using the methods described in Chapter 2 with a few key differences, including the use of in-situ X-ray diffraction to measure lattice spacing of the sample and map it directly to a combined XRD/SMS study of the same material. Chapter 4 describes the P-V-T equation of state of $(Mg_{.06}Fe_{.94})O$. Finally, we close in Chapter 5 with a mixing model that combines the results of our work with dynamic calculations of a solid ULVZ.

Chapter	beamlines	beamtime dates	information collected	P-T conditions	samples
2	APS 3-ID-B	10/08, 7/09	NRIXS, in-situ SMS	300 K, 0-121 GPa	Mw84
	ALS 12.2.2	4/09	XRD	300 K, 0 GPa	Mw84
3	APS 3-ID-B	8/11, 10/12	NRIXS, in-situ SMS	300 K, 0-81 GPa	Mw94
	APS 3-ID-B	2/13	SMS with in-situ XRD	300 K, 8-52 GPa	Mw94
4	APS 13-ID-D	7/11	XRD	300-1950 K, 32-120 GPa	Mw94
	APS 13-ID-D	2/12	XRD with Fe buffer	300-1800 K, 30-70 GPa	Mw94
A.3	APS 3-ID-B	8/11, 3/12	NRIXS	300 K, 0-100 GPa	FeO
	ALS 12.2.2	5/11	XRD	300 K, 0 GPa	FeO
	APS 13-ID-D	2/12	XRD	300 K, 100 GPa	FeO

Table 1.1: Summary of experiments presented in this thesis

Chapter 2

Sound velocities of $(Mg_{0.16}Fe_{0.84})O$ measured by Nuclear Resonant Inelastic X-Ray Scattering*

* *This chapter has been previously published as: Wicks, J. K., J. M. Jackson, and W. Sturhahn (2010), Very low sound velocities in iron-rich (Mg,Fe)O: Implications for the core-mantle boundary region, Geophys. Res. Lett., 37, L15304. A re-evaluation of this data is briefly discussed in Chapter 5*

2.1 Nuclear Resonant Scattering

Nuclear resonant scattering (NRS) methods take advantage of the fact that nuclei, much like electrons, can be excited into higher energy states, which are organized into discrete energy levels. A resonance energy is the energy that corresponds to the excitation of a nucleus into one of these higher energy levels, at which energy the absorption cross-section of the nucleus is much higher. Whether a nucleus is accessible for nuclear resonant studies is a function of both nuclear excitation energy and lifetime of the excited state. We refer the reader to references such as *Sturhahn* (2004) that introduce the spectroscopy technique and *Sturhahn* (2000) that describes the software. In addition, *Sturhahn and Jackson* (2007) discusses NRS techniques in the context of geophysical application.

2.1.1 Nuclear Resonant Inelastic X-Ray Scattering (NRIXS)

Nuclear resonant inelastic X-ray scattering (NRIXS) is a technique that probes the lattice vibrations in which the resonant atoms participate. It is complementary to techniques such as Raman spectroscopy and infrared spectroscopy in that it measures vibrations of a lattice, but differs in both information and execution. Most notably, there are no selection rules for NRIXS, so no vibrations are missed based on symmetry. However, because it is isotope-specific, the vibrations measured are a projection of lattice vibrations onto the resonant isotope.

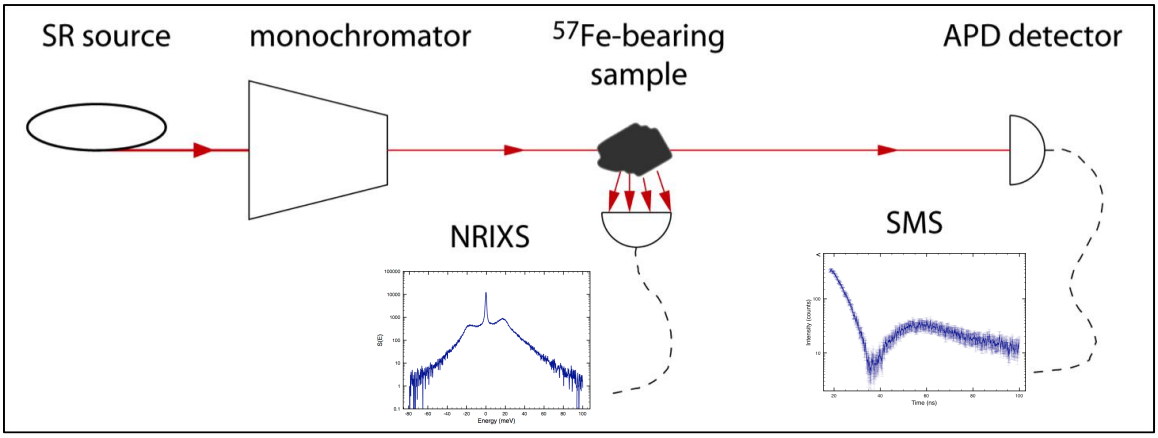

Figure 2.1: Setup of Nuclear Resonant Scattering measurements at Sector 3-ID-B of the Advanced Photon Source. Figure adapted from (*Sturhahn and Jackson*, 2007).

Figure 2.1 shows a cartoon of the setup of nuclear resonant scattering measurements at Sector 3-ID-B of the Advanced Photon Source (APS). The synchrotron radiation (SR) of the APS is a third-generation light source capable of producing X-rays with high flux and brilliance. In Sector 3 of the APS a series of monochromators eliminate all energies except the resonance energy with a 1 meV bandwidth. In the case of ^{57}Fe, the resonance energy is 14.4125 keV, and the energies corresponding to inelastic scattering are obtained by tuning the energy around the resonance peak. Incoherent scattering is measured radially as close to the sample as possible using avalanche photodiodes detectors (APDs), and produce the NRIXS spectra. Coherent scattering is measured in the forward direction, further downstream, which gives us the shape of the elastic peak, which reflects the source, and the synchrotron Mössbauer spectrum if measured in the time domain.

Figure 2.2 shows an example energy scan collected in an NRIXS experiment. The elastic peak

at the origin corresponds to recoilless absorption and emission. Peaks on either side of the elastic peak correspond to phonon annihilation (anti-Stokes) or creation (Stokes). The spectrum measured in the forward direction gives the shape of the elastic peak, and is scaled and subtracted from the NRIXS spectrum to isolate the vibrations.

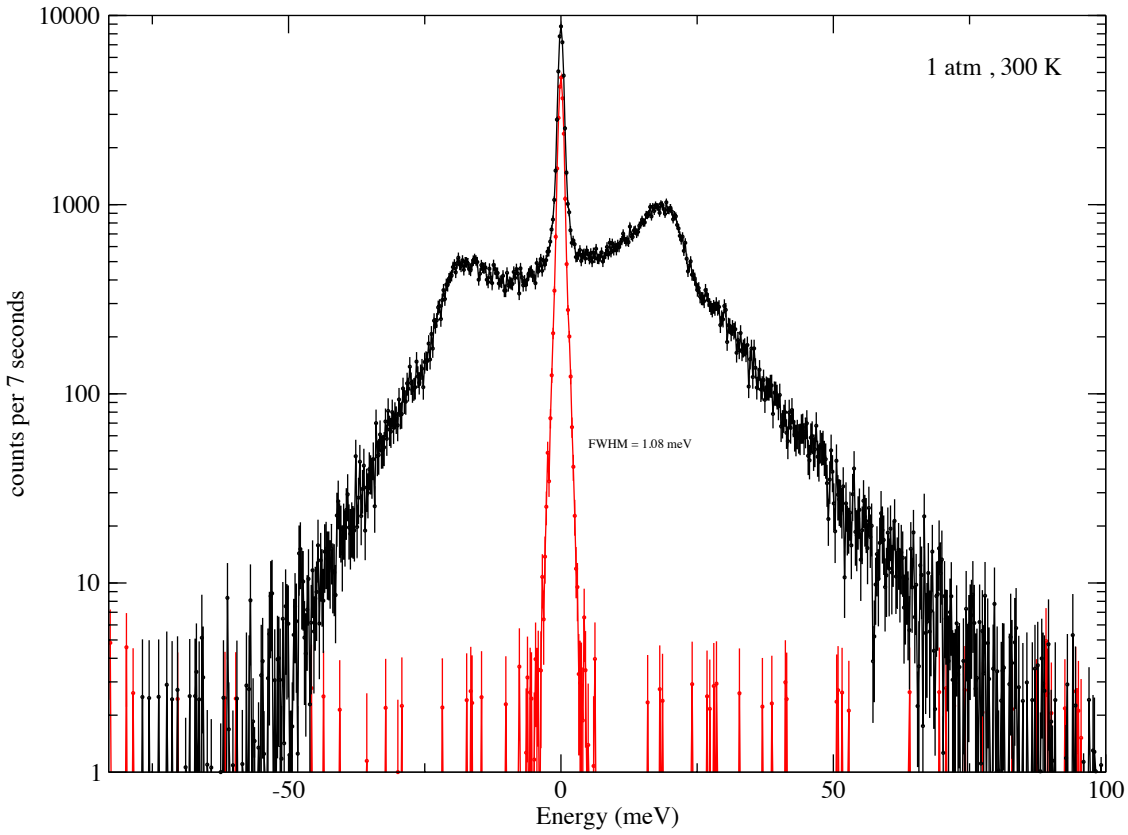

Figure 2.2: Sample energy scan (raw NRIXS spectrum) of $(Mg_{.06}Fe_{.94})O$ around the ^{57}Fe resonance energy of 14.4125 keV at ambient pressure and temperature. The spectrum independently measured in the forward direction gives the shape of the elastic peak (red). The spectrum measured radially captures the inelastic absorptions corresponding to lattice vibrations (black).

2.1.2 Synchrotron Mössbauer Spectroscopy (SMS)

Mössbauer spectroscopy measures small changes to nuclear energy levels in response to its environment. From this technique, we gain information about the electronic and magnetic environment of a nucleus that has an accessible resonance (e.g. ^{57}Fe).

Nuclear energy levels are sensitive to the electric field gradient, which couples with the quadrupole

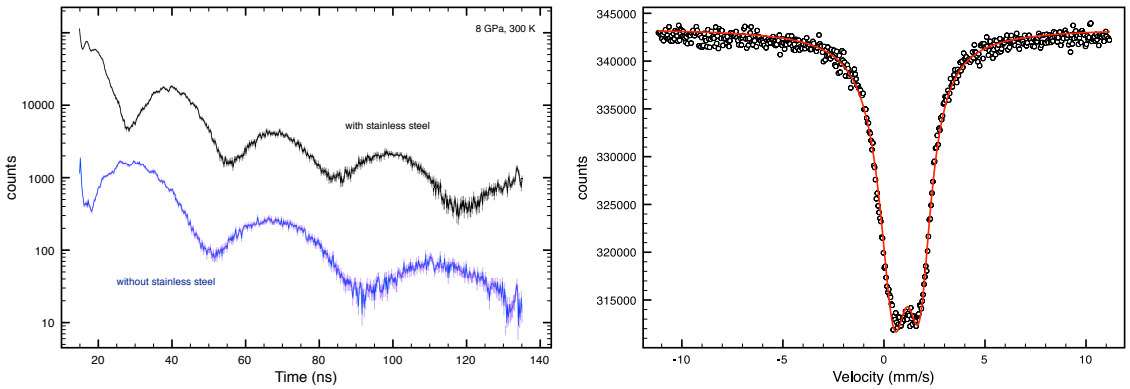

Figure 2.3: Left: Synchrotron Mössbauer spectra of $(Mg_{.06}Fe_{.94})O$ at 8 GPa, with and without stainless steel reference. Right: Conventional Mössbauer spectrum of $(Mg_{.06}Fe_{.94})O$ at 0 GPa, with a fit drawn in red corresponding to a quadrupole splitting of 1 mm/s and isomer shift of 0.8 mm/s, consistent with divalent iron.

moment of the nucleus. An asymmetric electronic distribution around the nucleus, then, results in quadrupole splitting. Nuclear energy levels split even further in the presence of electric or magnetic fields. Synchrotron Mössbauer spectroscopy measures the Rayleigh scattering of excited resonant nuclei, where a superposition of different emitted energies reflecting nuclear level splitting can be measured using detectors as a function of time.

Figure 2.3 shows an example of typical Mössbauer spectra of $(Mg_{.06}Fe_{.94})O$ at low pressures. Higher pressure data is discussed in Chapter 3. A quadrupole splitting of energy manifests as a split peak in conventional spectra (right), and as an oscillational frequency in synchrotron Mössbauer spectra (left). In conventional spectra, the isomer shift measured gives the energy shift of the ground energy level with respect to the gamma ray source, typically ^{57}Co embedded in stainless steel. In synchrotron Mössbauer spectroscopy, isomer shift is determined by measuring a sample twice, with and without a reference absorber in the beam. Advantages of synchrotron Mössbauer spectroscopy over conventional methods include no source broadening, no background, and high photon flux at the resonance energy of the ^{57}Fe atom, permitting high quality spectra with reasonable count times of samples even at high pressure.

2.2 Experiments and Data Evaluation

The $(Mg_{.16}{}^{57}Fe_{.84})O$ sample was synthesized at room pressure in a gas-mixing furnace. Details of synthesis and purity can be found in section A.1. Three panoramic diamond anvil cells (DACs) were prepared for this experiment. The panoramic DACs were designed and machined at Caltech. Beveled anvils with 250 and 300 μm-flat culet diameters were used. A 140 μm sample chamber was drilled out of a pre-indented beryllium gasket for each DAC, and the sample was loaded in the center of a boron epoxy insert to increase sample thickness, aid in gasket stability, and reduce pressure gradients. In one of the three DAC setups, a NaCl pressure medium was included with the sample, and no boron epoxy was used. Small ruby spheres were loaded close to the sample in all DACs to determine pressure before and after data collection using the characteristic ruby fluorescence line shift according to the non-hydrostatic ruby pressure scale (*Mao et al.*, 1978).

High-pressure nuclear resonance scattering experiments were conducted at Sector 3-ID-B of the Advanced Photon Source at Argonne National Laboratory (*Sturhahn and Jackson*, 2007, Figure 2.1). The storage ring was operated in top-up mode with 24 bunches separated by 153 ns. The X-ray energy incident on the sample had a bandwidth of 1.2 meV and was tuned around the 14.4125 keV nuclear resonance of ^{57}Fe (*Toellner et al.*, 2001). Time-delayed photons resulting from nuclear excitation of the ^{57}Fe isotope in $(Mg_{.16}Fe_{.84})O$ were collected using three avalanche photodiode detectors (APDs) positioned radially around the DAC. At each pressure, inelastically scattered photons were collected over select energy ranges spanning -80 meV to +100 meV. Nuclear resonance inelastic X-ray scattering (NRIXS) spectra were collected from ambient pressure to 121 GPa at 300 K. Raw spectra are shown in Figure 2.4.

From the measured energy spectra, the partial projected phonon density of states (PDOS) pertaining to the Fe site was extracted using methods described in (*Sturhahn*, 2004). PDOSs are shows in Figure 2.5.

A fourth APD was positioned in the forward direction with two goals: 1) to measure the resolution function independently for accurate sound velocity determination and 2) to measure the time spectra using synchrotron Mössbauer spectroscopy for local magnetic environment determination of the ^{57}Fe

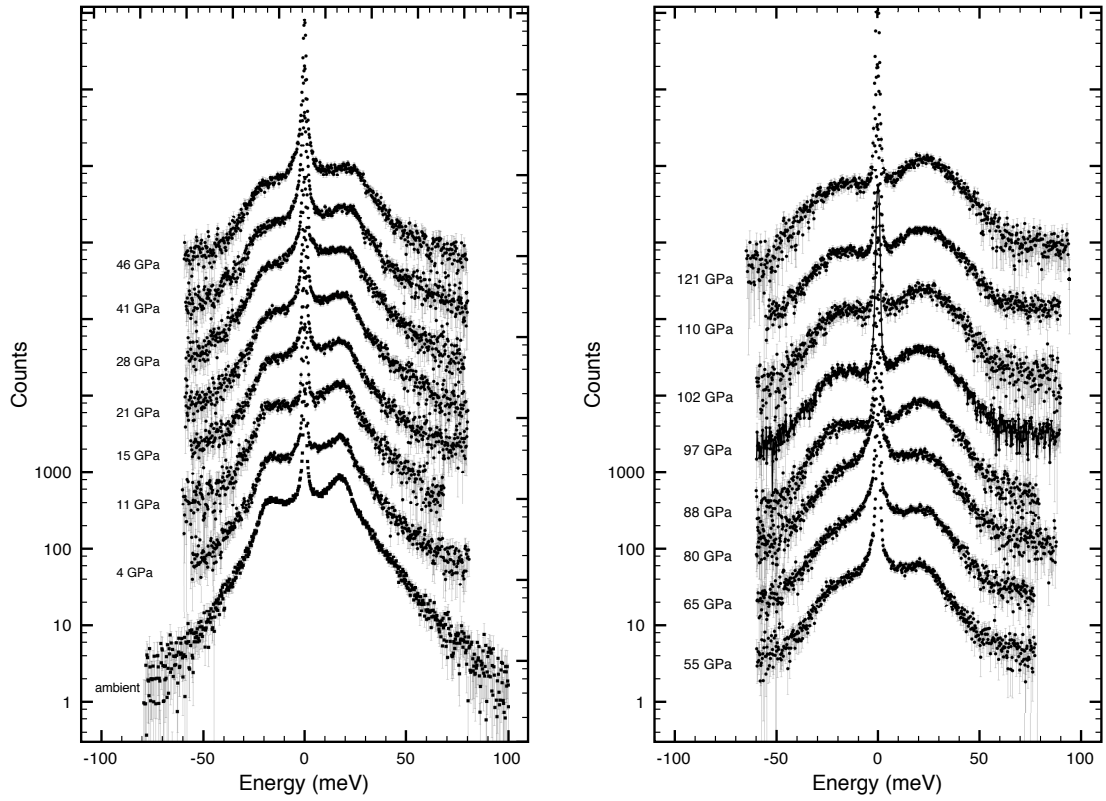

Figure 2.4: Raw NRIXS spectra of $(Mg_{.16}Fe_{.84})O$ at 300 K at different pressures over 0 to 120 GPa, measured at Sector 3-ID-B of the Advanced Photon Source. They are offset in the y-direction for clarity.

(Figure 2.6).

The Debye sound velocity, V_D, is related to the low-energy region of the PDOS in the following manner:

$$V(E) = \left\{ \frac{m\,E^2}{2\pi^2\hbar^3\rho\,D(E)} \right\}^{\frac{1}{3}} \quad \text{and} \quad V_D = V(0) \ , \tag{2.1}$$

where m is the mass of the resonant nucleus, ρ is the mass density of the sample, and $D(E)$ is the PDOS. Values of $V(E)$ were calculated from the measured PDOS and matched to an empirical function $f(E) \approx V_D\,\{1-(E/E_0)^2\}$, where E_0 and V_D are optimized in a standard least-square-fit procedure (*Jackson et al.*, 2009). The energy region for the fit was chosen between 4 and 14 meV.

The lower limit of the energy range is chosen to avoid errors resulting from the subtraction of the elastic contributions and is mainly determined by the energy bandwidth of the X-rays. The upper limit is chosen as the maximum possible energy that permits an acceptably small χ^2 value in

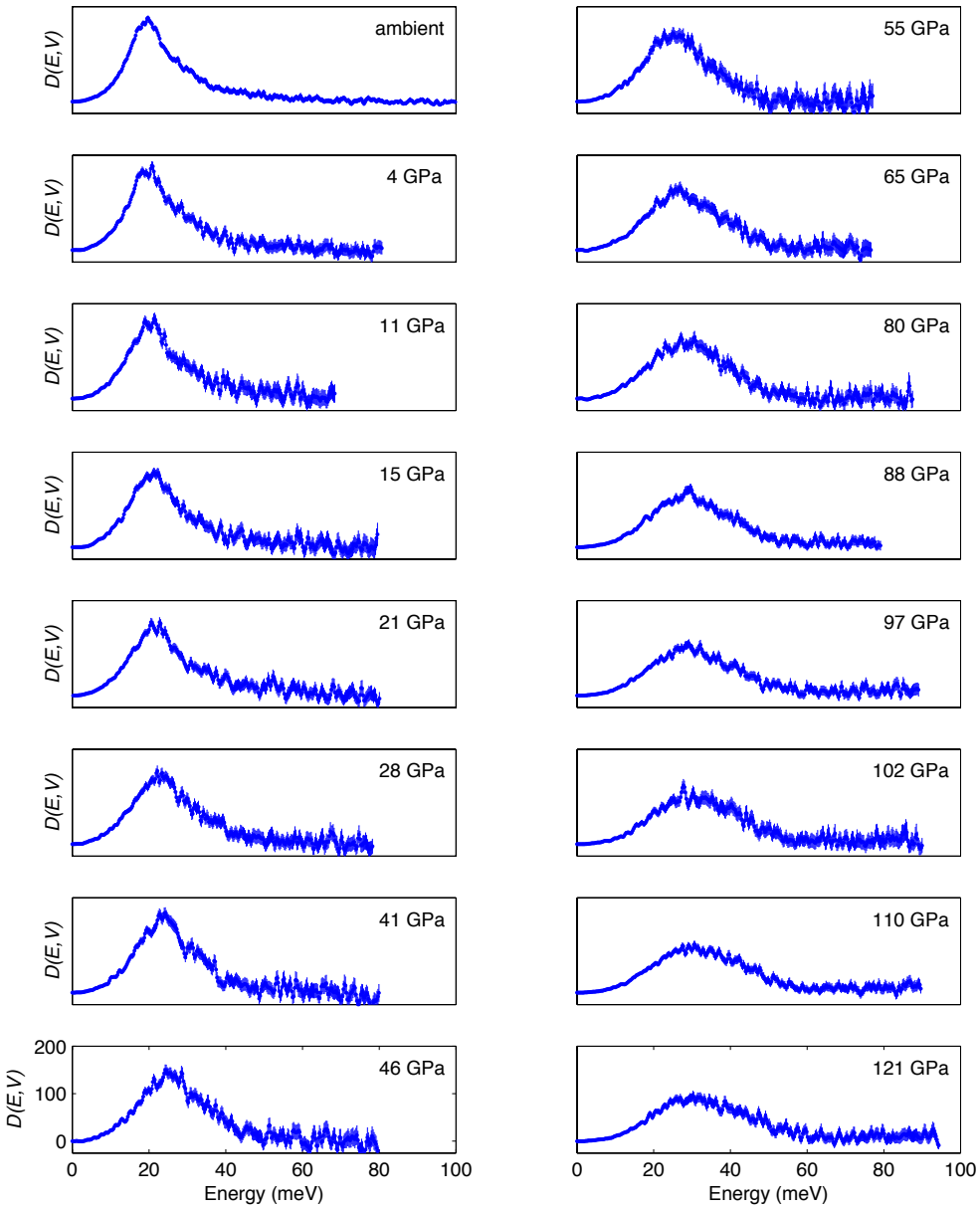

Figure 2.5: Partial projected phonon density of states (PDOSs) of $(Mg_{.16}Fe_{.84})O$, extracted from the NRIXS scans using the PHOENIX software.

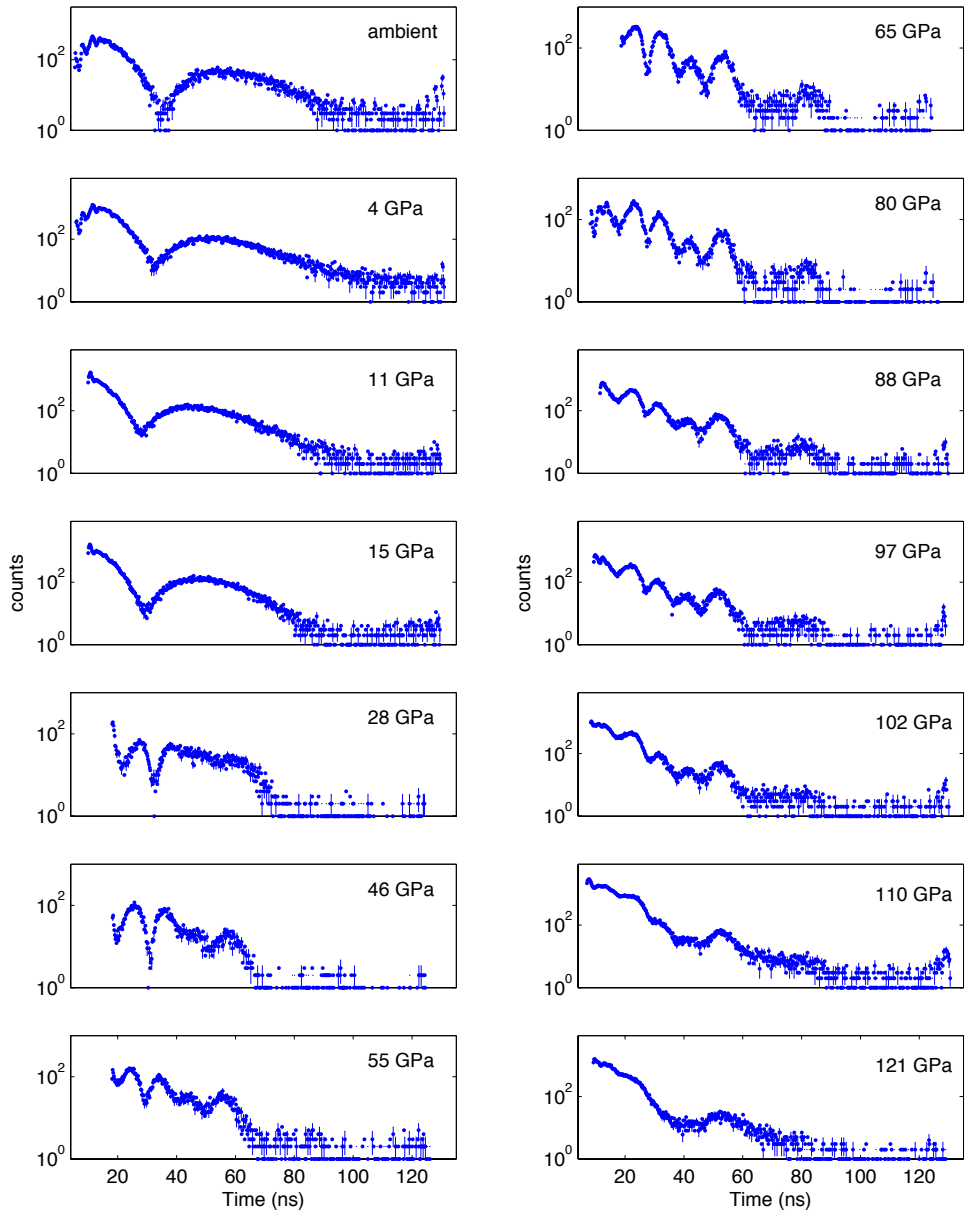

Figure 2.6: Time spectra of $(Mg_{.16}Fe_{.84})O$ from synchrotron Mössbauer spectroscopy. The ambient pressure spectrum is characterized by slow oscillations, consistent with no magnetic ordering. Fast oscillations appear in the spectrum at 28 GPa. A magnetically-ordered state is stable between 28 and 110 GPa. At 121 GPa, the fast oscillations have disappeared, which is indicative of a spin transition to a low-spin state of the Fe $3d$-electron configuration. Error bars are shown for every fourth point, and each data point represents a binning of 4.

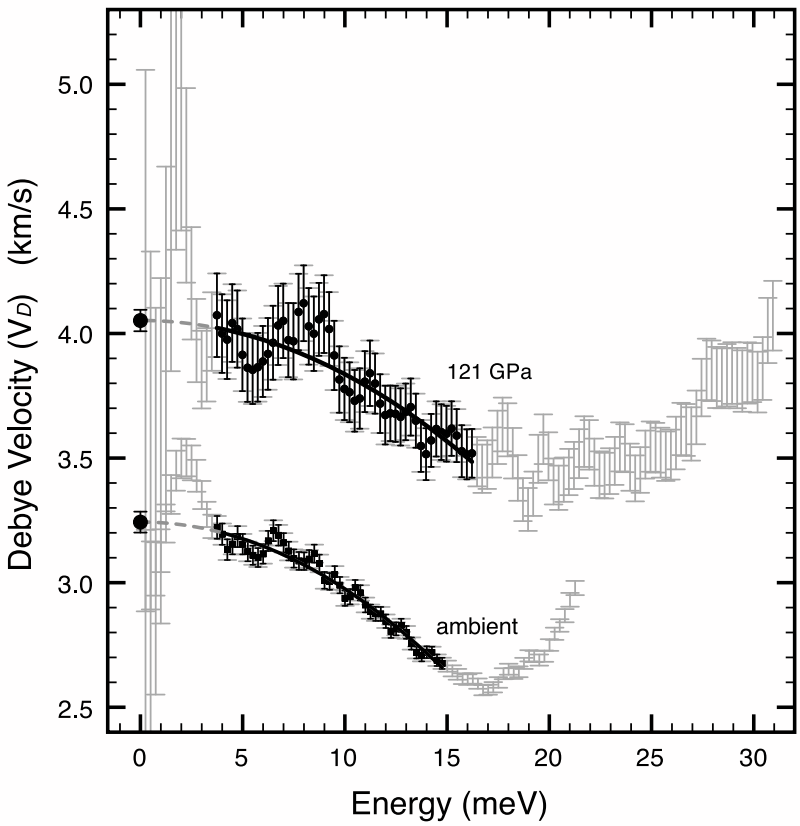

Figure 2.7: Determination of the Debye sound velocity of $(Mg_{.15}Fe_{.85})O$ at ambient pressure and 121 GPa. Symbols show values of Equation (2.1). Solid lines show the best fit of the empirical function $f(E)$ as explained in the text.

the fit procedure. Figure 2.7 shows $V(E)$, the fitted function $f(E)$, and the optimum value of V_D for ambient pressure and 121 GPa. Dashed lines illustrate the extrapolations using the best fits to obtain the Debye sound velocities.

In Figure 2.8, we plot V_D's determined for the entire pressure range. For comparison, we also show V_D's of $Fe_{.947}O$ that we determined from the PDOSs reported in a published NRIXS study, which was conducted at 300 K up to 49 GPa (*Struzhkin et al.*, 2001).

For an isotropic solid, V_D is related to the seismically relevant aggregate compressional (V_P) and shear (V_S) velocities by

$$3/V_D^3 = (1/V_P^3) + (2/V_S^3) \quad \text{and} \quad V_P^2 - (4/3)V_S^2 = K_{0S}/\rho = V_\phi^2 \tag{2.2}$$

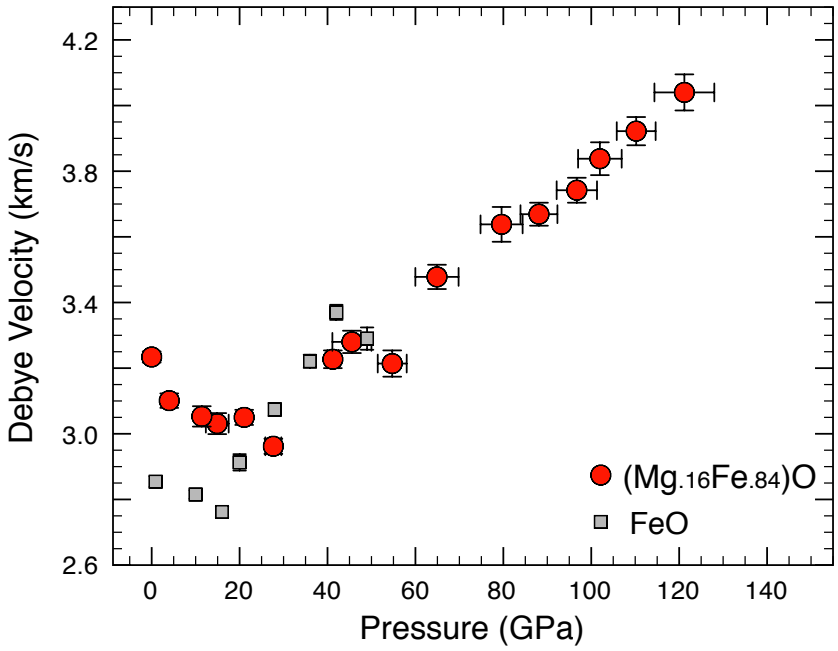

Figure 2.8: Debye sound velocities determined from the PDOS of $(Mg_{.16}Fe_{.84})O$ (this study) and of $Fe_{.947}O$ (*Struzhkin et al.*, 2001) at 300 K.

where K_{0S} is the adiabatic bulk modulus at ambient temperature, ρ is the density, and V_ϕ is the bulk sound velocity. K_{0S} is related to the isothermal bulk modulus, K_{0T}, by $K_{0S} = K_{0T}(1 + \alpha\gamma T)$. K_{0S} can be approximated by K_{0T}, because at room temperature $\alpha\gamma T \leq 0.01$ for most materials (*Angel and Jackson*, 2002). The isothermal third order Birch-Murnaghan weighted equation of state (EOS) from a high-pressure powder x-ray diffraction study up to 93 GPa on $(Mg_{.22}Fe_{.78})O$, a similar composition to that used in our NRIXS measurements, provided the values K_{0T}=191.2±5.5 GPa and K'_{0T}=2.5±0.1 (*Zhuravlev et al.*, 2010). The pressure-dependent density of $(Mg_{.16}Fe_{.84})O$ was obtained by rescaling this EOS with our initial density of 5.69(7) g/cm^3. X-ray diffraction spectra of our sample were taken at select pressures, including ambient, at the Advanced Light Source at Lawrence Berkeley National Laboratory, confirming our choice of EOS and pressure scale. The seismically relevant V_P and V_S values determined at each pressure point are shown for the entire pressure range (Figure 2.9, Table 2.1).

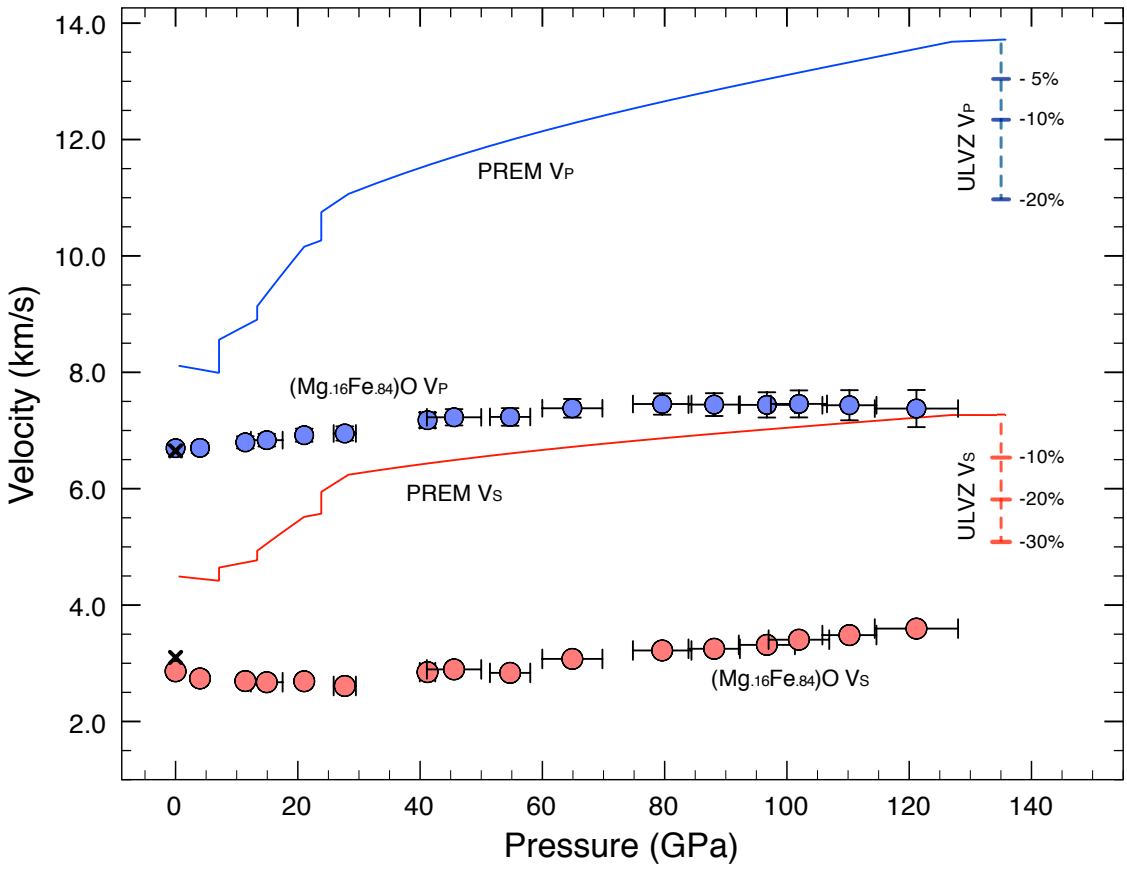

Figure 2.9: V_P (blue) and V_S (red), of $(Mg_{.16}Fe_{.84})O$ determined from V_D along with PREM (*Dziewonski and Anderson*, 1981) and ULVZs (*Thorne and Garnero*, 2004). ×: predicted sound velocities for $(Mg_{.16}Fe_{.84})O$ from an ultrasonic study on (Mg,Fe)O (*Jacobsen et al.*, 2002).

2.3 Results

At ambient pressure, the velocities of $(Mg_{.16}Fe_{.84})O$ are in good agreement with the trend in sound velocities for iron-rich (Mg,Fe)O (*Jacobsen et al.*, 2002; *Struzhkin et al.*, 2001, Figures 2.8, 2.9). In-situ synchrotron Mössbauer spectroscopy shows an absence of magnetic ordering (Figure 2.6) at low pressures, and detailed analysis reveals a quadrupole splitting of about 0.8 mm/s. At pressures approaching 28 GPa, both V_D and V_S of $(Mg_{.16}Fe_{.84})O$ decrease with increasing pressure (Figures 2.8, 2.9). The softening occurs in the vicinity of the transition from the paramagnetic state to a magnetically ordered state around 28 GPa (Figure 2.6). The presence of magnetic hyperfine fields is clear evidence for a magnetically ordered state demonstrating a magnetic transition in $(Mg_{.16}Fe_{.84})O$ around 28 GPa at 300 K—a finding in agreement with a conventional Mössbauer

Pressure (GPa)	Density (g/cm^3)	V_D (km/s)	V_P (km/s)	V_S (km/s)
0	5.69(7)	3.23(2)	6.70(9)	2.86(2)
4.0(3)	5.81(8)	3.10(2)	6.70(9)	2.74(2)
11.4(3)	6.02(8)	3.05(3)	6.8(1)	2.70(3)
15(3)*	6.1(1)	3.03(3)	6.8(1)	2.67(3)
21.0(4)	6.27(8)	3.05(2)	6.9(1)	2.69(2)
28(2)	6.44(9)	2.96(2)	6.9(1)	2.61(2)
41(1)	6.8(1)	3.23(2)	7.2(1)	2.85(2)
46(4)	6.9(1)	3.28(3)	7.2(1)	2.90(3)
55(3)	7.1(1)	3.21(4)	7.2(2)	2.84(3)
65(5)	7.4(1)	3.48(3)	7.4(2)	3.08(4)
80(5)	7.7(1)	3.64(5)	7.5(2)	3.22(5)
88(4)	7.9(1)	3.67(3)	7.5(2)	3.25(3)
97(5)	8.1(1)	3.74(3)	7.4(2)	3.32(3)
102(5)	8.2(2)	3.84(5)	7.5(2)	3.41(5)
110(4)	8.5(2)	3.92(2)	7.5(3)	3.48(4)
121(7)	8.7(2)	4.04(5)	7.4(3)	3.60(5)

Table 2.1: Summary of pressure, density, Debye sound velocity (V_D), and compressional (V_P) and shear (V_S) sound velocities of $(Mg_{.16}Fe_{.84})O$. Numbers in parenthesis reflect the error on the last digit. Errors in pressure reflect the standard deviation of pressures measured from multiple rubies surrounding the sample, measured before and after the x-ray measurement. Errors in ambient pressure density reflect the uncorrelated errors of unit cell volume measurement, sample composition, and assumed vacancies. Errors in V_D incorporate fitting errors in the low-energy region of the PDOS (Figure 2.7) as well as the propagation of the errors in density and pressure. This error is then propagated further to the V_P and V_S errors. * NaCl pressure medium.

study on $(Mg_{.20}Fe_{.80})O$ (*Speziale et al.*, 2005). A similar softening is observed for $Fe_{.947}O$ (*Struzhkin et al.*, 2001, Figure 2.9) and other iron-rich (Mg,Fe)O samples (*Jacobsen et al.*, 2004). This particular behavior has been associated with phonon-magnon coupling (*Struzhkin et al.*, 2001) and has been attributed to c_{44} mode softening preceding the B1 to rhombohedral structural distortion (*Mao et al.*, 1996).

At 121 GPa the fast oscillations, thus the magnetic hyperfine fields, disappear in the time spectrum (Figure 2.6), and is consistent with the onset of a spin transition into a low-spin state of the Fe 3*d*-electron configuration. We note that at pressures above 100 GPa, V_P ceases to increase and gradually softens. Such a behavior is consistent with a transition to a low spin state, as similar observations have been reported for iron-poor (Mg,Fe)O in the vicinity of a spin transition (*Crowhurst et al.*, 2008). Most important, the very low pressure derivatives of V_P and V_S for $(Mg_{.16}Fe_{.84})O$ above 28 GPa persist to the highest pressure measured and ensure that this material retains ultra-low sound velocities at core-mantle boundary pressures.

2.4 Ultralow-Velocity Zones

The shear sound velocity of $(Mg_{.16}Fe_{.84})O$ at 121 GPa is about 55% and 50% reduced compared to MgO (*Murakami et al.*, 2009) and the Preliminary Reference Earth Model (PREM) (*Dziewonski and Anderson*, 1981), respectively. The V_P/V_S ratio at the highest pressure measured is 2.1±0.1, which falls within the V_P/V_S range of ULVZs (2.2±0.3) (*Thorne and Garnero*, 2004). The Poisson ratios (ν) determined from seismic ULVZ observations range from 0.30 to 0.41 and compare favorably to our value of 0.34±0.02 for iron-rich (Mg,Fe)O at 121 GPa and 300 K.

At thousands of K and regardless of its structure (*Lin et al.*, 2003), $(Mg_{.16}Fe_{.84})O$ is unlikely to be stiffer than it is at room temperature, which could result in even lower sound velocities at the CMB. As an illustration of the expected V_P, V_S, and density of a mechanical mixture containing iron-rich (Mg,Fe)O and ambient mantle material, we estimate the effect of temperature on $(Mg_{.16}Fe_{.84})O$'s properties using MgO behavior as a proxy (*Sinogeikin et al.*, 2000). Due to the highly uncertain elastic properties of silicates under CMB conditions, we employ PREM as our bound for the remaining silicate fraction, while recognizing that PREM values may underestimate silicate behavior. We then calculate the Voigt-Reuss-Hill mechanical mixing envelopes for V_P, V_S, and density (*Watt et al.*, 1976) for a given vol% of $(Mg_{.16}Fe_{.84})O$ and PREM (Figure 2.10). To first order, mixing of just 12 vol% of $(Mg_{.16}Fe_{.84})O$ with 88 vol% silicates (represented here by PREM) matches signature seismic observations for the ULVZ (Figure 2.10).

While ULVZ provinces are often considered to be patches of dense partial melt, no measurements exist for the sound velocities of partially molten mantle material at CMB conditions. The connection between ULVZs and partial melting was popularized by the correlation between ULVZ and hot spot locations (*Williams et al.*, 1998). However, not all ULVZs are related spatially to hot spots. An alternative explanation of several ULVZ observations is a dense, localized solid layer containing some amount of iron-rich (Mg,Fe)O. A solid dense layer would not require the intersection of the local geotherm and solidus of the mantle and can produce low sound speeds independent of partial melting (Figure 2.10).

This scenario would require a mechanism in which the (Mg,Fe)O phase becomes enriched in iron

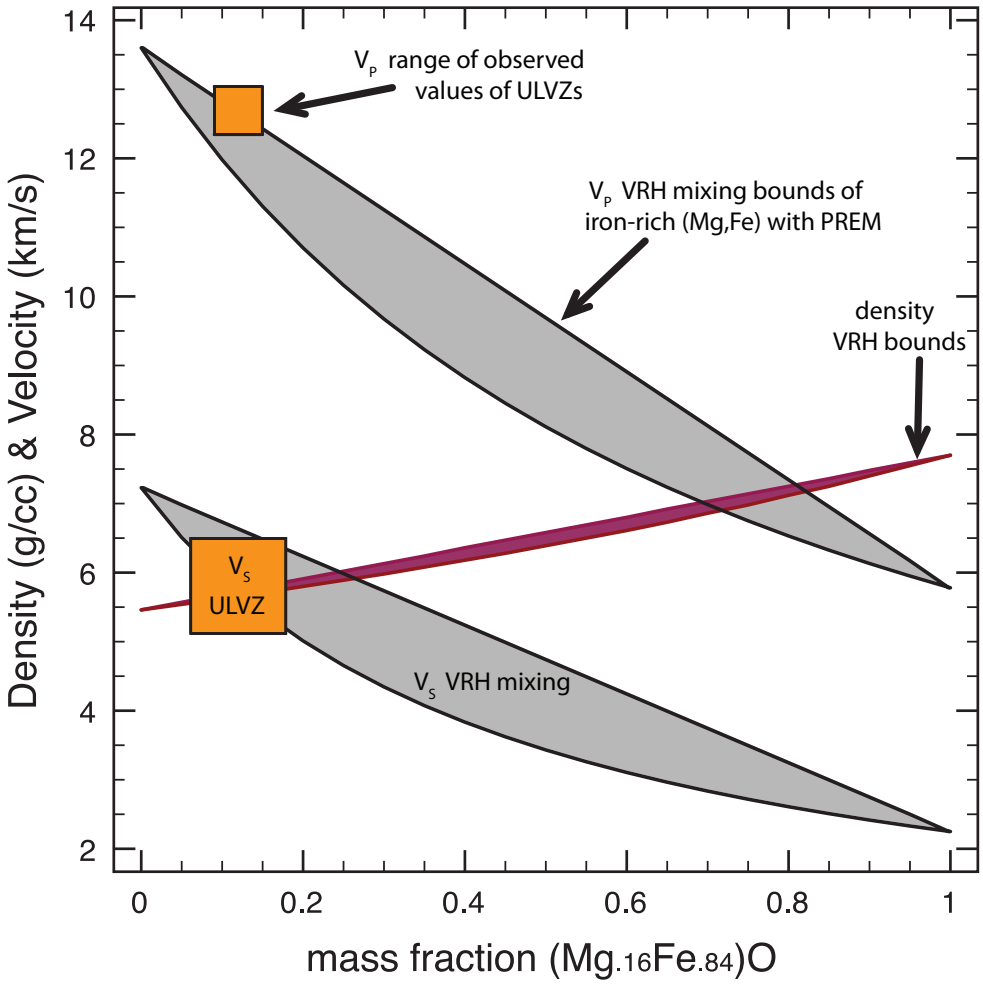

Figure 2.10: Voigt-Reuss-Hill (VRH) mixing of V_P, V_S, and density (red area) of $(Mg_{.16}Fe_{.84})O$ with PREM (see text for details). In orange boxes, we plot V_P and V_S of the ULVZ's centered at 12 vol% $(Mg_{.16}Fe_{.84})O$, which produces a ν of about 0.34. This particular calculation assumes a pressure of 123 GPa and a temperature of 2700 K. The widths of the ULVZ symbols are arbitrary.

in localized areas of the CMB. It has been suggested that extensive iron enrichment could localize in patches in the vicinity of the CMB due to viscosity variations, because liquid iron can be pulled up into the lower mantle on the km scale (*Kanda and Stevenson*, 2006). Iron-rich pockets could represent residue of a fractional crystallization of primordial magma ocean (*Labrosse et al.*, 2007). In representative mantle assemblages with typical amounts of iron, (Mg,Fe)O has been identified as the preferred iron sink (*Auzende et al.*, 2008; *Sinmyo et al.*, 2008).

Chemical reaction studies between liquid iron and lower mantle perovskite or oxide have produced

a wide range of results, leading to interpretations ranging from production of FeSi and FeO (*Knittle and Jeanloz*, 1991; *Song and Ahrens*, 1994) to dissolution of oxygen into liquid iron (*Takafuji et al.*, 2005; *Frost et al.*, 2010). Further investigations exploring the dependence of these reactions on CMB fugacity and chemistry may address these discrepancies, which could be complicated by the possibility of disequilibria. Nevertheless, the low sound velocities of iron-rich (Mg,Fe)O provide compelling motivation to explore the distribution of iron-rich (Mg,Fe)O in the core-mantle boundary region.

Chapter 3

Nuclear Resonant Spectroscopy of $(Mg_{0.06}Fe_{0.94})O$ at high pressure with in-situ X-ray Diffraction

3.1 Introduction

In Chapter 3, we established that iron-rich magnesium oxide ($X_{Fe} = 0.84$) is characterized by very low sound velocities, and found that a magnetic transition occurred between 15 and 28 GPa.

In this chapter, we present a similar study on a different composition, $(Mg_{0.06}Fe_{0.94})O$, hereafter referred to occasionally as Mw94. In addition to providing insight into the compositional dependence of sound velocities, this chapter also reflects improvements in the methodology since the publication of the previous work. Most notably, availability of in-situ XRD allowed us to directly measure the sample's volume, and thus provide in-situ density (ρ) of our sample for every nuclear resonant scattering (NRS) measurement. This allows us to report the direct result of our NRIXS studies: the Debye sound velocity (V_D) at in-situ ρ. Finally, volumes of this material at room temperature measured as part of a synchrotron Mössbauer study (this chapter) and a thermal equation of state study (Chapter 4) give us an equation of state that is used to convert Debye velocities into compressional and shear wave speeds reliably.

Another direct result of this study is the transition pressure of the paramagnetic to antiferromagnetic transition, also known as the Néel transition (*Fujii et al.*, 2011, e.g.). Mössbauer and magnetic investigations have shown a compositional dependence in Néel temperature in the (Mg,Fe)O solid

solution, where projected transition pressure at 300 K coincides with the cubic to rhombohedral distortion (*Speziale et al.*, 2005; *Fujii et al.*, 2011). Other experimental studies, however, find that structural and magnetic transition pressures or temperatures do not coincide (*Kantor et al.*, 2004, 2005, 2006; *Glazyrin et al.*, 2011).

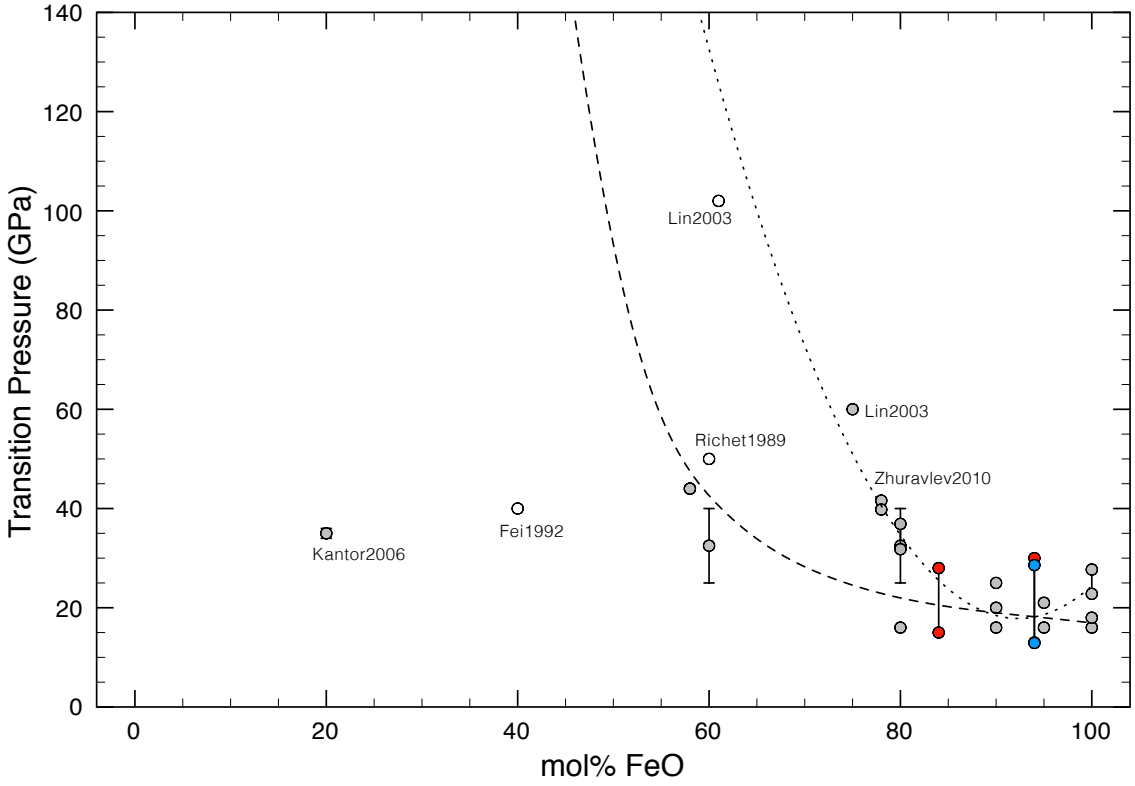

Figure 3.1: Cubic to rhombohedral transition pressures in the literature, as a function of composition. In red we plot our brackets on the magnetic transition pressure from synchrotron Mössbauer spectroscopy of $(Mg_{0.16}Fe_{0.84})O$ (Chapter 2) and $(Mg_{0.06}Fe_{0.94})O$ (this Chapter). In blue we plot the constraint on the cubic to rhombohedral structural transition from X-ray diffraction (Chapter 4). The dashed line indicates the cubic-rhombohedral phase boundary according to *Fei et al.* (2007a), and the dotted line indicates the same according to (*Lin et al.*, 2003). Gray-filled circles are reported transition pressures in the literature (*Mao et al.*, 2002; *Jacobsen et al.*, 2005; *Fei and Mao*, 1994; *Yagi et al.*, 1985; *Zhuravlev et al.*, 2010; *Lin et al.*, 2003; *Shu et al.*, 1998a; *Fei et al.*, 2007a; *Kondo et al.*, 2004; *Richet et al.*, 1989; *Fei et al.*, 2007a; *Kantor et al.*, 2006; *Mao et al.*, 1996), whereas white-filled circles indicate maximum pressures of studies that did not see a transition (*Fei et al.*, 1992; *Richet et al.*, 1989; *Lin et al.*, 2003).

Experimental investigations of the structural transition find that increasing FeO component corresponds to a decrease in transition pressure (*Lin et al.*, 2003; *Shu et al.*, 1998b). The transition pressure is found to be very sensitive to hydrostaticity *Shu et al.* (1998a), and some studies found no

compositional dependence of transition pressure (*Kondo et al.*, 2004). Figure 3.1 shows a summary of cubic to rhombohedral structural transition pressures in the literature, which may reflect a compositional dependence. We include our magnetic transition bounds for $(Mg_{0.16}Fe_{0.84})O$ (Chapter 2) and $(Mg_{0.06}Fe_{0.94})O$ (this Chapter), in addition to structural transition constraints for $(Mg_{0.06}Fe_{0.94})O$ (Chapter 4).

We will describe a synchrotron Mössbauer (SMS) study of $(Mg_{0.06}Fe_{0.94})O$ over the pressure range 8 to 52 GPa with in-situ X-ray diffraction. Next, we will describe nuclear resonant inelastic X-ray scattering (NRIXS) measurements over the pressure range 0 to 80 GPa, also taken with in-situ SMS and X-ray diffraction. These results will be compared to an iron-poor sample, $(Mg_{0.65}Fe_{0.35})O$ (*Chen et al.*, 2012) and to FeO (this study).

3.2 X-ray Diffraction

The (Mg,Fe)O solid solution, excluding the end member FeO, is found in one of two crystal structures in the pressure and temperature range of studies that we conducted. In this chapter, at room pressure and temperature, $(Mg_{0.06}Fe_{0.94})O$ is face-centered cubic, also referred to as $B1$ or rocksalt structure. Its space group is Fm-$3m$, and the first five reflections, i.e. first 3 lattice planes probed with increasing 2θ, are (111), (200), and (220), where the numbers (hkl) refer to the Miller indices of the lattice planes. In a cubic system, the spacing between lattice planes, or $d-$spacing, geometrically gives the lattice constant a:

$$d_{hkl} = \frac{a}{(h^2 + k^2 + l^2)^{1/2}} \tag{3.1}$$

At high pressure, between 8 and 40 GPa and depending on composition and hydrostatisticy of the sample environment, the cubic structure undergoes a distortion to a rhombohedral structure (space group R-$3m$). Rhombohedral unit cells are often described using a hexagonal coordinate system, which encompasses the rhombohedron (the c axis of the hexagonal cell corresponds to the long body-diagonal of the rhombohedral unit cell). In this description, the (111) reflection splits

into two: (003) and (101), the (200) is renamed as the (012) reflection, and the cubic (220) splits into hexagonal (110) and (104).

X-ray diffraction is a scattering technique that measures the elastic, coherent scattering of X-rays off electrons (e.g. *Fultz and Howe*, 2008, and references therein). Powder XRD is variation of this technique that assumes that sampled grains are randomly oriented, such that scattering in the forward direction samples all allowed reflections. We apply this method to understand the changes in unit cell variations with pressure (and temperature, see Chapter 4).

X-ray diffraction can often be performed with in-house X-ray diffractometers with fixed-wavelength sources. The small sample size of diamond anvil cell experiments, however, require higher-intensity radiation to achieve reasonable experiment times. The high flux and versatile energy range of synchrotron experiments make them ideally suited for high pressure experiments. See *Duffy and Wang* (1998) for a discussion on performing high pressure and temperature XRD experiments at the synchrotron.

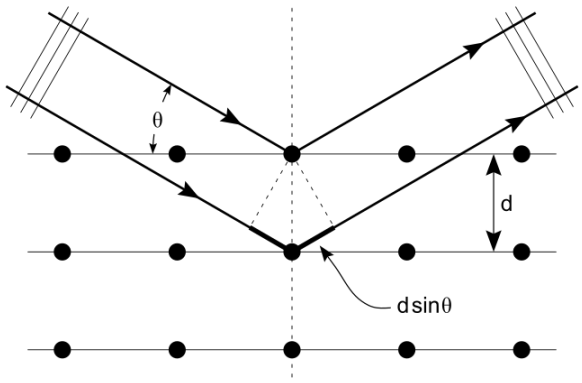

Figure 3.2: Illustration of Bragg's law in X-ray diffraction. Elastic scattering occurs in all directions, but constructive interference occurs in directions in which the Bragg condition is satisfied: $n\lambda = 2dsin\theta$.

The XRD measurements presented in this chapter were measured in conjunction with nuclear resonant scattering experiments at Sector 3-ID-B of the Advanced Photon Source, where a MAR345 image plate is inserted downstream from the sample. The angle-dispersive X-ray pattern is integrated radially using the Fit2D software (*Hammersley et al.*, 1996). A CeO_2 standard is used to calibrate both the X-ray beam center and the distance between the X-ray focus spot and the detector.

The wavelength is optimized, in these experiments, for the resonance energy of ^{57}Fe of 14.4125 meV. This energy, by design, is not optimized for XRD. The $\sim$ 1 meV bandwidth provides relatively small flux compared to beam lines tailored for XRD, and the scattering cross-section of electrons at this energy is small. As a result, typical XRD exposures of oxides in a diamond anvil cell require 10 minutes at low pressure and up to 30 minutes at high pressure, whereas at tailored beam lines for XRD at high pressure (e.g. 13-ID-D, APS) exposures are $\sim$ 1 minute to 2 minutes. Nevertheless, in-situ XRD is required for accurate sound velocity determinations from NRIXS measurements, as the pressure gradients (and therefore uncertainty in the absence of in-situ XRD) can reach upwards of 10 GPa across 100 μm.

3.3 Experimental Details

3.3.1 NRIXS with in-situ XRD

This high-pressure nuclear resonance scattering experiment was conducted at Sector 3-ID-B of the Advanced Photon Source at Argonne National Laboratory in August 2011 and October 2012. Three samples were prepared for this experiment. For the high pressure points, beveled anvils with 300 μm-culets were used. The $(Mg_{0.06}Fe_{0.94})O$ sample was embedded in boron epoxy, with rubies on either side, one on each culet. The pressure of the sample's environment was tracked with both ruby fluorescence (*Mao et al.*, 1986, only visible in compression to initial pressure point) and "diamond edge" Raman spectroscopy of diamond anvil culet (*Akahama and Kawamura*, 2006), but ultimately the pressure of the sample was determined with in-situ X-ray diffraction. The ambient pressure data point was taken in air. A low pressure data point (11.6 GPa) was taken of a sample loaded in a DAC with beveled 400 μm-culets, with beryllium gasket, and KCl pressure medium. We summarize the compression points measured in Table 3.1.

At each compression point, we collected a series of inelastic spectra, a synchrotron Mössbauer spectrum, and an X-ray diffraction spectrum (often both before and after the NRS spectra).

Raw spectra are shown in Figure 3.8. Energy scans were collected over a minimum energy range

	Environment	P_{ruby}[a] (GPa)	P_{sample}[b] (GPa)	Energy range (meV)	Scans, count times	P_{XRD}[c] (GPa)
1	air			$-80 \rightarrow +100$	1 at 3 sec/pt, 1 at 4 sec/pt	0
2	KCl, Be gasket		11.6	$-60 \rightarrow +70$	1 at 3 sec/pt, 5 at 5 sec/pt	9.61(2)[d]
3	B epoxy	41.2	43.5, 48.4[e]	$-60 \rightarrow +80$	1 at 3 sec/pt, 3 at 5 sec/pt	42.7(7)
4	B epoxy		59.1	$-60 \rightarrow +80$	1 at 3 sec/pt, 4 at 5 sec/pt	55(1)
5	B epoxy		72, 76[e]	$-60 \rightarrow +80$	5 scans at 5 sec/pt	64(2)
6	B epoxy		85	$-60 \rightarrow +80$	7 scans at 5 sec/pt	81.6(7)
				$-70 \rightarrow +130$	1 at 3 sec/pt, 5 at 5 sec/pt	81.1(8)[f]

Table 3.1: Details of the $(Mg_{0.06}Fe_{0.94})O$ NRIXS experiment. [a]Pressures were determined off-line using ruby fluorescence (*Mao et al.*, 1986). [b]Pressures were determined offline using the diamond edge (*Akahama and Kawamura*, 2006). [c]Pressures from XRD were determined from the combined equation of state of $(Mg_{0.06}Fe_{0.94})O$, given in Table 3.3 and Figure 3.5. [d]Number in parenthesis gives the error on the last digit. [e]Two numbers listed indicate before and after measurements [f]Without increasing pressure, the highest compression point was remeasured in October 2012.

of $-60 \rightarrow +70$ meV. At the highest compression point (#6, ∼82 GPa), the energy scan was measured again in October 2012 with an extended energy range.

3.3.2 SMS with in-situ XRD

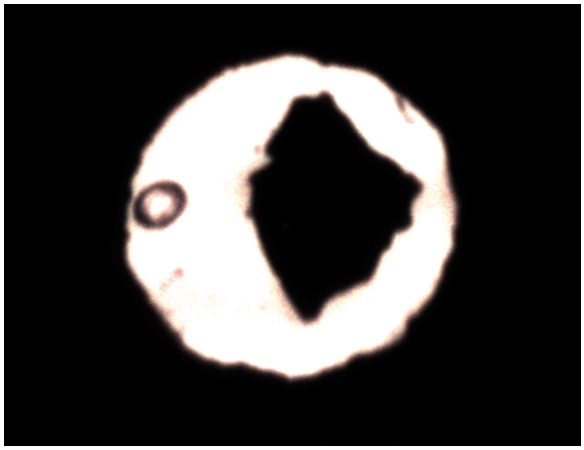

Figure 3.3: $(Mg_{0.06}Fe_{0.94})O$ at 50 GPa in the Synchrotron Mössbauer study. The sample chamber is 150 μm across. This study was conducted at 300 K. Ruby sphere is located to the left.

An independent synchrotron Mössbauer spectroscopy (SMS) experiment was carried out at Sector 3-ID-B of the Advanced Photon Source in February 2012. $(Mg_{0.06}Fe_{0.94})O$ was loaded in a diamond anvil cell with KCl as a pressure-transmitting medium in a rhenium metal gasket. A small ruby was included near the edge of the sample chamber (Figure 3.3). XRD and SMS were collected at 8 compression points over the range 7.8 to 52.4 GPa, determined by the equation of state of

KCl (*Dewaele et al.*, 2012). Ruby fluorescence was used to track the pressure offline. As Sector 3 is optimized for NRS (not XRD), with relatively low flux at a low energy with low scattering efficiency off electrons, we only observed one reflection of $(Mg_{0.06}Fe_{0.94})O$ (200) and KCl (110). One reflection is enough to determine the unit cell volume for cubic symmetry, which both KCl and $(Mg_{0.06}Fe_{0.94})O$ are at low pressure. At high pressure, we can estimate rhombohedral distortion, assuming that rhombohedral distortion is solely a function of pressure. In Chapter 4, Figure 4.8 shows the evolution of d-spacings as a function of pressure, and gives the interpolation $d_{012_R} \approx -0.0019 \times P + 2.1064$, a linear relationship between d-spacing of the rhombohedral (012) reflection and pressure. See Section 4.6 for more details.

The d-spacings and resulting pressure of KCl and $(Mg_{0.06}Fe_{0.94})O$ are summarized in Table 3.2. $(Mg_{0.06}Fe_{0.94})O$ d_{200} are interpreted as either cubic volumes or rhombohedral volumes.

P_{ruby} (GPa)	P_{KCl} (GPa)[a]	d_{110} KCl (Å)	d_{200} Mw94 (Å)	Vol/atom (Å^3)$_C$	Vol/atom (Å^3)$_R$
7.92	7.79	2.114	2.481	9.443	
11.72, 12.17	13.09	2.100	2.415	9.258	
15.71, 16.59	19.16	2.081	2.360	9.015	
19.71, 20.1	22.92	2.069	2.333	8.851	
23.84, 24.17	29.51	2.049	2.293	8.605	8.646
28.08, 28.62	35.73	2.036	2.262	8.439	8.487
34.97	43.47	2.018	2.228	8.223	8.275
	52.43	2.000	2.196	8.005	8.058

Table 3.2: XRD results of the $(Mg_{0.06}Fe_{0.94})O$ SMS experiment. When two numbers are listed, ruby pressures correspond to before and after the SMS and XRD measurement. [a]KCl pressure is determined from the d-spacing of KCl using the equation of state of KCl (*Dewaele et al.*, 2012). C and R subscripts indicate volumes assuming that the Mw94 d-spacing corresponds to the cubic (200) or rhombohedral (012) reflection.

3.4 Results

3.4.1 XRD: Isothermal Equation of State

A Birch-Murnaghan equation of state was fit to the pressure-volume data given in Table 3.2, given by the equations:

$$P(V) = 3K_0 f_E (1 + 2f_E)^{\frac{5}{2}} \left\{ 1 + \frac{3}{4}(K_0' - 4) f_E \right\} \tag{3.2}$$

$$f_E = \frac{1}{2}\left[\left(\frac{V_0}{V}\right)^{\frac{2}{3}} - 1\right] \tag{3.3}$$

where K_0 is the initial bulk modulus, K_0' is the pressure derivative of the bulk modulus, and f_E is Eulerian strain. K_0' fixed to 4. Pressure was determined by the equation of state of KCl (*Dewaele et al.*, 2012), and the results are summarized in Table 3.3. In the first fit, sample volumes were interpreted as being cubic given the measured d_{200} (Table 3.2). Cubic sample volumes are plotted as black circles in Figure 3.4. In the second fit, the rhombohedral estimates of volumes were included. These two fits are plotted in Figure 3.4.

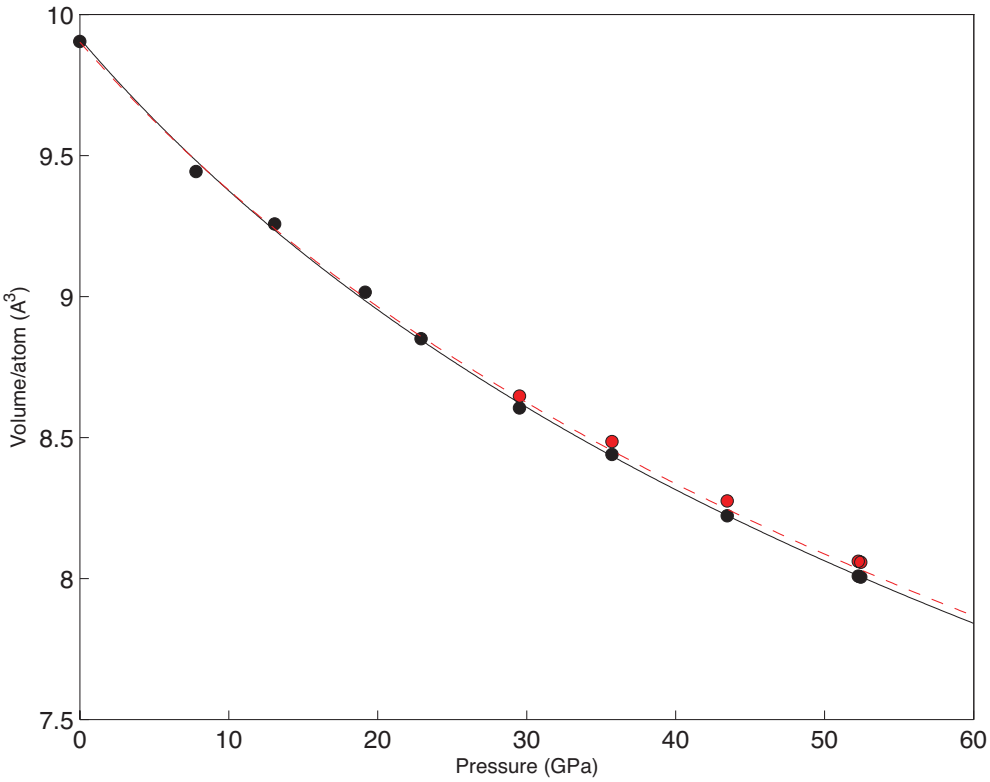

Figure 3.4: Volume of $(Mg_{0.06}Fe_{0.94})O$ at 300 K determined by its (200) reflection, with pressure determined by the volume of $B2$-KCl, determined by its (110) reflection, using the equation of state given by *Dewaele et al.* (2012). Black line is a Birch-Murnaghan equation of state with K_{0T}' fixed to 4, giving V_0 = 9.91(2) Å^3/atom, K_{0T} = 160(2) GPa. Red circles show volumes assuming a rhombohedral structure (See text and Table 3.2), and the red dashed curve shows the fit calculated with those points included (V_0 = 9.90(3) Å^3/atom, K_{0T} = 164(4) GPa). Equation of state results are summarized in Table 3.3.

In the third fit, the room temperature rhombohedral quench data from our high pressure and

temperature XRD experiment (Chapter 4) are also included. We plot this combined equation of state in Figure 3.5. This equation of state is used to determine pressure in the NRIXS study.

	V_0 (Å^3)	K_{0T} (GPa)	K'_{0T}
Assume cubic	9.91(2)	160(2)	4 (fixed)
Include rhombo	9.90(3)	164(4)	4 (fixed)
Combined[a]	9.90446($fixed$)	189(4)	2.9(1)

Table 3.3: Equations of state fit to the $(Mg_{0.06}Fe_{0.94})O$ dataset. [a]In this fit, the ambient temperature dataset was combined with the 300 K quench data of $(Mg_{0.06}Fe_{0.94})O$ from our high pressure and temperature XRD study (discussed in Chapter 4).

3.4.2 SMS: Magnetic Ordering Transition

Figure 3.6 shows the spectra from the synchrotron Mössbauer experiment. Pressure determined by the equation of state of KCl are shown on the right. At low pressure the spectra are characterized by slow oscillations, consistent with no magnetic ordering. With increasing pressure, it is expected that the quadrupole splitting of the nuclear excited state should increase as inter-atom bond shortening accentuates the intra-atom electric field gradient, i.e. the rate of change of electric field at the nucleus. This effect is reflected in the SMS spectrum in the shortening of period between 8 and 13 GPa. This trend does not persist at higher pressures. At 19 GPa the period in the SMS spectrum has increased and continues to do so with pressure up to 23 GPa. At higher pressure the spectra are characterized by fast, irregular oscillations, indicative of a magnetically-ordered state coupled with thickness effects.

The changes in the SMS spectrum preceding the magnetically-ordered state at 30 GPa are either indicative of a growing magnetically-ordered component, indicating a gradual transition, or some other change preceding a sharp transition. Careful fitting of the spectra is required.

In Figure 3.7, SMS spectra measured in-situ in the NRIXS experiment are shown. Pressures listed are determined from the combined equation of state of $(Mg_{0.06}Fe_{0.94})O$ (Table 3.3) using the

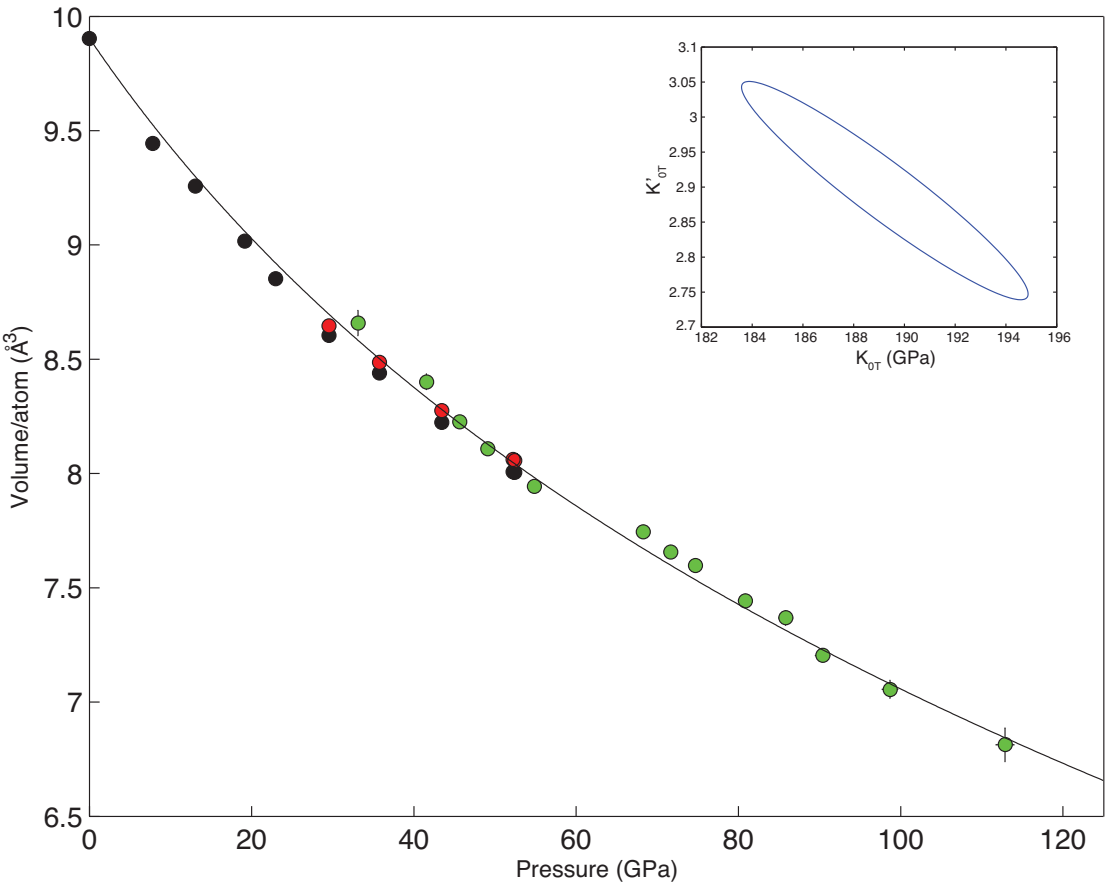

Figure 3.5: Volume of $(Mg_{0.06}Fe_{0.94})O$ measured in the SMS experiment (black and red circles, also shown in Figure 3.4) and the thermal equation of state study in Chapter 4. Green circles are volumes of rhombohedral "quench" points after each heating cycle of $(Mg_{0.06}Fe_{0.94})O$ in the buffered experiments, described in Section 4.6 and summarized in Table 4.6. The black line is a Birch-Murnaghan equation of state with $V_0 = 9.90446$ Å^3/atom (fixed), $K_{0T} = 189(4)$ GPa and $K'_{0T} = 2.9(1)$. Inset: 1σ error ellipse of K_{0T} and K'_{0T}.

d-spacings from in-situ XRD at each NRIXS pressure point (Table 3.4). Spectra were collected only over the pressure range 43-82 GPa, and all display magnetic ordering and thickness effects. As expected, there is no evidence of a spin transition in the pressure range probed by this study.

3.4.3 NRIXS: Sound Velocities

NRIXS spectra were collected over the pressure range 0 to 82 GPa. Raw spectra are shown in Figure 3.8. The phonon peak around 19 meV at ambient pressure moves out to about 24 meV at 55 GPa as vibrations move to higher energy with pressure. We see the emergence of the multi-phonon contribution to the vibrational spectrum at around 80 meV, most visible in the extended energy

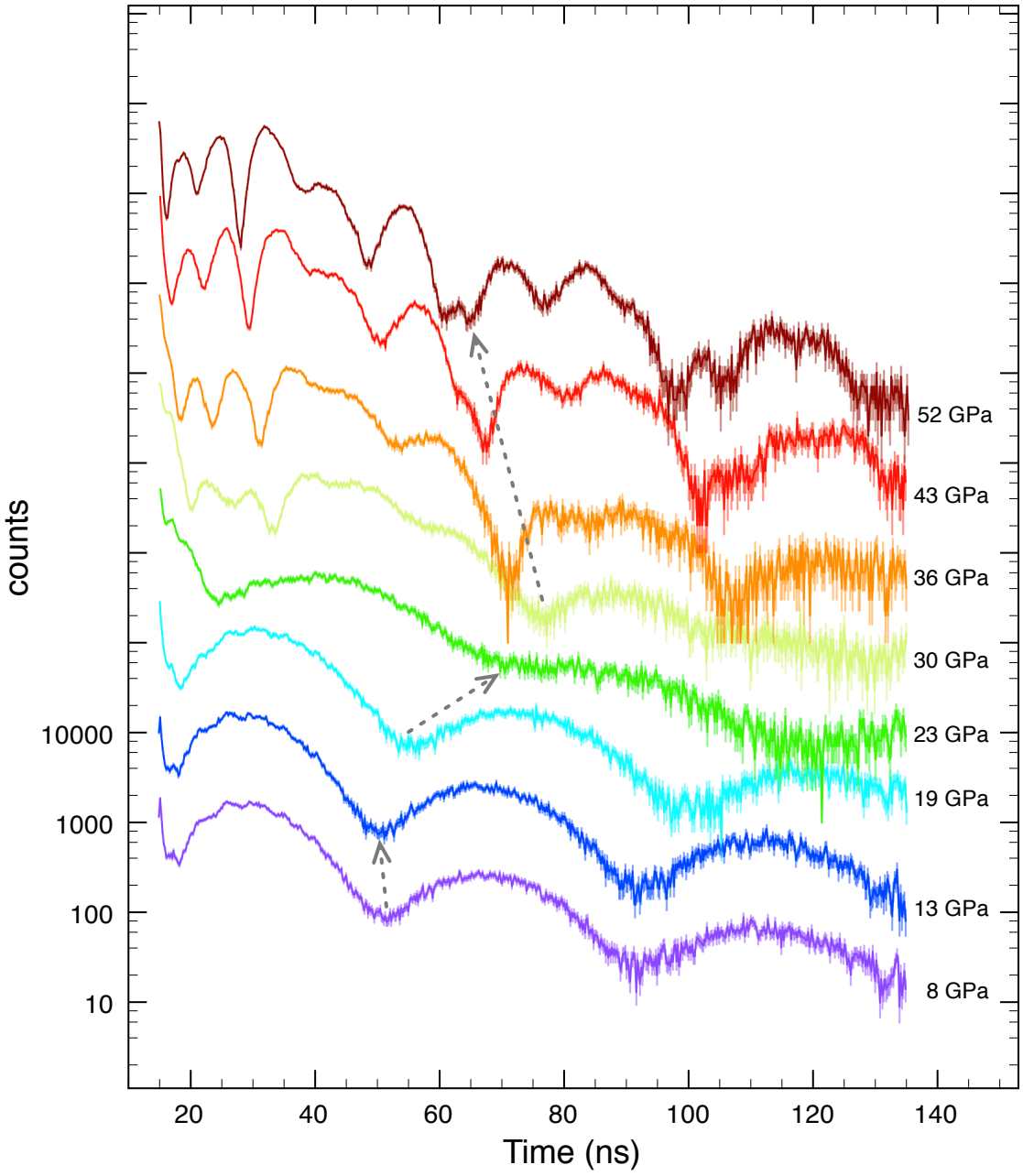

Figure 3.6: Synchrotron Mössbauer spectra of $(Mg_{0.06}Fe_{0.94})O$ at 300 K, with data binned into groups of 4. A magnetic transition occurs between 23 and 30 GPa. Pressures listed are determined from the equation of state of KCl (*Dewaele et al.*, 2012).

range of the 82 GPa pressure point.

Energy scans from our NRIXS study were processed using the PHOENIX software (*Sturhahn*, 2000) using methods described in *Sturhahn* (2004). Resulting PDOSs are shown in Figure 3.9.

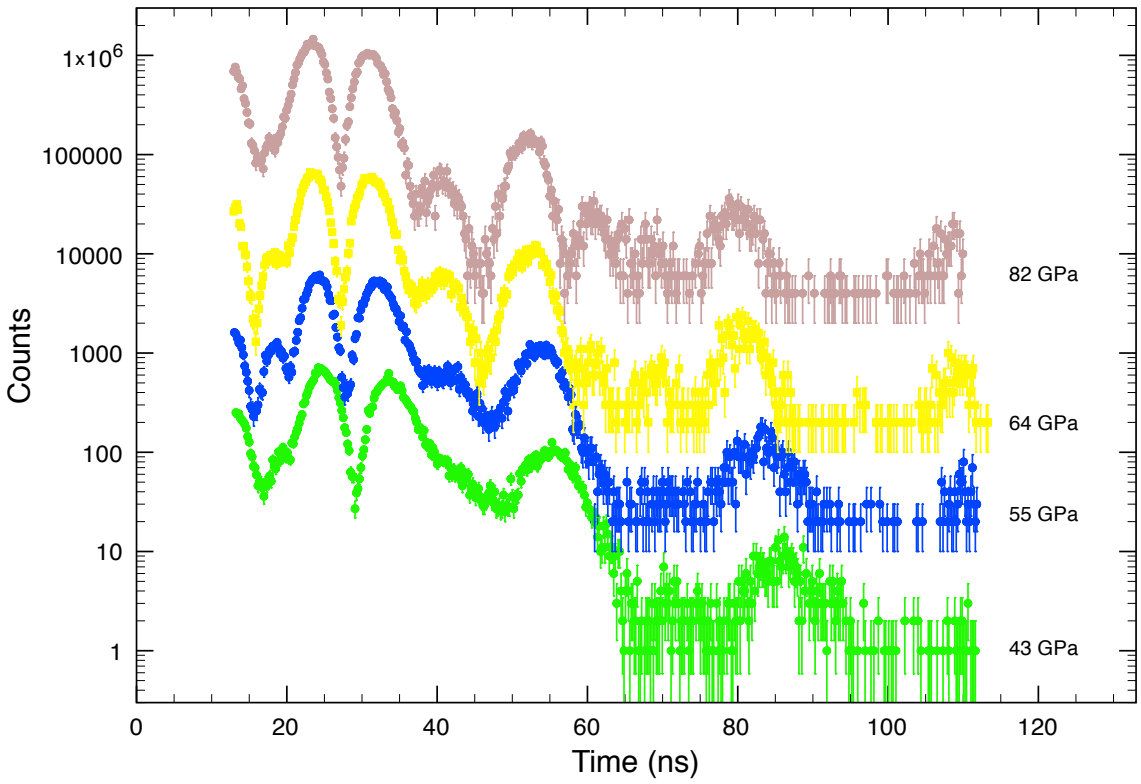

Figure 3.7: In-situ synchrotron Mössbauer spectra of $(Mg_{0.06}Fe_{0.94})O$ at 300 K, with data binned into groups of 4. A magnetic transition occurs between 23 and 30 GPa. Pressures listed are determined from the combined equation of state of $(Mg_{0.06}Fe_{0.94})O$, summarized in Table 3.3. The *d*-spacings from in-situ XRD used to calculate the pressure are listed in Table 3.4.

Figure 3.10 shows, in detail, two different phonon dispersion models applied to the low-energy region of the PDOS to derive the Debye velocity using the *psvl* subroutine in PHOENIX. In this procedure, the PDOS is scaled according to Equation 2.1. A strict "Debye-like" region varies quadratically with energy, which would be flat in this scaling (red line, Figure 3.10). More data can be included if we don't impose such a strict scaling, fitting instead an empirical function $f(E) \approx V_D \{1-(E/E_0)^2\}$ that projects to zero energy (blue line, Figure 3.10). In either case, the zero-energy limit of the scaled PDOS is the Debye velocity (V_D). The lower energy limit of the fitting region to obtain this intercept is limited by the successful subtraction of the elastic peak. The upper limit of the fitting region is determined both by visual inspection, the χ^2 of fitting, and reasonable energy ranges where the phonons behave like an acoustic medium.

Results from fitting in the *psvl* routine are presented in Table 3.4 and Figure 3.11. Fitting with

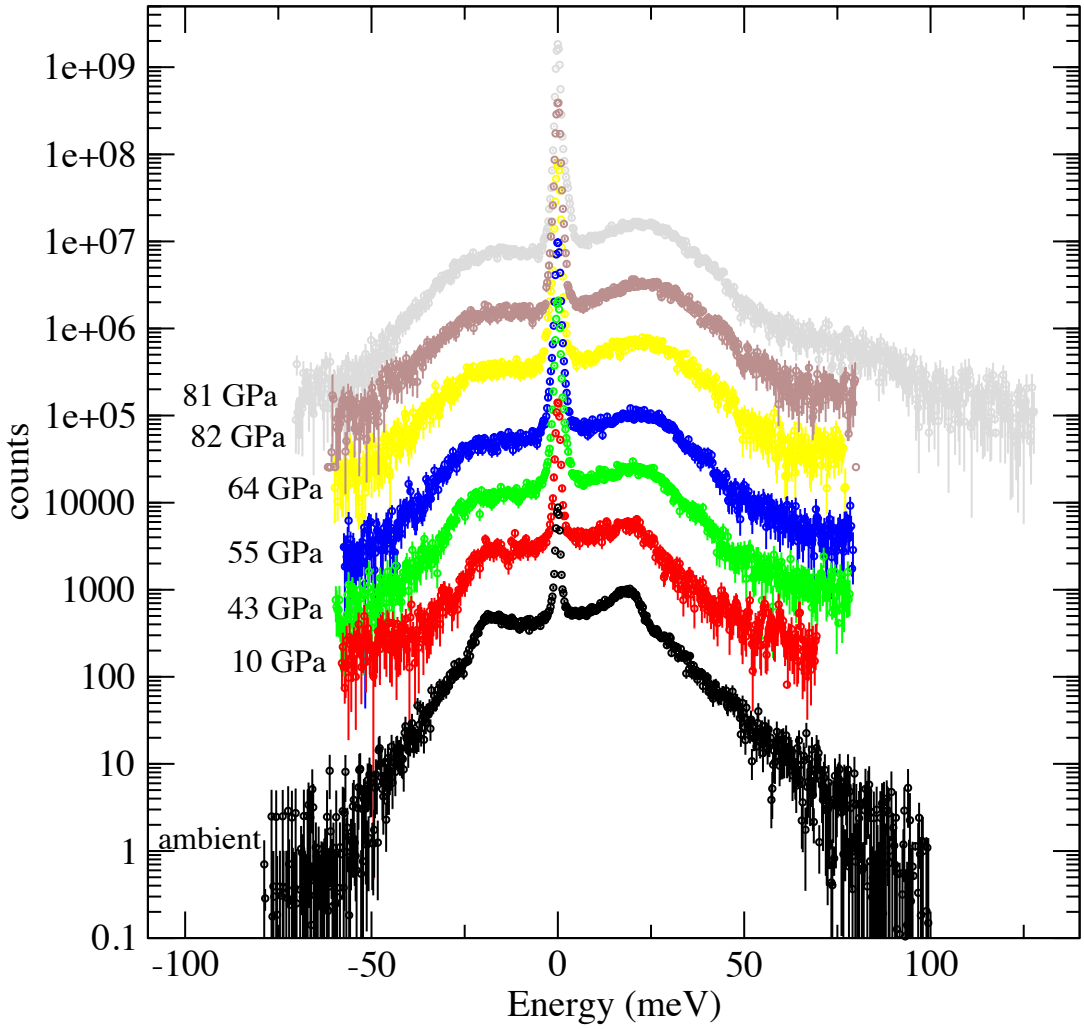

Figure 3.8: Raw NRIXS spectra of $(Mg_{0.06}Fe_{0.94})O$ at 300 K. Spectra are offset in the y-direction for clarity.

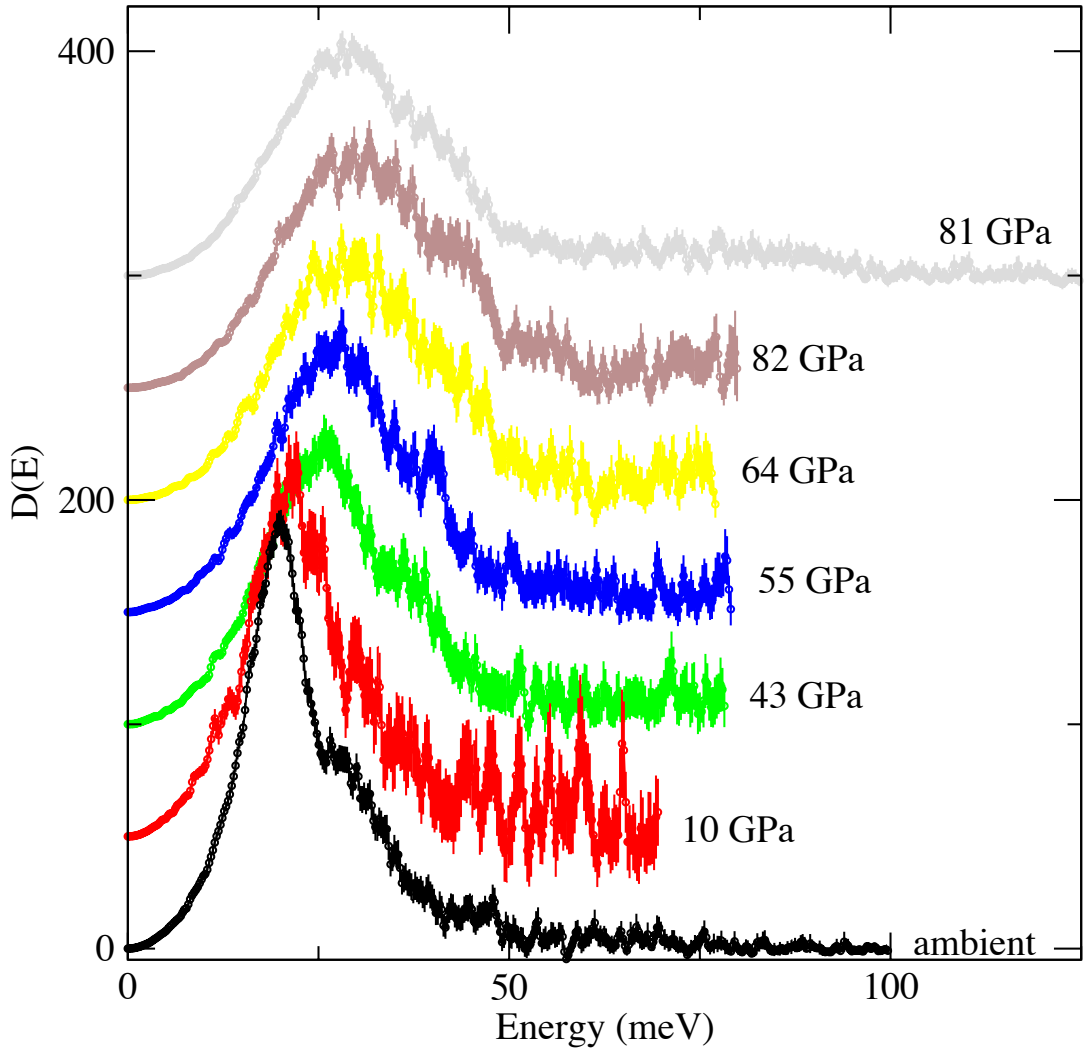

Figure 3.9: Partial projected phonon density of states of $(Mg_{0.06}Fe_{0.94})O$ at 300 K, extracted from raw spectra using PHOENIX (*Sturhahn*, 2000). Spectra are offset in the y-direction for clarity.

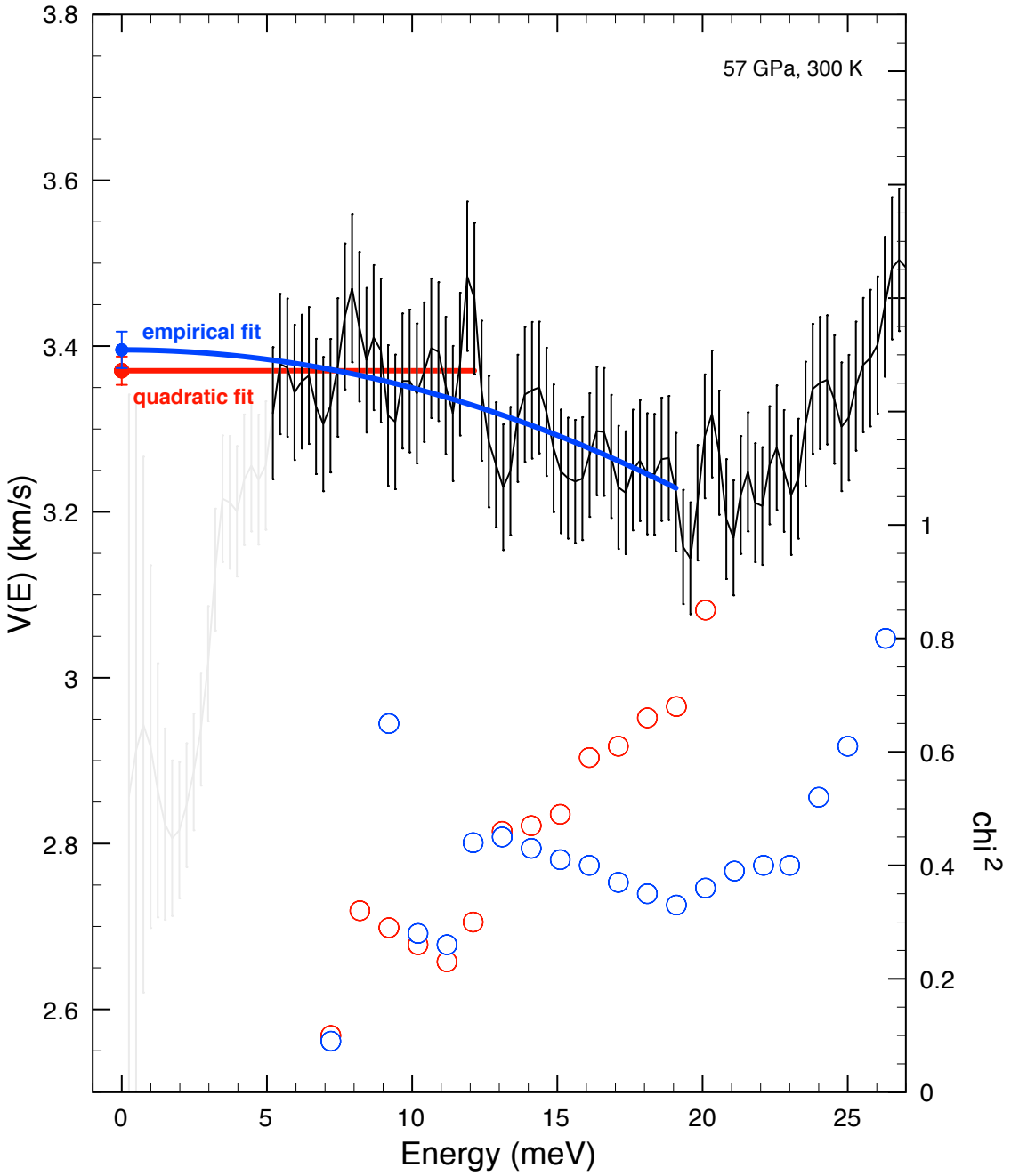

Figure 3.10: Debye velocity determination using the *psvl* subroutine in PHOENIX at 57 GPa. The PDOS is scaled according to Equation 2.1. A quadratic fit to $V(E)$ best describes data up to 12 meV (red line). More of the PDOS can be included if an empirical function is instead used (blue line). V_D is the intercept at $E = 0$ (red and blue circles). Open circles are the χ^2 values calculated in *psvl*, plotted at the E_{max} of each calculation.

the quadratic requirement uses a smaller range of energy.

in-situ d_{200} (Å)	ρ (g/cc)	$V_{D(normal)}$ (km/s)	$E_{min} - E_{max(normal)}$ (meV)	$V_{D(quad)}$ (km/s)	$E_{max(quad)}$ (meV)
2.480[a]	5.93(2)	3.08(1)	5.0 − 14.1		
2.114	6.23(3)	2.97(2)	5.7 − 19.9	2.94(2)	10.7
2.023, 2.022[b]	7.08(4)	3.27(2)	5.7 − 18.6	3.25(2)	10.6
1.998, 1.995[b]	7.36(4)	3.40(2)	5.2 − 19.1	3.3(2)	12.1
1.980, 1.975[b]	7.58(4)	3.62(2)	3.7 − 20.8	3.59(2)	10.7
1.948, 1.946[b]	7.95(3)	3.78(2)	5.9 − 21.0	3.69(2)	10.9
1.948	7.94(6)	3.73(2)	5.2 − 17.9	3.64(1)	9.0

Table 3.4: Debye Velocity (V_D) of $(Mg_{0.06}Fe_{0.94})O$ as a function of in-situ density, calculated with both the quadratic fit and normal fit. This data is shown in Figure 3.10. [a]This particular d-spacing corresponds to the (111) reflection. [b]Two d-spacings correspond to before and after XRD measurements.

Debye velocities of $(Mg_{0.06}Fe_{0.94})O$ are compared to those of $(Mg_{0.65}Fe_{0.35})O$ (*Chen et al.*, 2012) and FeO (this study, Appendix A.3) in Figure 3.12. In this plot, the $(Mg_{0.06}Fe_{0.94})O$ and $(Mg_{0.65}Fe_{0.35})O$ densities were determined with in-situ XRD. The densities for FeO at low pressure was determined by volume measured with XRD at Sector 12.2.2 of the Advanced Light Source, and at high pressure by volume measured with XRD at Sector 13-ID-D, GSECARS in February 2012.

Using the combined equation of state determined in Section 3.4.1, shown in Figure 3.5, we calculated pressure from our in-situ densities and the seismically relevant V_P and V_S from our V_D. The results are summarized in Table 3.5. In Figure 3.13, we plot V_P and V_S as a function of pressure. For comparison, we plot the sound velocities of $(Mg_{0.65}Fe_{0.35})O$, measured using NRIXS with in-situ XRD by *Chen et al.* (2012). At 70 GPa, $(Mg_{0.65}Fe_{0.35})O$ is just coming out of a spin transition, which is reflected in the low P-wave velocities. Between 100 and 140 GPa, the sound velocities of $(Mg_{0.65}Fe_{0.35})O$ are linear with pressure. $(Mg_{0.65}Fe_{0.35})O$ is more iron-rich than expected for typical lower mantle ferropericlase (*Murakami et al.*, 2005), and could be present in in iron-enriched regions of the lower mantle. The sound velocities of $(Mg_{0.06}Fe_{0.94})O$ are much lower than those of $(Mg_{0.65}Fe_{0.35})O$, and better able to explain ULVZs.

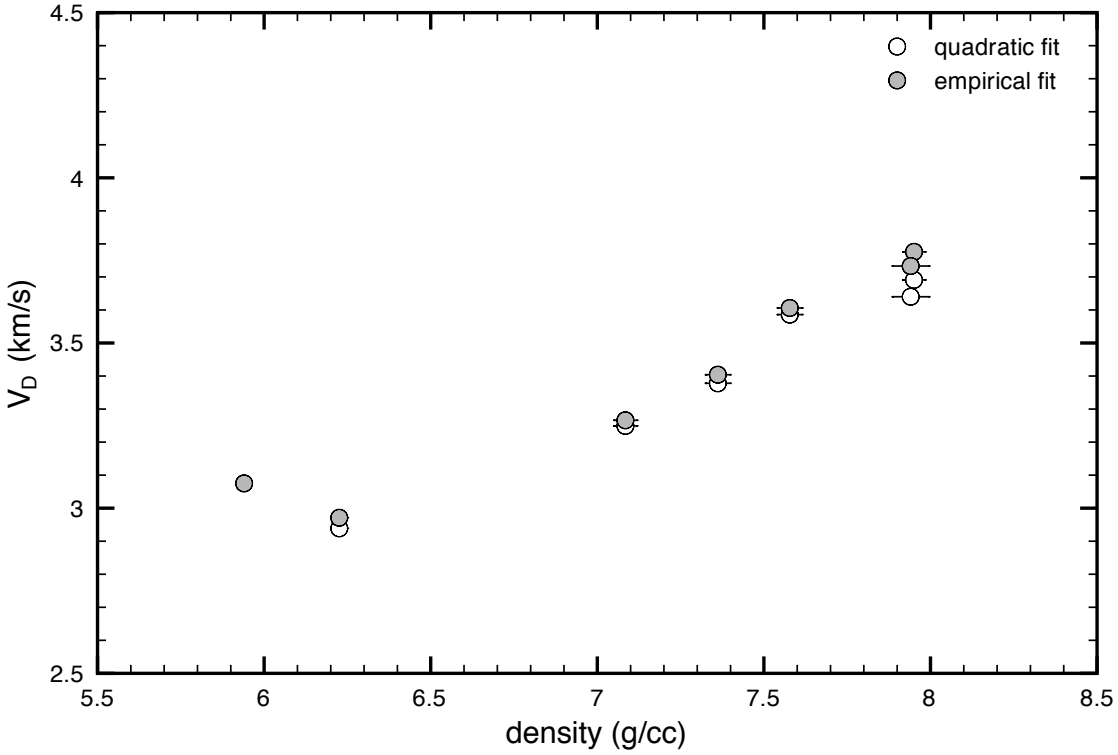

Figure 3.11: Debye velocity (V_D) of ($Mg_{0.06}Fe_{0.94}$)O at 300 K as a function of density. Fits in which a quadratic form of the low-energy region of the PDOS is assumed are shown in white, while a more flexible parameterization of the low-energy region results in Debye velocities shown in gray (empirical fit), as described in the text. Figure 3.10 illustrates the difference between the two fitting routines.

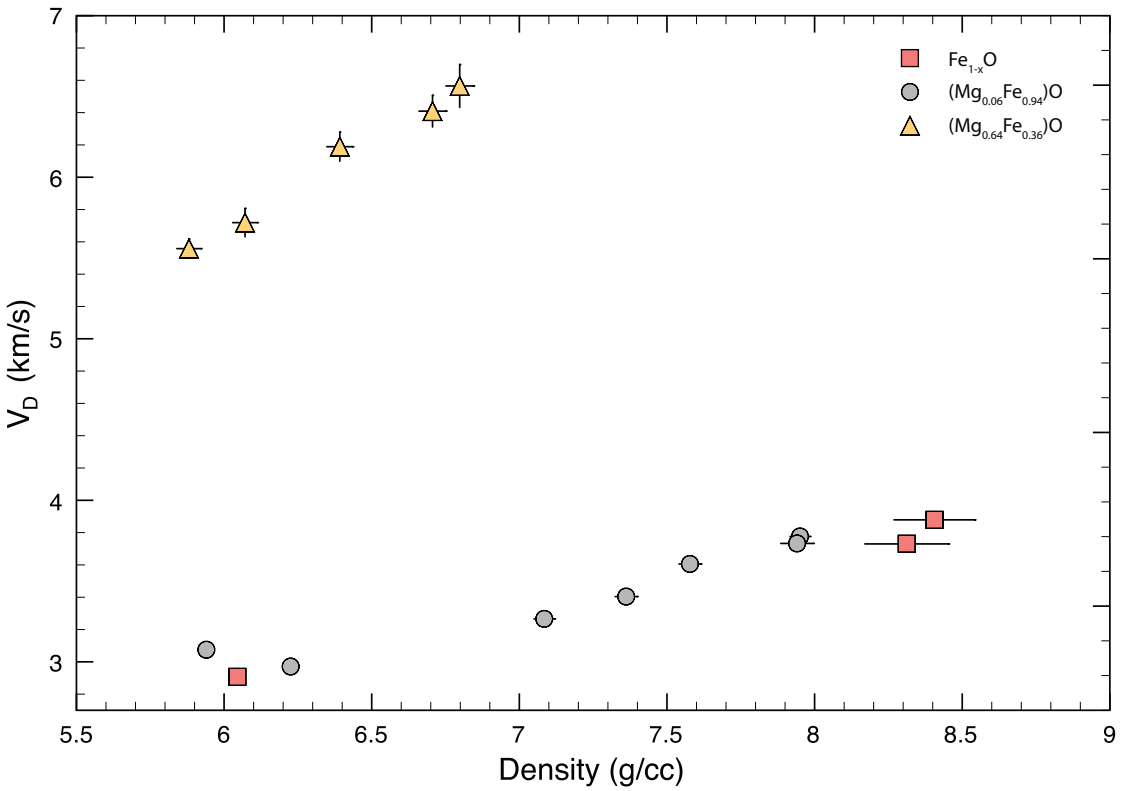

Figure 3.12: (V_D) of $(Mg_{0.06}Fe_{0.94})O$ compared to FeO (Section A.3) and $(Mg_{0.65}Fe_{0.35})O$ (*Chen et al.*, 2012) at 300 K, as a function of in-situ density. $(Mg_{0.65}Fe_{0.35})O$ and $(Mg_{0.06}Fe_{0.94})O$ volumes were measured in-situ at Sector 3-ID-B of the Advanced Photon Source (APS). The volumes of FeO were measured at Sector 12.2.2 of the Advanced Light Source (low density) and at Sector 13-ID-D of the APS (high density). $(Mg_{0.16}Fe_{0.84})O$ is not included in this figure as its volume was not measured in-situ at either Sector 3-ID-B or Sector 13-ID-D.

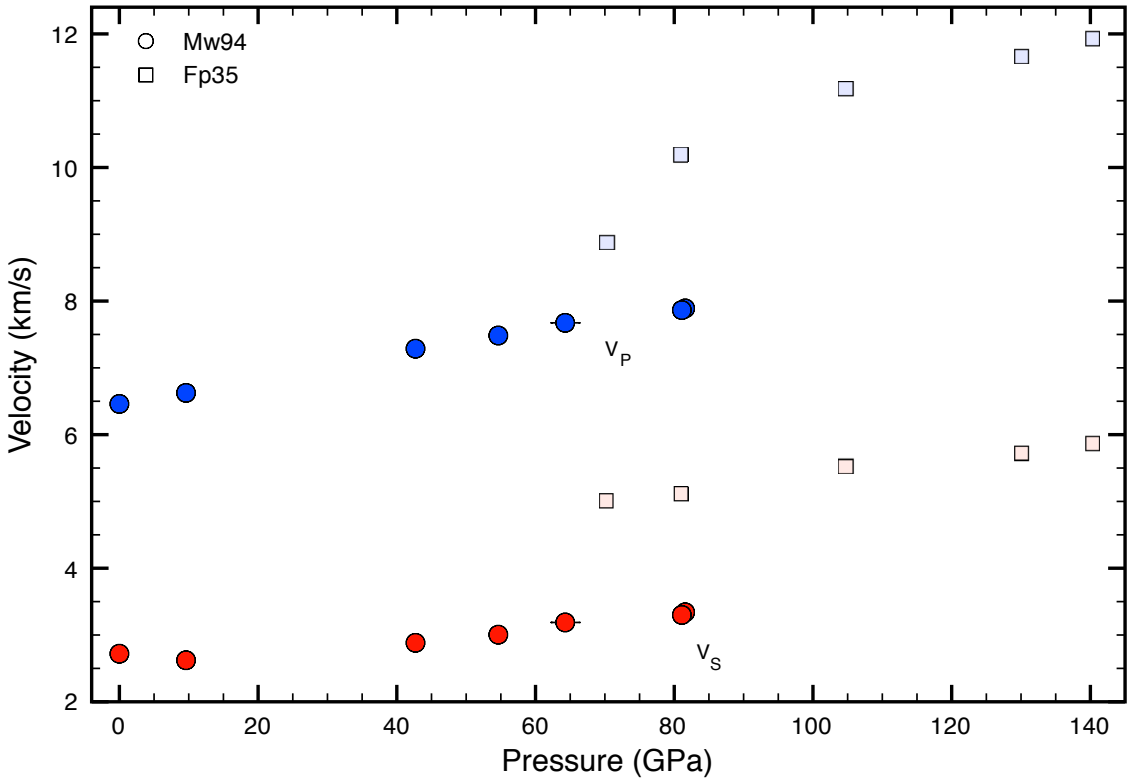

Figure 3.13: Compressional (V_P, red) and shear (V_S, blue) wave velocities of $(Mg_{0.06}Fe_{0.94})O$ at 300 K, over the pressure range 0 to 82 GPa (circles). For comparison, the velocities of $(Mg_{0.65}Fe_{0.35})O$ are shown as light blue and red squares(*Chen et al.*, 2012).

$\rho^{a,b}$ (g/cc)	Pressure^c (GPa)	V_D (km/s)	V_P (km/s)	V_S (km/s)	G (GPa)	K (GPa)
5.93(2)	0	3.08(1)	6.47(5)	2.72(1)	43.9(4)	189(3)
6.23(3)	9.61(2)	2.97(2)	6.63(6)	2.62(2)	42.8(7)	216(4)
7.08(4)	42.7(7)	3.27(2)	7.29(8)	2.88(2)	58.9(8)	288(7)
7.36(4)	55(1)	3.40(2)	7.48(8)	3.01(2)	66.5(9)	324(8)
7.58(4)	64(2)	3.61(2)	7.67(8)	3.19(2)	77.0(9)	344(8)
7.95(3)	81.6(7)	3.78(2)	7.89(9)	3.34(2)	89(1)	377(9)
7.94(6)	81.1(8)	3.73(2)	7.87(9)	3.30(2)	86.5(8)	376(9)

Table 3.5: Summary of sound velocities and bulk and shear moduli of $(Mg_{0.06}Fe_{0.94})O$ as a function of pressure. V_P and V_S are shown in Figure 3.13. ^{a} Number in parenthesis is the error on the last digit. ^{b}From Table 3.4. ^{c}Pressure is determined from the equation of state of $(Mg_{0.06}Fe_{0.94})O$, summarized in Table 3.3.

Chapter 4

Thermal Equation of State of $(Mg_{0.06}Fe_{0.94})O$

4.1 Introduction

In the previous two chapters, we carried out nuclear resonant spectroscopy and X-ray diffraction on iron-rich (Mg,Fe)O at 300 K and reported properties as a function of pressure and composition. In this chapter, we explore this material in yet another dimension, temperature, measuring the equation of state of $(Mg_{0.06}Fe_{0.94})O$ at high pressures and temperatures. This study will allow us to explore the phase diagram and density of iron-rich (Mg,Fe)O at pressures and temperatures approaching those of Earth's core-mantle boundary region.

4.2 Previous Studies

Previous pressure-volume-temperature ($P - V - T$) studies have shown that the MgO-FeO solid solution is complicated by the existence of phase transitions, a spin transition, and defect clustering as a function of FeO component. The MgO endmember is known to be cubic even beyond the pressure and temperature conditions of the earth's mantle (*Duffy and Ahrens*, 1993). The FeO endmember is thought to be cubic at the pressures and temperatures of the interior of the earth, but at lower temperatures is found to transform to rhombohedral structure at moderate pressures (*Shu et al.*, 1998a, e.g.) and then to the $B8$ NiAs structure at higher pressures (*Fei and Mao*, 1994;

Fischer et al., 2011b, e.g.).

Iron-rich (Mg,Fe)O undergoes a cubic to rhombohedral phase transition at 8-40 GPa, with a phase transition pressure sensitive to both composition and hydrostaticity (Figure 3.1). Studies of the bulk modulus at 0 GPa as a function of composition show differing trends due to sample stoichiometry. Studies of non-stoichiometric, iron-rich (Mg,Fe)O show that both K_S and K_T decreases as a function of Fe concentration (*Jacobsen et al.*, 2002; *Richet et al.*, 1989), where K_S is determined from direct measurements of volume, composition, and of V_P and V_S using ultrasonic interferometry, and K_T is determined in a $P-V$ compression study. The trend is opposite for stoichiometric samples, where ultrasonic interferometry studies for iron-poor samples display a positive trend of K_S with increasing iron content (*Jacobsen et al.*, 2002). In the iron endmember, K_T does indeed depend on stoichiometry, with $Fe_{0.99}O$ being much less compressible than $Fe_{<0.98}O$ (*Zhang*, 2000).

Thermal expansion, $\alpha = \frac{1}{V}(\frac{\delta V}{\delta T})_P$ has been shown to be insensitive to Fe content for Mg-containing ferropericlase (*Zhang and Kostak Jr*, 2002). Yet, it appears to be sensitive to defect concentration. In the Fe end member, α is about 30% larger for $Fe_{0.942}O$ than $Fe_{0.987}O$ (*Zhang and Zhao*, 2005). In this study, we aim to measure the $P-V-T$ equation of state $(Mg_{0.06}Fe_{0.94})O$, first to constrain the thermoelasticity of iron-rich (Mg,Fe)O and second to see if these trends apply to the equation of state of iron-rich (Mg,Fe)O.

4.3 Experimental Details

Two experiments were conducted in this study. For the unbuffered experiment, a symmetric diamond anvil cell with 300 μm-culet diamonds was prepared. $(Mg_{0.06}Fe_{0.94})O$ was lightly ground with NaCl powder (1:1 by volume) in an agate mortar under ethanol, allowed to dry, then pressed into a pellet. This mixture was loaded between two thin NaCl plates (<10 μm), and the remaining space in the rhenium gasket sample chamber was filled with neon using the COMPRES/GSECARS gas-loading system (*Rivers et al.*, 2008). To keep the NaCl dehydrated, the pellet was consistently stored in a desiccator when not in use, and the loaded diamond anvil was placed under vacuum for about one hour and purged with argon before being put into the gas-loading system. In a second high

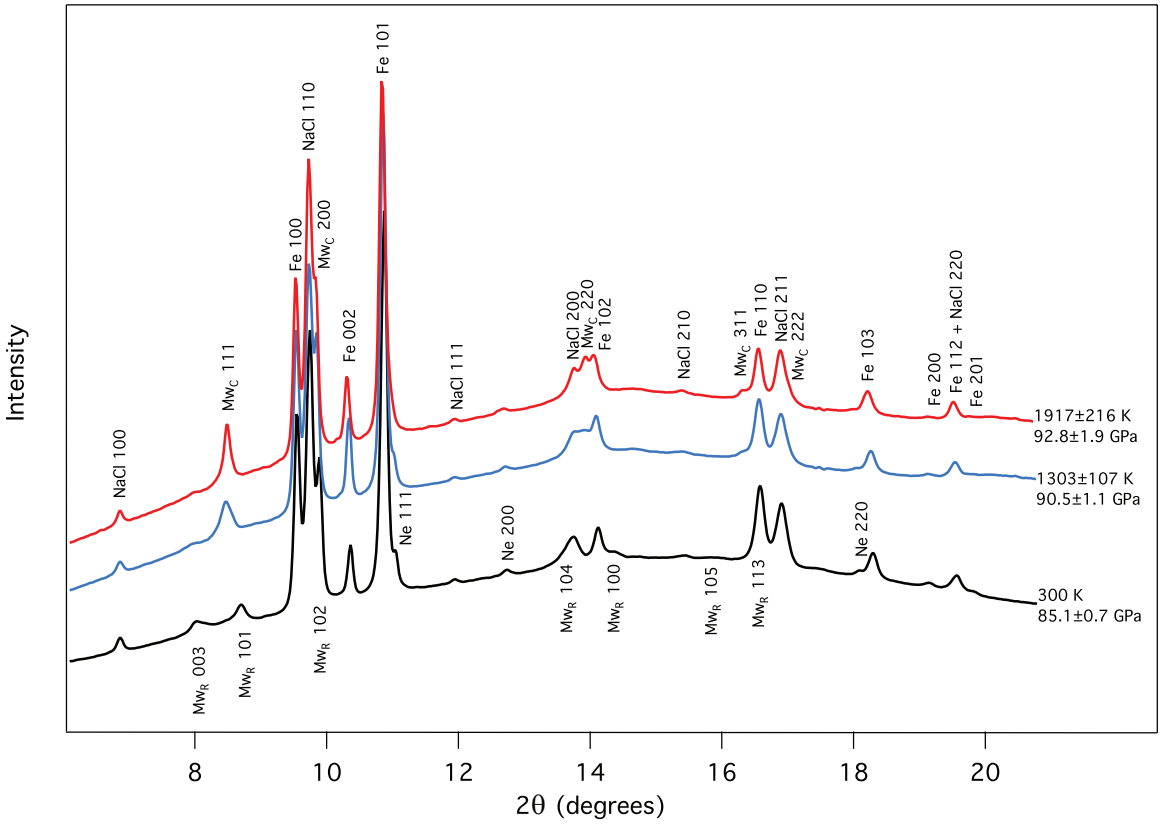

Figure 4.1: Example XRD spectra at 85 GPa showing peak identifications for $B2$-NaCl, *hcp*-Fe, and Ne. $(Mg_{0.06}Fe_{0.94})O$ is rhombohedral at room temperature (Mw_R, *R-3m*) and cubic at high temperature (Mw_C, *Fm-3m*). Pressures listed were determined by the equation of state of *hcp*-Fe (*Dewaele et al.*, 2006; *Murphy et al.*, 2011)

pressure experiment, 250 μm-culet diamonds were used. Otherwise, the preparation differed in that the sample pellet also included a Fe metal (1:1 Mw94:Fe by weight) as an in-situ oxygen buffer and pressure marker.

The high temperature powder diffraction experiments were conducted at the 13-ID-D beamline (GSECARS) at the Advanced Photon Source, Argonne National Laboratory. High temperatures were achieved in-situ by laser heating from both sides with a split infrared fiber laser (*Prakapenka et al.*, 2008) with temperature determined spectroradiametrically on both up and downstream sides (e.g. *Heinz and Jeanloz*, 1987). Using an incident X-ray beam of $\lambda = 0.3344$ Å, angle-dispersive X-ray diffraction patterns were recorded onto a MAR165 CCD detector and subsequently integrated using Fit2D (*Hammersley et al.*, 1996). Example spectra are shown in Figure 4.1.

The 2θ angles corresponding to lattice reflections of $(Mg_{0.06}Fe_{0.94})O$, NaCl, Fe, and Ne were determined by fitting the spectra with Voigt peaks using Igor Pro (WaveMetrics, Lake Oswego, OR, USA). Unit cell volumes were determined using unweighted linear regression using the *Unit Cell* refinement software package (*Holland and Redfern*, 1997), which assumes a minimum uncertainty of 0.005 degrees on each lattice reflection, with errors on the unit cell weighted by goodness of fit. The $B2$-NaCl thermal equation of state of *Fei et al.* (2007b) was used to determine pressure in the unbuffered experiment, and to compare that dataset to the buffered experiment. Pressures in the second experiment were determined using the unit cell volume of *hcp*-iron. We used the Fe equation of state given by *Dewaele et al.* (2006) for the data collected at 300 K, and the quasiharmonic thermal pressure given by *Murphy et al.* (2011). The difference between the two pressure scales is small, with a resulting pressure increase of 0.01 to 0.4 GPa for the *Murphy et al.* (2011) values.

To determine temperature and error of our measurements, we took the average and standard deviation of multiple temperature measurements, which are known to have a precision of 100 K (*Shen et al.*, 2001). Errors in temperature and unit cell of NaCl and *hcp*-Fe were propagated into error in pressure assuming a Gaussian distribution of errors in a simple Monte Carlo error propagation. In the buffered experiment, the discrepancy between measured upstream and downstream temperatures, and the sharp diffraction peaks that show there is no temperature gradient, made it clear that we could not assume a Gaussian distribution. In order to not place undo constraints on the supposed temperature distribution, we used a flat distribution in the error propagation. Calculated volumes and pressures of the buffered dataset are presented in Table 4.1. Calculated volumes and pressures of the unbuffered dataset are presented in Table 4.2.

4.4 Results

4.4.1 Phase Identification

In the P–T range of study, we identified cubic (Mg,Fe)O at high temperature and rhombohedral or a mixture of rhombohedral and cubic (Mg,Fe)O at room temperature. We interpret the mixture to be

Table 4.1: Pressure-volume-temperature data for the buffered experiment. [a]Pressure was determined by the equation of state of *hcp*-Fe from *Dewaele et al.* (2006) and *Murphy et al.* (2011).

Pressure[a] (GPa)	Temperature (K)	Vol_{Mw94} (Å^3)	Vol_{NaCl} (Å^3)	Vol_{Fe} (Å^3)
116.5(7)	1056(13)	6.94(3)	20.10(2)	16.50(2)
118(1)	1218(85)	6.94(2)	20.13(3)	16.50(2)
118.0(9)	1295(124)	6.95(2)	20.11(2)	16.51(2)
119(1)	1436(191)	6.95(2)	20.12(3)	16.53(2)
120(2)	1649(278)	6.95(2)	20.11(2)	16.55(2)
102.5(4)	1124(29)	7.17(1)	20.86(2)	16.90(1)
103.0(4)	1212(15)	7.17(2)	20.87(2)	16.90(1)
103.8(4)	1370(36)	7.19(2)	20.89(2)	16.92(1)
104.8(6)	1563(108)	7.19(1)	20.89(2)	16.94(1)
105.5(6)	1646(109)	7.19(2)	20.89(2)	16.94(1)
106.4(9)	1852(166)	7.20(2)	20.90(2)	16.97(1)
95.0(5)	1184(61)	7.26(3)	21.5(1)	17.13(1)
95.3(7)	1296(139)	7.29(1)	21.45(9)	17.16(1)
96(1)	1426(193)	7.30(2)	21.5(1)	17.18(1)
97(1)	1620(228)	7.34(1)	21.5(1)	17.19(1)
90.2(6)	1201(111)	7.40(2)	21.66(2)	17.29(1)
90.5(6)	1303(107)	7.43(2)	21.68(2)	17.31(1)
91.2(7)	1459(130)	7.43(3)	21.68(2)	17.33(1)
93(1)	1707(204)	7.45(2)	21.69(2)	17.36(1)
93(1)	1807(246)	7.45(2)	21.70(2)	17.37(1)
93(1)	1917(216)	7.43(1)	21.71(2)	17.40(1)
84.5(7)	1105(119)	7.52(3)	21.98(4)	17.45(1)
84.4(8)	1162(144)	7.52(3)	22.00(3)	17.48(2)
84.7(8)	1270(152)	7.52(2)	22.00(3)	17.50(1)
85(1)	1379(193)	7.54(3)	21.98(2)	17.52(1)
77.3(6)	1051(64)	7.65(2)	22.44(3)	17.70(2)
77.5(8)	1135(130)	7.66(2)	22.45(3)	17.71(2)
79(1)	1332(193)	7.66(2)	22.45(3)	17.73(2)
79(1)	1460(260)	7.66(1)	22.47(3)	17.75(2)
75.7(7)	1089(145)	7.70(1)	22.69(2)	17.77(1)
76(1)	1169(211)	7.71(1)	22.65(2)	17.78(1)
77(1)	1285(247)	7.72(1)	22.67(2)	17.79(1)
77(1)	1356(298)	7.72(1)	22.66(3)	17.80(1)
77(2)	1490(346)	7.74(1)	22.67(3)	17.83(1)
72.4(8)	1119(155)	7.80(2)	23.00(3)	17.90(1)
73(1)	1179(211)	7.81(2)	23.02(3)	17.91(1)
73(1)	1268(275)	7.81(3)	23.05(4)	17.92(1)
74(1)	1454(277)	7.81(2)	23.04(3)	17.94(1)
75(2)	1626(359)	7.81(2)	23.06(2)	17.97(1)
75(2)	1604(350)	7.81(1)	23.03(3)	17.97(1)
60.1(8)	1131(128)	8.05(2)	24.02(7)	18.41(2)
60.4(8)	1205(156)	8.05(2)	24.03(6)	18.42(2)
61(1)	1364(189)	8.06(2)	24.01(4)	18.45(2)
62(1)	1520(265)	8.06(2)	24.04(4)	18.47(1)
63(1)	1671(308)	8.07(2)	24.06(4)	18.50(1)
53.9(7)	1136(100)	8.21(1)	24.74(5)	18.70(3)
54.2(9)	1205(141)	8.22(1)	24.74(6)	18.71(3)
55(1)	1356(247)	8.22(1)	24.72(7)	18.72(3)
56(1)	1466(255)	8.23(1)	24.76(6)	18.74(2)
56(1)	1558(291)	8.23(1)	24.75(6)	18.75(2)
57(1)	1631(308)	8.23(1)	24.77(7)	18.76(2)
51(1)	1311(245)	8.33(1)	25.29(4)	18.94(2)
50.0(8)	1177(164)	8.32(1)	25.27(4)	18.91(2)
51(2)	1435(328)	8.34(1)	25.31(3)	18.95(2)
38.4(4)	1324(51)	8.69(1)	27.07(7)	19.63(2)
38.7(6)	1370(76)	8.69(1)	27.12(4)	19.63(3)
39.0(7)	1416(122)	8.70(1)	27.11(6)	19.64(3)
40(1)	1581(246)	8.72(1)	27.15(6)	19.65(3)
40(1)	1643(294)	8.72(1)	27.13(7)	19.66(2)
33.1(4)	300	8.58(3)	26.99(5)	19.50(2)

Table 4.2: Pressure-volume-temperature data for the unbuffered experiment. [a]Pressure was determined from the equation of state of $B2$-NaCl (*Fei et al.*, 2007b).

Pressure[a] (GPa)	Temperature (K)	Vol_{Mw94} ($Å^3$)	Vol_{NaCl} ($Å^3$)	Pressure[a] (GPa)	Temperature (K)	Vol_{Mw94} ($Å^3$)	Vol_{NaCl} ($Å^3$)
71.5(4)	1227(11)	7.77(2)	22.84(3)	55(1)	1396(42)	8.22(3)	24.6(1)
71.7(6)	1312(14)	7.78(2)	22.85(5)	55(1)	1579(16)	8.23(2)	24.6(1)
72.0(5)	1442(28)	7.79(2)	22.88(4)	56(1)	1670(24)	8.23(1)	24.6(1)
71.4(4)	1208(23)	7.77(2)	22.85(3)	56(1)	1731(9)	8.24(1)	24.6(1)
71.7(5)	1317(27)	7.78(2)	22.86(4)	51.9(5)	300	8.09(5)	24.37(6)
71.9(4)	1413(26)	7.78(2)	22.88(4)	54.4(8)	1140(21)	8.15(8)	24.49(8)
70(1)	1192(44)	7.85(5)	22.99(8)	54.7(6)	1239(6)	8.16(6)	24.51(7)
70.0(9)	1306(62)	7.84(3)	23.00(5)	55.4(6)	1437(16)	8.18(3)	24.52(6)
70.5(7)	1433(19)	7.85(1)	23.01(5)	55.3(8)	1483(53)	8.22(1)	24.56(6)
69.9(7)	1173(15)	7.82(3)	22.96(6)	51.9(1)	300	8.06(3)	24.37(1)
70.1(7)	1279(36)	7.83(3)	22.98(4)	47(1)	1195(20)	8.39(4)	25.5(2)
70.5(9)	1396(49)	7.85(3)	22.99(6)	48(1)	1398(34)	8.4(3)	25.5(1)
67.4(9)	1226(28)	7.89(6)	23.21(7)	48.2(9)	1591(24)	8.41(2)	25.5(1)
67.7(7)	1293(17)	7.89(5)	23.21(6)	48.8(9)	1760(26)	8.42(1)	25.51(1)
68.0(6)	1403(20)	7.9(5)	23.22(5)	44.6(7)	300	8.24(3)	25.25(9)
64.9(6)	300	7.77(1)	23.06(5)	45(1)	1248(24)	8.42(5)	25.7(2)
67.4(6)	1180(23)	7.88(5)	23.18(5)	46(1)	1429(15)	8.42(4)	25.7(2)
67.8(5)	1306(7)	7.89(5)	23.20(5)	46(1)	1613(15)	8.44(3)	25.8(2)
67.9(6)	1351(15)	7.89(5)	23.21(5)	47(1)	1705(35)	8.45(2)	25.8(1)
68.1(6)	1420(16)	7.9(4)	23.22(5)	42.5(8)	300	8.34(4)	25.54(1)
63.3(3)	1216(7)	7.96(4)	23.58(2)	41(1)	1186(32)	8.55(2)	26.2(2)
63.6(2)	1295(2)	7.97(4)	23.59(2)	42.0(9)	1387(6)	8.56(2)	26.3(1)
64.1(4)	1412(17)	7.97(3)	23.60(3)	43(1)	1561(33)	8.57(2)	26.3(1)
63.6(2)	1212(10)	7.95(3)	23.55(1)	42.8(8)	1584(12)	8.57(2)	26.3(1)
63.8(3)	1289(11)	7.96(3)	23.57(2)	38.9(6)	300	8.4(3)	26.0(1)
64.1(3)	1430(13)	7.97(3)	23.60(3)	35(1)	300	8.55(7)	26.7(2)
60.5(5)	1215(27)	8.05(5)	23.86(4)	39(1)	1265(35)	8.62(4)	26.7(2)
61.1(2)	1335(14)	8.05(4)	23.86(1)	39(1)	1398(37)	8.63(4)	26.7(2)
61.4(3)	1424(15)	8.05(3)	23.87(3)	39(1)	1395(23)	8.63(4)	26.7(2)
58.2(1)	300	7.91(3)	23.70(1)	40(1)	1562(38)	8.65(4)	26.8(1)
60.9(9)	1210(10)	8.08(8)	23.82(9)	40(1)	1613(28)	8.65(4)	26.8(1)
61(1)	1322(17)	8.04(5)	23.84(9)	35.8(6)	300	8.53(9)	26.5(1)
62.1(8)	1446(23)	8.03(1)	23.81(7)	38.4(9)	1165(51)	8.6(3)	26.7(1)
57.6(3)	1203(24)	8.13(4)	24.16(3)	39(1)	1436(45)	8.63(3)	26.7(2)
58.0(5)	1317(40)	8.13(3)	24.18(3)	39.7(9)	1594(17)	8.65(4)	26.8(1)
58.4(4)	1424(43)	8.13(3)	24.19(2)	35.9(6)	300	8.48(1)	26.5(1)
58.3(4)	1390(20)	8.13(3)	24.18(3)	31.4(6)	300	8.63(4)	27.3(1)
55.1(2)	300	7.93(6)	24.02(2)	34.6(9)	1207(77)	8.72(1)	27.4(1)
57.9(4)	1207(36)	8.11(3)	24.13(2)	35.0(9)	1295(68)	8.73(1)	27.4(1)
58.1(3)	1308(12)	8.12(3)	24.16(2)	35.3(8)	1384(50)	8.76(1)	27.4(1)
58.4(2)	1382(19)	8.12(3)	24.16(1)	35.5(7)	1475(25)	8.77(1)	27.4(1)
58.8(6)	1451(37)	8.13(3)	24.16(5)	31.9(4)	300	8.61(2)	27.19(8)
55.2(2)	300	7.98(3)	24.01(2)	29.8(7)	300	8.62(11)	27.6(1)
55.7(3)	1245(22)	8.18(3)	24.39(2)	33(1)	1224(31)	8.76(2)	27.6(2)
56.2(5)	1337(18)	8.18(2)	24.39(4)	33.6(9)	1454(41)	8.79(1)	27.7(1)
56.1(3)	1371(16)	8.18(2)	24.41(3)	34(1)	1630(31)	8.81(1)	27.8(2)
56.1(4)	1386(32)	8.17(2)	24.41(3)	30.1(4)	300	8.66(4)	27.53(8)
53.0(2)	300	8.02(1)	24.24(2)	31.9(9)	1235(36)	8.75(7)	27.9(2)
55.9(6)	1270(23)	8.15(3)	24.38(6)	32(1)	1384(65)	8.78(5)	28.0(2)
56.1(3)	1346(18)	8.16(3)	24.40(2)	32.4(9)	1526(21)	8.82(4)	28.0(2)
56.4(3)	1422(15)	8.17(2)	24.40(3)	32.4(7)	1391(60)	8.79(4)	27.93(9)
53.0(2)	300	8.03(2)	24.24(2)	32.8(5)	1510(31)	8.81(4)	27.95(8)
54(2)	1224(38)	8.21(4)	24.6(2)				

a result of incomplete back-transformation of cubic to rhombohedral phase on quench. We plot our results in Figure 4.2. Our before-heating points are shown in gray, bracketing the room temperature cubic-rhombohedral transition between 13 and 24 GPa. Representative error bars (bottom right) show the discrepancy in average standard deviation of temperature measurements between the two experiments.

The phase identifications presented in Figure 4.2 are consistent with previous results in that there is no observable $B8$-structured $(Mg_{0.06}Fe_{0.94})O$ in the pressure and temperature range studied (*Kondo et al.*, 2004). Our study, however, disagrees with the location of the rhombohedral-cubic phase boundary of iron-rich (Mg,Fe)O at high temperature. Where we find no evidence of rhombohedral $(Mg_{0.06}Fe_{0.94})O$ at the high temperatures explored in our study, *Kondo et al.* (2004) find a transition of cubic to rhombohedral $(Mg_{0.1}Fe_{0.9})O$ and $(Mg_{0.05}Fe_{0.95})O$ at 1100 to 1500 K, 70 to 100 GPa (Figure 4.2).

4.4.2 Equations of State

The buffered and unbuffered datasets were fit to a 3rd-order Birch-Murnaghan equation of state using EOSFIT (*Angel*, 2000), with the following relations:

$$P(V) = 3K_0 f_E (1+2f_E)^{\frac{5}{2}} \left\{ 1 + \frac{3}{4}(K_0' - 4) f_E \right\} \tag{4.1}$$

$$f_E = \frac{1}{2}\left[\left(\frac{V_0}{V} \right)^{\frac{2}{3}} - 1 \right] \tag{4.2}$$

$$V_0(T) = V_0(T_0) \exp(\alpha_0 (T - T_0)) \tag{4.3}$$

$$K(T) = K_0 + (T - T_0) \left(\frac{\partial K}{\partial T} \right)_P \tag{4.4}$$

where P is pressure in GPa, K_0 is the bulk modulus in GPa at the reference pressure, in our case the isothermal bulk modulus at either 0 or 30 GPa, f_E is Eulerian strain, V and V_0 are volume and initial volume, respectively, in units of $Å^3$/atom. In the high temperature formulation (Equations

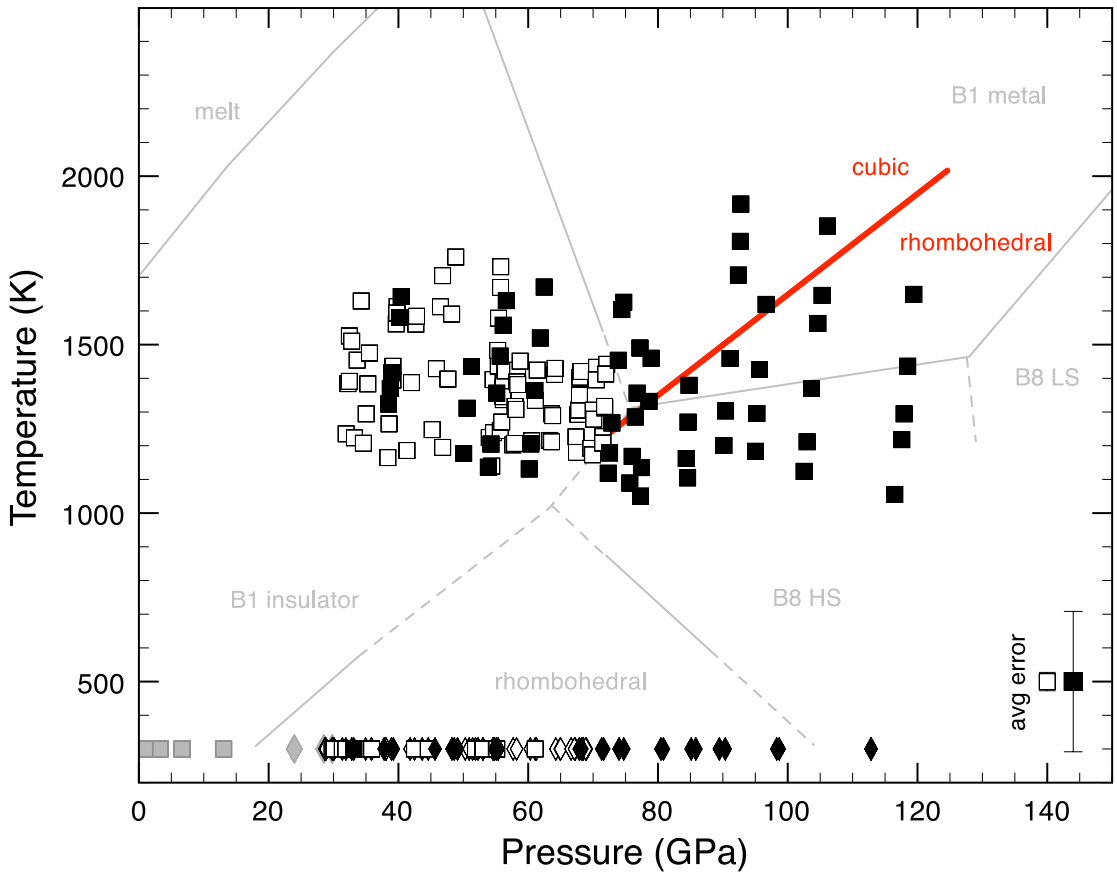

Figure 4.2: Phase identification of $(Mg_{0.06}Fe_{0.94})O$ in P–T space. $(Mg_{0.06}Fe_{0.94})O$ is cubic (unbuffered: white boxes, buffered: black boxes) at high temperature and rhombohedral (unbuffered: white diamonds, buffered: black diamonds) at room temperature, with exception of some quench measurements that contained a mixture of cubic and rhombohedral phases. Before-heating points are shown below 25 GPa in gray. Light gray lines: the latest phase diagram of wüstite (*Fei and Mao*, 1994; *Fischer and Campbell*, 2010; *Fischer et al.*, 2011b,a; *Kondo et al.*, 2004; *Ozawa et al.*, 2010, 2011). Red line: rhombohedral-cubic phase boundary of $(Mg_{0.1}Fe_{0.9})O$ and $(Mg_{0.05}Fe_{0.95})O$ measured by *Kondo et al.* (2004). Representative error bars are also shown in the lower right corner.

Table 4.3: 3rd-order Birch-Murnaghan equation of state parameters for the buffered dataset using *hcp*-Fe as a pressure marker (*Dewaele et al.*, 2006; *Murphy et al.*, 2011). Reference pressure of either 0 or 30 GPa result in equivalent equations of state.

	$P_0 = 0$ GPa	$P_0 = 30$ GPa
V_0 (Å^3)	9.88(9)	8.6(3)
K_{0T} (GPa)	193(14)	275(11)
K'_{0T}	3.0(2)	2.6(2)
$\alpha_0(\times 10^{-5}$ K$^{-1})$	4.2(7)	3.2(4)
$\partial K/\partial T$ (GPa/K)	−0.017(6)	−0.021(7)

4.3,4.4), T and T_0 are temperature and reference temperature, respectively, in Kelvin, α_0 is the thermal expansion coefficient, in units of K^{-1}, and $\partial K/\partial T$ is the isobaric temperature derivative of the bulk modulus, in units of (GPa/K).

The equation of state of the buffered dataset (32 to 117 GPa) was fit using pressures given by the equation of state of hcp-Fe (*Dewaele et al.*, 2006; *Murphy et al.*, 2011, (Table 4.3)).

The fitted V_0 from our study is 9.89(7) Å^3/atom, when using *hcp*-Fe metal as a pressure indicator, which is consistent with our starting material volume of 9.90(1) Å^3/atom, measured on the sample outside of the diamond anvil cell, which in turn is consistent with our Mössbauer measurement showing that Fe^{2^+} is below detection limit ($< 2\%$). The range of fitted K_0 includes that predicted for nearly stoichiometric (Mg,Fe)O (*Jacobsen et al.*, 2002) .

Figure 4.3 shows the results from this buffered experiment, showing volume as a function of pressure and temperature. Also shown are the volumes measured as we compressed the cell before the heating experiment began. We did not include these points in the fit. The steeper $\partial V/\partial P$ of these points, i.e. lower K_0, is more consistent with (Mg,Fe)O containing >2% vacancies (*Zhang*, 2000; *Jacobsen et al.*, 2002).

Table 4.4 shows the fitting results of both buffered and unbuffered datasets with reference pressures of either $P_0 = 0$ GPa or $P_0 = 30$ GPa, using pressure determined by the equation of state of $B2$-NaCl (*Fei et al.*, 2007b).

The limited pressure range (30 to 70 GPa) of the unbuffered dataset proved difficult to fit without external constraints, so we fixed $\partial K/\partial T$ to that of the buffered dataset. If, instead of fixing V_0 of one dataset to the other, we fix K_0 to 180 GPa, the predicted bulk modulus for a stoichiometric

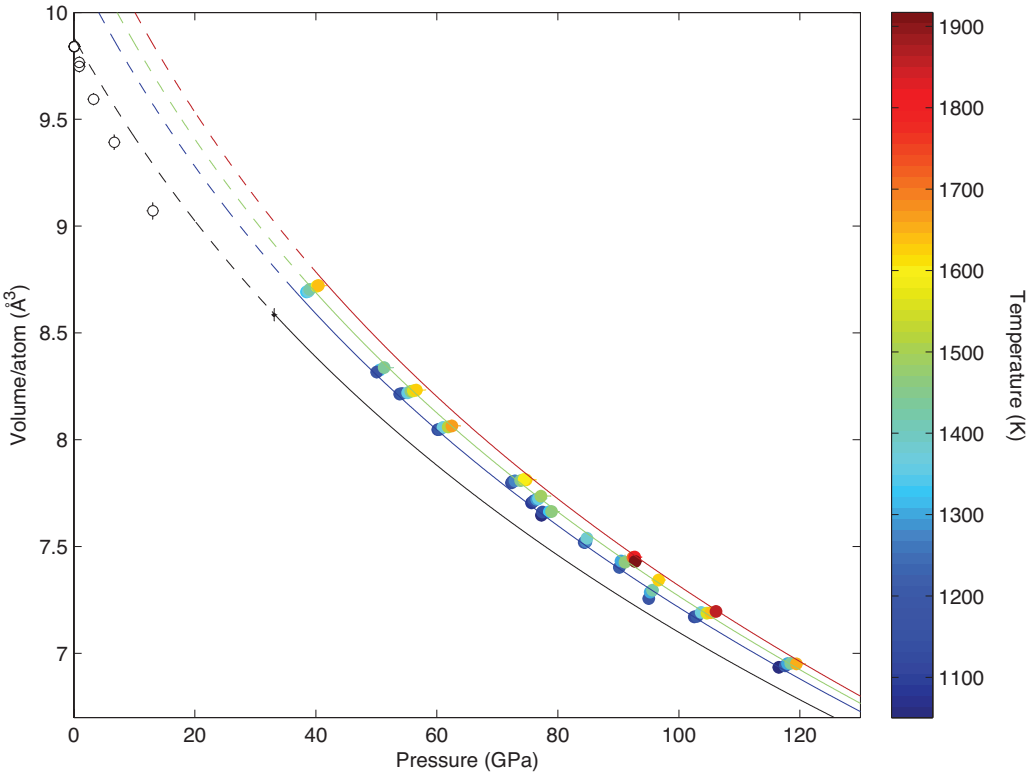

Figure 4.3: $P-V-T$ data and isotherms of $B1$-structured $(Mg_{0.06}Fe_{0.94})O$ in the buffered experiment. Pressures were determined using the equation of state of Fe (*Dewaele et al.*, 2006; *Murphy et al.*, 2011). Open circles: pre-experiment volumes at pressures determined by the equation of state of $B1$-NaCl (JCPDS 5-0628).

Table 4.4: 3rd-order Birch-Murnahan equation of state parameters the both the buffered and unbuffered dataset using $B2$-NaCl as a pressure marker (*Fei et al.*, 2007b). In both cases, the $\partial K/\partial T$ of the unbuffered dataset is fixed to that of the buffered.

	$P_0 = 0$ GPa		$P_0 = 30$ GPa	
	buffered	unbuffered	buffered	unbuffered
V_0 (Å^3)	9.85(8)	9.8(1)	8.69(3)	8.64(1)
K_{0T} (GPa)	202(12)	201(24)	276(9)	283(11)
K'_{0T}	2.7(1)	3.0(4)	2.3(1)	2.6(5)
$\alpha_0(\times 10^{-5}$ K$^{-1})$	3.3(6)	3.6(1)	2.5(4)	2.89(7)
$\partial K/\partial T$ (GPa/K)	−0.013(5)	−0.013 (*fixed*)	−0.016(7)	−0.016 (*fixed*)

Table 4.5: Equation of state parameters using $B2$-NaCl as a pressure marker (*Fei et al.*, 2007b), where we fix K_{0T} to 180 GPa.

	buffered	unbuffered
V_0 (Å^3)	10.0(3)	9.9(1)
K_{0T} (GPa)	180 ($fixed$)	180 ($fixed$)
K'_{0T}	2.95(7)	3.29(6)
$\alpha_0(\times 10^{-5}$ K$^{-1})$	3.0(7)	3.41(7)
$\partial K/\partial T$ (GPa/K)	$-0.010(5)$	-0.010 ($fixed$)

magnesiowüstite (*Jacobsen et al.*, 2002), we again get equation of state parameters that yield values consistent with our previous fits (Table 4.5).

Figure 4.4 shows the results from the unbuffered experiment, showing volume change of $(Mg_{0.06}Fe_{0.94})O$ as a function of pressure and temperature, using NaCl as a pressure marker (*Fei et al.*, 2007b).

4.5 Discussion

4.5.1 Effect of Buffering on Equation of State

In Figure 4.5, we compare the first dataset to the second, showing example volumes and isotherms at 1200, 1500, and 1800 K. At 50 GPa, the calculated thermal expansion coefficients are $\alpha_{buffered} = 2.1(6) \times 10^{-5}$K^{-1} and $\alpha_{unbuffered} = 2.6(1) \times 10^{-5}$K^{-1}.

We first note that the sole room temperature quench point of the buffered dataset is consistent with the unbuffered dataset (Figure 4.5, black filled circle and squares), and the room temperature equations of state are consistent (Table 4.4). The initial thermal expansion coefficient (α_0) of the two datasets are also consistent within error.

The discrepancy between un-annealed (before heating) low pressure and annealed (heated) high pressure measurements suggests a physical difference between cold-compressed and annealed iron-rich (Mg,Fe)O even without an Fe metal buffer. It has been proposed that vacancy concentrations in non-stoichiometric FeO-bearing samples are reduced with the exsolution of $(Fe,Mg)Fe_2O_4$ at high pressure and temperature according to

$$(Mg_xFe_y)O \rightarrow a(Mg_{x'}Fe_{1-x'})Fe_2O_4 + b(Mg_{x''}Fe_{y''})O \tag{4.5}$$

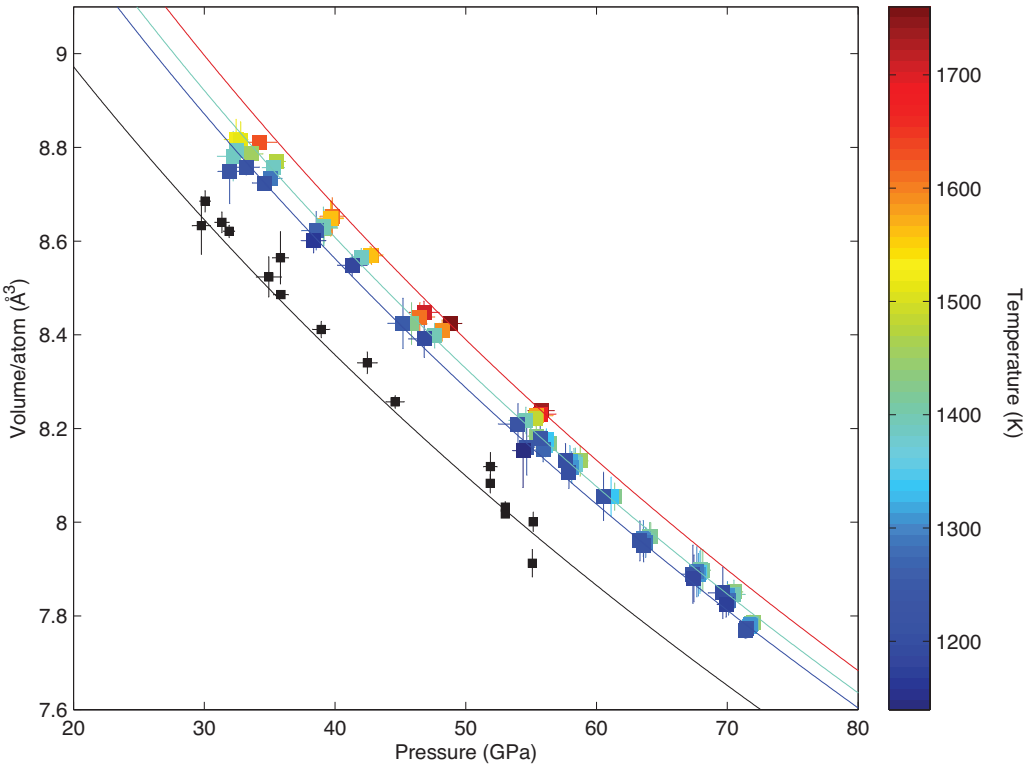

Figure 4.4: $P-V-T$ data and isotherms of $B1$-structured $(Mg_{0.06}Fe_{0.94})O$ in the unbuffered experiment with $\partial K/\partial T$ fixed to that of the buffered experiment. Equation of state parameters corresponding to these curves are those in Table 4.4.

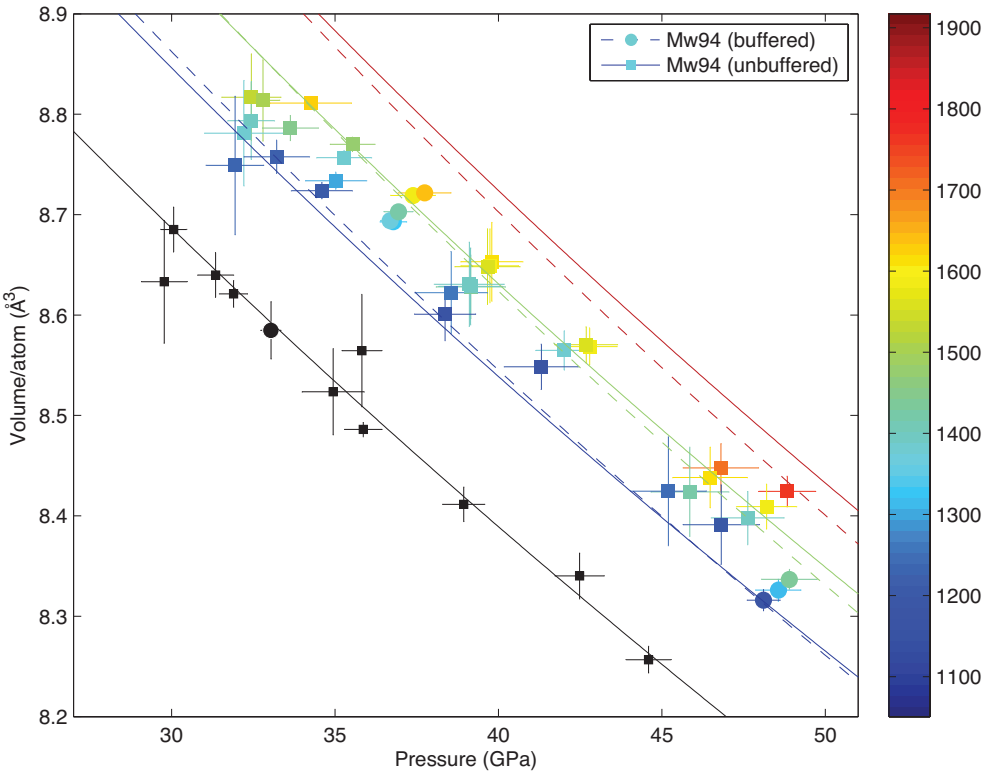

Figure 4.5: Overlay of data and equations of state of $(Mg_{0.06}Fe_{0.94})O$ in both experiments. The unbuffered (squares, solid lines) and buffered (circles, dashed lines) datasets are in good agreement where they overlap in pressure-temperature conditions.

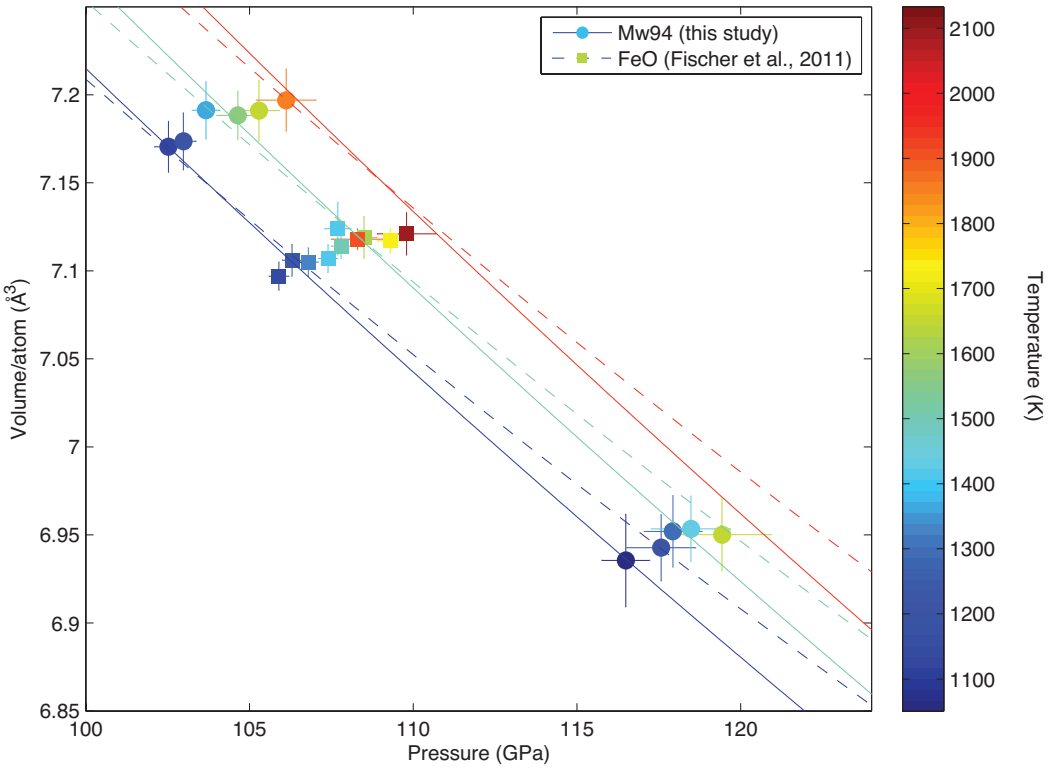

Figure 4.6: Comparison of volume measurements and equations of state of buffered $(Mg_{0.06}Fe_{0.94})O$ (circles, solid lines) to $B1$-FeO (squares, dashed lines) (*Fischer et al.*, 2011b).

where $(x'' + y'') > (x + y)$, ensuring the stoichiometry of the (Mg,Fe)O phase regardless of oxygen fugacity (*Zhang and Zhao*, 2005; *McCammon et al.*, 1998). If this were true in our case, it would also explain the similarity between the buffered and unbuffered datasets at high pressure and temperature.

4.5.2 Effect of Composition on the Thermal Equation of State of (Mg,Fe)O

In Figure 4.6, we compare $(Mg_{0.06}Fe_{0.94})O$ to the equation of state and volumes of FeO (*Fischer et al.*, 2011b) to determine the effect of incorporation of Mg on the equation of state FeO. Both experiments were conducted with in-situ Fe metal buffer/pressure marker. At our highest pressure, 117 GPa, we were not able to discern a difference between the thermal expansion of Mw94 and FeO ($\alpha_{(Mg_{0.06}Fe_{0.94})O} = 1.5(7) \times 10^{-5}$ K^{-1} and $\alpha_{FeO} \approx 1.4(1) \times 10^{-5}$ K^{-1}).

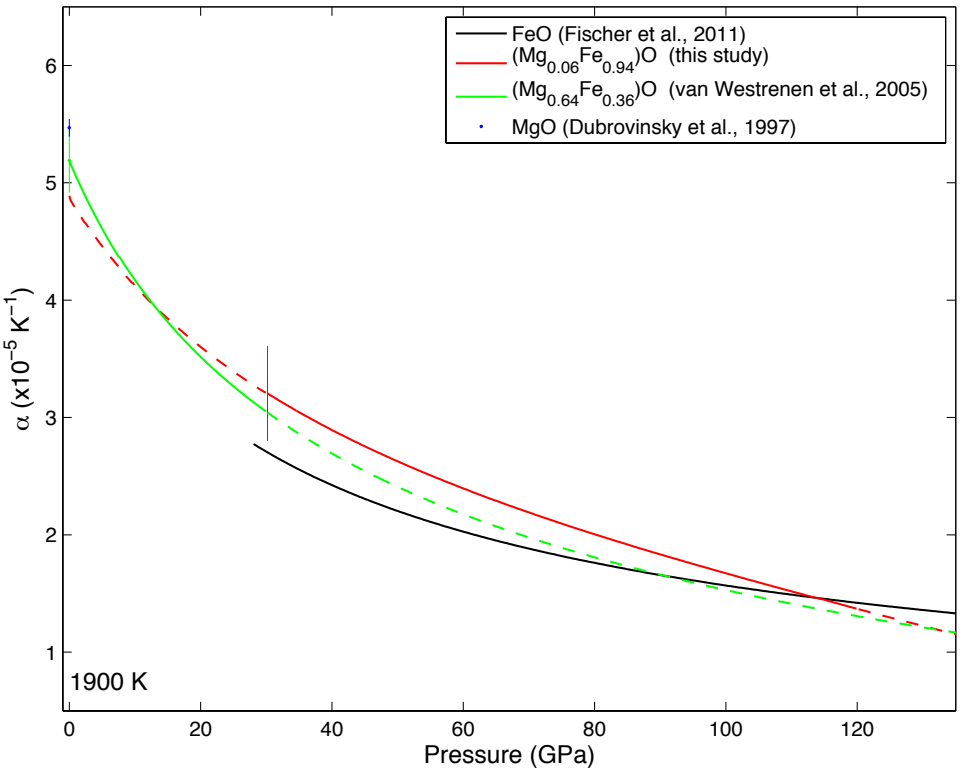

Figure 4.7: Thermal expansion at 1900 K as a function of pressure (Table 4.3), compared to FeO (*Fischer et al.*, 2011b), $(Mg_{0.64}Fe_{0.36})O$ (*Westrenen et al.*, 2005), and MgO (*Dubrovinsky and Saxena*, 1997). Dashed lines show areas of extrapolated curves, and error bars shown are the 1σ error in thermal expansion coefficient.

In Figure 4.7, we plot the thermal expansion of different members of the (Mg,Fe)O solid solution as a function of pressure, at 1900 K. At ambient pressure, the thermal expansion of MgO, $(Mg_{0.64}Fe_{0.36})O$, and FeO vary as a function of composition. Within our experimental uncertainties, we cannot resolve a compositional effect on the thermal expansion of (Mg,Fe)O at high pressures.

Given the different experimental conditions of our buffered and unbuffered datasets, Fe/Mg compositional variation may also be a concern. It is imaginable that buffering with Fe metal could lead to a different Fe/Mg ratio in the (Mg,Fe)O than the mechanism in Equation 4.5 would. However, given that we cannot distinguish $(Mg_{0.06}Fe_{0.94})O$ from FeO, if our buffered $(Mg_{0.06}Fe_{0.94})O$ were slightly enriched in Fe compared to the unbuffered $(Mg_{0.06}Fe_{0.94})O$, we would not know how to distinguish the two without sample recovery.

4.6 Rhombohedral Distortion of $(Mg_{0.06}Fe_{0.94})O$

Volumes and lattice parameters of rhombohedral-structured $(Mg_{0.06}Fe_{0.94})O$ were fit using methods described above. As depicted in Figure 4.2, rhombohedral $(Mg_{0.06}Fe_{0.94})O$ was stable at room temperature at pressures higher than 20 GPa. In the unbuffered experiment, room temperature patterns revealed a mixture of rhombohedral and cubic phases, while in the buffered experiment, only rhombohedrally-structured (Mg,Fe)O was present higher than 34 GPa.

Figure 4.8 shows the evolution of the lattice reflections of $(Mg_{0.06}Fe_{0.94})O$. Before-heating points, shown in gray, show the cubic (111), (200) and (220) reflections that split accordingly: $(111)_C \rightarrow (003)_R+(101)_R$ and $(220)_C \rightarrow (104)_R+(110)_R$. These five reflections were used to refine the unit cell volume. Black circles show measurements of the buffered dataset, and are less scattered than the white circles. Pressure was determined using the (111) and (200) reflections of solid neon (*Dewaele et al.*, 2008) or by the (100), (200), (101), (102), (110), (103), and (112) reflections of *hcp*-iron (*Dewaele et al.*, 2006).

Despite the obvious mismatch between the two datasets in the (003) reflection below 47 GPa, the two datasets appear to agree within scatter above 47 GPa. This observation is more apparent in Figure 4.9, which shows the c/a ratio of the hexagonal unit cell for each measurement. Above 55 GPa, the c/a ratios of the two datasets are indistinguishable. Another observation we note here is the leveling off of the distortion, apparently starting at 70 GPa.

This dataset shown in Figure 4.10, combined with the low-pressure measurements taken at Sector 3-ID-B (Section 3.4.1), was used to constrain the equation of state of $(Mg_{0.06}Fe_{0.94})O$ at 300 K for use in determining the pressure and sound velocities from NRIXS data (see 3.4.1).

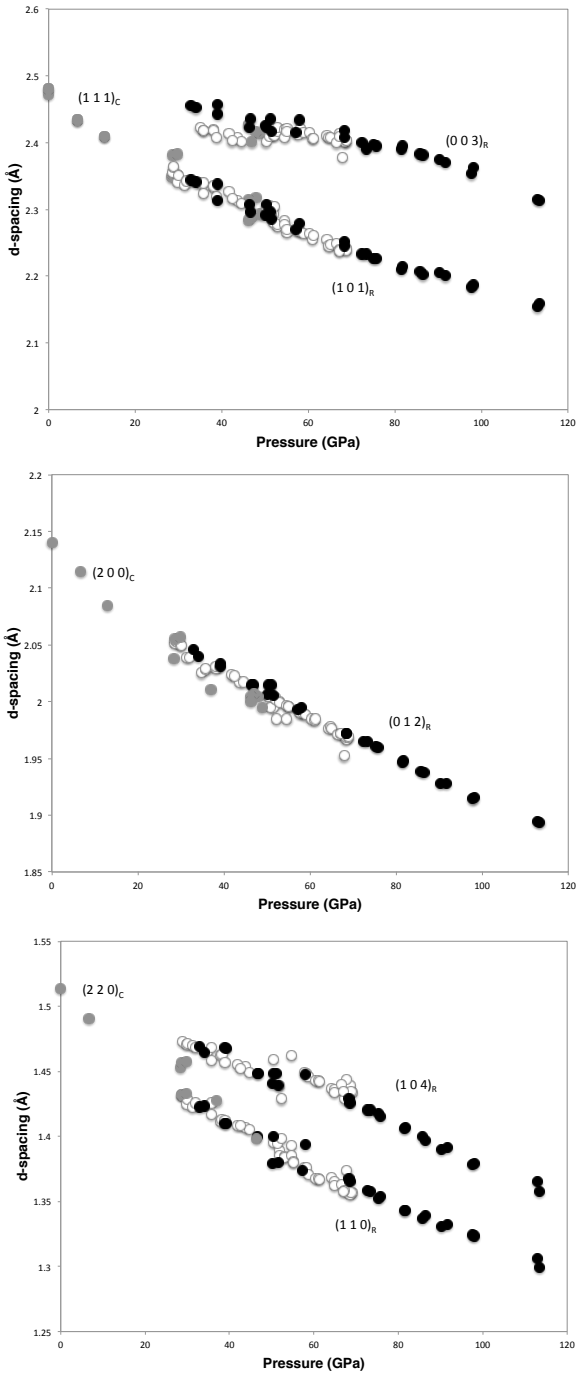

Figure 4.8: Evolution of *d*-spacings of $(Mg_{0.06}Fe_{0.94})O$ as a function of pressure. Gray circles: before heating experiment began. White circles: unbuffered dataset. Black circles: buffered dataset. Pressure was determined from the unit cell of neon (*Dewaele et al.*, 2008).

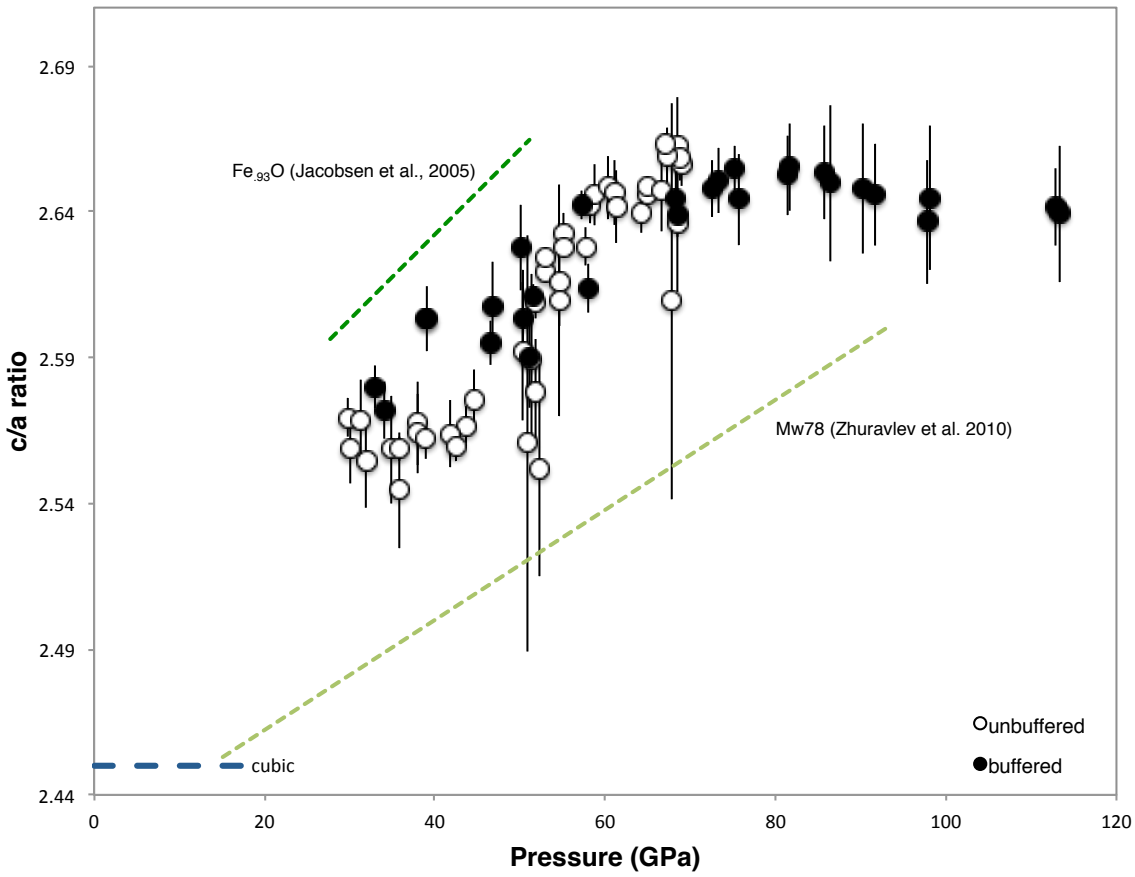

Figure 4.9: Evolution of c/a ratios of rhombohedral $(Mg_{0.06}Fe_{0.94})O$ as a function of pressure at 300 K. White circles: unbuffered dataset. Black circles: buffered dataset. Pressure was determined from the unit cell of neon (*Dewaele et al.*, 2008). Error bars are determined from the unit cell refinement.

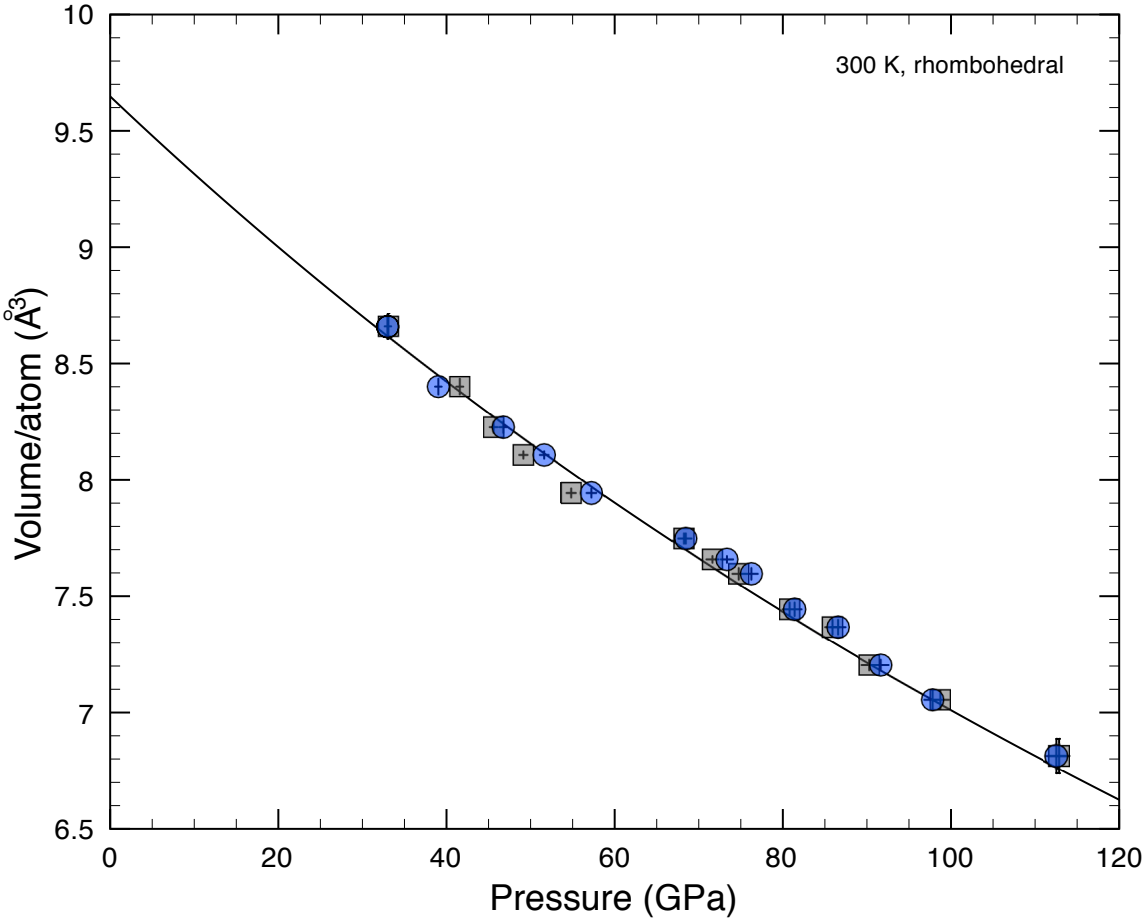

Figure 4.10: Pressure-volume data of quenched, rhombohedral $(Mg_{0.06}Fe_{0.94})O$ at 300 K, with pressure determined either by *hcp*-Fe (*Dewaele et al.*, 2006, gray squares) or Ne (*Dewaele et al.*, 2012, blue circles). Quench points are those after each heating cycle. Black line is a 3rd-order Vinet equation of state fit to the data using pressure determined from the equation of state of neon, where $V_0 = 9.65(7)$ Å^3/atom, $K_{0T} = 281(22)$ GPa, and $K'_{0T} = 0.6(4)$.

Table 4.6: Pressure-volume data for the buffered experiment at 300 K. [a]Pressure was determined from the equation of state of *hcp*-Fe (*Dewaele et al.*, 2006). [b]Pressure was determined from the equation of state of Ne (*Dewaele et al.*, 2008). [c]Volumes of *hcp*-Fe were refined using 7 reflections: (100),(200), (101), (102), (110), (103), and (112). [d]Volumes of Ne were determined using 2 to 3 reflections of (111), (200), and (220). [e]Measurements after each heating cycle is referred to in the text as "quench" points.

P_{Fe}[a] (GPa)	P_{Ne}[b] (GPa)	Vol_{Fe}[c] Å^3	Vol_{Ne}[d] Å^3	Vol_{Mw} Å^3/atom	a_{Mw} Å	c_{Mw} Å	Vol_{NaCl} Å^3
112.8(8)	113(1)	16.45(2)	25.39(7)	6.84(1)	2.612(7)	6.90(3)	20.10(4)
112.9(6)[e]	113.3(9)	16.45(1)	25.36(5)	6.81(5)	2.60(1)	6.87(5)	20.05(4)
98.3(5)	98(2)	16.84(2)	26.4(2)	7.10(5)	2.64(1)	6.99(5)	20.84(2)
98.7(4)[e]	98(3)	16.83(1)	26.4(2)	7.04(4)	2.65(1)	6.98(5)	20.78(2)
89.5(9)	90(2)	17.10(3)	26.9(1)	7.20(7)	2.66(1)	7.05(5)	21.42(9)
90.4(4)[e]	92(1)	17.08(1)	26.8(1)	7.20(6)	2.66(1)	7.04(4)	21.24(2)
85.1(3)	86(1)	17.24(1)	27.3(1)	7.31(5)	2.672(9)	7.09(4)	21.62(3)
85.8(2)[e]	86(2)	17.218(8)	27.2(1)	7.30(6)	2.67(2)	7.08(6)	21.53(2)
80.5(4)	82(1)	17.39(1)	27.66(9)	7.41(5)	2.683(8)	7.13(3)	21.92(3)
80.8(3)[e]	81(1)	17.38(1)	27.7(1)	7.39(4)	2.683(8)	7.12(3)	21.88(3)
74.0(4)	75(1)	17.62(2)	28.3(1)	7.56(3)	2.703(5)	7.17(2)	22.39(3)
74.7(4)[e]	75.8(6)	17.59(1)	28.21(6)	7.56(3)	2.704(6)	7.16(2)	22.31(2)
71.3(3)	73(1)	17.71(1)	28.5(1)	7.63(3)	2.712(8)	7.18(1)	22.62(2)
71.6(4)[e]	73.3(6)	17.70(1)	28.45(6)	7.62(3)	2.71(1)	7.18(2)	22.57(2)
67.9(7)	68(1)	17.84(3)	29.0(1)	7.78(4)	2.731(7)	7.22(2)	22.99(4)
68.3(4)[e]	68(1)	17.83(2)	29.0(1)	7.73(3)	2.727(5)	7.20(2)	22.87(2)
55.4(6)	58(1)	18.35(3)	30.2(1)	8.08(3)	2.777(6)	7.26(2)	23.9(1)
55(1)[e]	57(1)	18.38(5)	30.3(1)	7.94(2)	2.751(3)	7.27(1)	23.88(4)
48.6(6)	50.1(3)	18.66(3)	31.35(5)	8.18(6)	2.78(1)	7.32(3)	24.70(5)
49.1(8)[e]	51.5(2)	18.64(4)	31.12(3)	8.11(2)	2.781(4)	7.26(1)	24.58(3)
48.3(7)	46.5(3)	18.68(4)	31.93(5)	8.22(3)	2.800(6)	7.27(2)	25.15(2)
45.6(4)[e]	46.8(3)	18.81(2)	31.89(5)	8.17(6)	2.79(1)	7.27(3)	25.12(2)
38(1)	39(1)	19.23(4)	33.3(3)	8.47(4)	2.825(7)	7.35(3)	26.27(6)
39(1)[e]	40(1)	19.15(2)	33.2(2)	8.42(1)	2.819(2)	7.34(1)	26.13(2)
33(1)	34(2)	19.52(3)	34.5(4)	8.55(4)	2.845(6)	7.32(2)	26.8(1)
33.1(4)[e]	33(2)	19.50(2)	34.7(5)	8.58(3)	2.846(5)	7.34(2)	26.99(5)

Chapter 5

Implications for Ultralow-velocity Zones

5.1 Physical Mixing Models

To explore the expected sound velocities and density of an ultralow-velocity zone containing iron-rich (Mg,Fe)O, we can construct simple models that combine the properties of iron-rich (Mg,Fe)O and mantle silicates. We show that a small amount of iron-rich (Mg,Fe)O can greatly reduce the average sound velocity of an aggregate assemblage. When combined with a geodynamic model of a solid ULVZ (*Bower et al.*, 2011), we can directly correlate inferred sound velocities to mineralogy and predicted ULVZ shapes. Our combined geodynamic and mineral physics model of a solid ULVZ can be used to explore the relationship between the observed sound velocities and mineralogy of ULVZs with added insight into ULVZ morphology.

5.1.1 Extrapolation of Magnesiowüstite properties to the CMB

Re-evaluation of sound velocities of $(Mg_{.16}Fe_{.84})O$ occurred after publication, which was presented unaltered in Chapter 2. Updates include a re-analysis of the sample, finding the composition to be $(Mg_{0.18}Fe_{0.78}Ti_{0.04})O$. In addition, we assume that equation of state of $(Mg_{.16}Fe_{.84})O$ can be approximated by that of $(Mg_{.06}Fe_{.94})O$, rather than that of $(Mg_{.12}Fe_{.78})O$. This equation of state choice should be more self-consistent, as both samples were made in the exact same way. Updated Debye velocities of $(Mg_{.16}Fe_{.84})O$ are shown in Figure 5.1, underlying those of $(Mg_{.06}Fe_{.94})O$ and

FeO presented in Chapter 3.

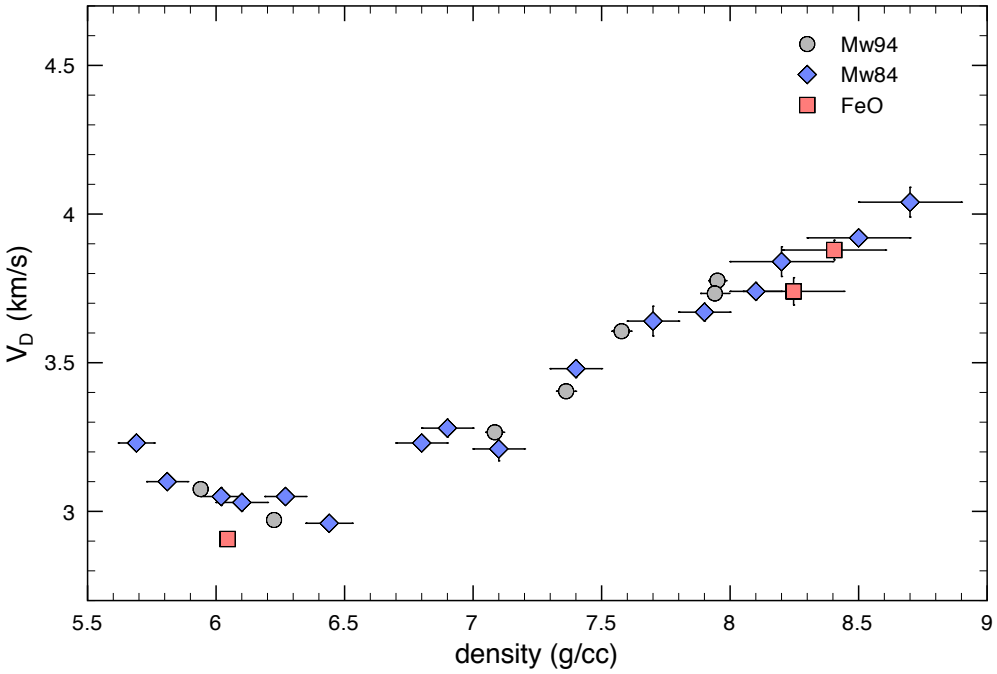

Figure 5.1: Debye velocity as a function of density of $(Mg_{.16}Fe_{.84})O$, $(Mg_{.06}Fe_{.94})O$, and FeO. $(Mg_{0.06}Fe_{0.94})O$ volumes were measured in-situ at Sector 3-ID-B of the Advanced Photon Source (APS). The volumes of FeO were measured at Sector 12.2.2 of the Advanced Light Source (low density) and at Sector 13-ID-D of the APS (high density). The volumes of $(Mg_{0.16}Fe_{0.84})O$ above ambient pressure were not measured, but estimated using ruby pressure, initial volume measured at the ALS, and the equation of state parameters $(Mg_{.06}Fe_{.94})O$: of $K_{0T} = 189(4)$ GPa and $K'_{0T} = 2.9(1)$. Figure updated from Figure 3.12 to include recalculated $(Mg_{.16}Fe_{.84})O$.

The Debye velocities in Figure 5.1 exhibit a linear increase as a function of density above 6.5 g/cc, independent of composition. As the highest density of $(Mg_{.16}Fe_{.84})O$ at 8.7 g/cc corresponds to a pressure of 121 GPa, we extrapolate that this linear trend is valid up to the core-mantle boundary pressure of 135 GPa.

In the latest formulation of the mixing model, presented below, the Debye sound velocities of $(Mg_{.06}Fe_{.94})O$ are linearly extrapolated to 135 GPa. This choice is made for self-consistency reasons, as it is the only dataset with in-situ volumes mapped directly onto its own equation of state. Here we assert that the Debye sound velocity as a function of density of $(Mg_{.16}Fe_{.84})O$ is the same as that of $(Mg_{.06}Fe_{.94})O$, since we cannot discern a difference. This assumption, however, introduces a slight inconsistency in the parameterization of Debye velocity with other compositions, which will

have to be worked out before this model can be published. Namely, this simple extrapolation to the CMB gives a $(Mg_{.16}Fe_{.84})O$ density of 8.63 g/cc, which is lower than the highest density plotted in Figure 5.1.

We estimate the sound velocities of $(Mg_{.16}Fe_{.84})O$ at high temperature by using the temperature derivatives $\partial V_P/\partial T = -4.64\times10^{-4}$ (km s^{-1}K^{-1}) and $\partial V_S/\partial T = -3.85\times10^{-4}$ (km s^{-1}K^{-1}), measured for MgO up to 20 GPa and 1650 K (*Kono et al.*, 2010). Density is adjusted for high temperature using the equation of state we measured on buffered $(Mg_{.06}Fe_{.94})O$ (Chapter 4, Table 4.3).

5.1.2 Mixture of Magnesiowüstite and Ambient Mantle

One such model represents a mixture of iron-rich (Mg,Fe)O and ambient mantle, and is hereafter referred to as "Mw+PREM". Prior versions of this model were published in *Wicks et al.* (2010) (Chapter 2) and updated in *Bower et al.* (2011), and mixes iron-rich oxide with surrounding lower mantle represented by the Preliminary Reference Earth Model (PREM) (*Dziewonski and Anderson*, 1981). This binary mixture can be thought of as a disequilibrium assemblage of lower mantle material mixed with iron-rich oxide.

Considering a physical mixing scenario in which an iron-rich oxide is combined with ambient mantle has two advantages. First, it is generally accepted that a large fraction of the lower mantle is made up of silicate perovskite, due to the fact that the expected sound velocities and density of perovskite largely agree with PREM. Using the seismic velocities and densities of PREM, therefore, should be a good approximation to using sound velocities and densities of perovskite, although it likely represents a mixture of phases. Second, without knowing the mechanism by which a ULVZ is formed, it is conceivable that a ULVZ can simply be a mixture of lower mantle and core material. There is increasing evidence for complexity on the core side of the core-mantle boundary which could be an expression of exsolved "sediments" on the top of the core (*Buffett et al.*, 2000). Therefore, a ULVZ could simply be ambient mantle mixed with FeO, which is what this mixing model represents.

We then calculate the Voigt and Reuss bounds for V_P, V_S, and density (*Watt et al.*, 1976) for a

Table 5.1: Model parameters for mixing model "Mw+PREM"

	V_P (km/s)	V_S (km/s)	density (g/cc)
PREM	13.714	7.2648	5.5613
Mw84 (2700 K)	7.3014	2.705	8.3001
Mw84 (4700 K)	6.3734	1.935	8.2288

given vol% of $(Mg_{.16}Fe_{.84})O$ and PREM at 135 GPa, choosing a low (2700 K) and high (4700 K) temperature estimates of the core-mantle boundary (Figure 5.2). Model parameters are listed in Table **??**. Voigt (uniform stress) and Reuss (uniform strain) bounds bracket the upper and lower bounds of mixing of the bulk modulus K, shear modulus G and density ρ, from which we calculate V_P and V_S using Equation 2.2 and $G = \rho V_S^2$.

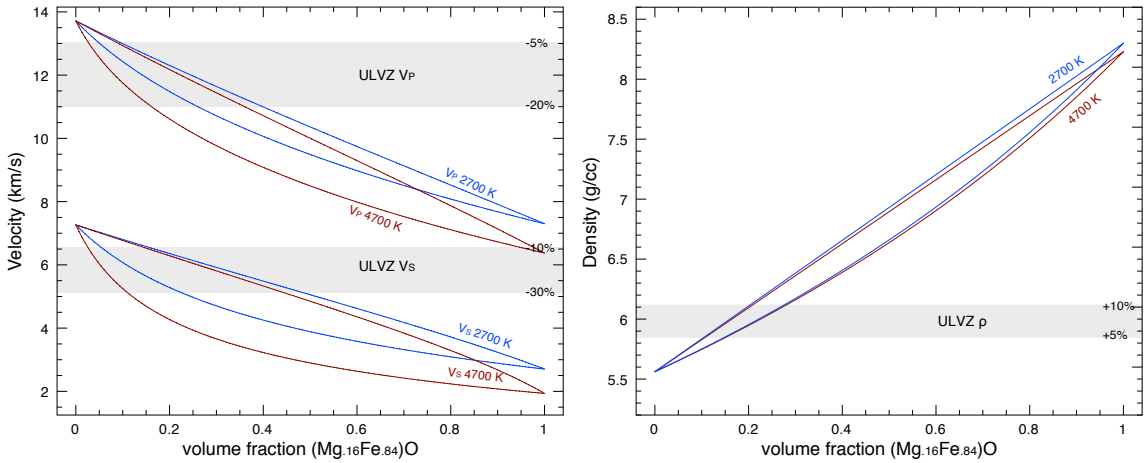

Figure 5.2: Voigt (upper)-Reuss (lower) bounds of V_P, V_S (left), and density (right) of $(Mg_{.16}Fe_{.84})O$ with PREM at 135 GPa. Gray shading shows typical ULVZ velocities (-5-20% V_P, -10-30 %V_S, with respect to surrounding mantle) reported by seismology. Density is not very well constrained by seismology, but have been quoted at +8-10% (*Rost et al.*, 2006; *Idehara et al.*, 2007, e.g.). Dynamic models such as those by *McNamara et al.* (2010) predict ULVZs with densities of at least +5% with respect to surrounding mantle, yet models by *Bower et al.* (2011) create reasonable ULVZs corresponding to less than 5% density increase.

To first order, mixing of just 20 vol% of $(Mg_{.16}Fe_{.84})O$ with 80 vol% silicates (represented here by PREM) matches signature seismic observations for the ULVZ (Figure 5.2).

5.1.3 Mixture of Magnesiowüstite and Silicate Perovskite

A second mixing model, a prior version of which is published in *Bower et al.* (2011), again starts with the assumption that iron-rich oxide is present in a ULVZ and explores a possible equilibrium

assemblage of iron-rich (Mg,Fe)O and perovskite. Hereafter we refer to it as "Mw+Pv".

The partitioning behavior of Fe vs. Mg between the two phases has been probed at lower mantle pressures by numerous studies without much agreement, but recent studies show a preferential partitioning of Fe into the oxide phase, which we adopt: $K_D^{Pv/Mw} \approx 0.07$ (*Auzende et al.*, 2008; *Sakai et al.*, 2009; *Sinmyo et al.*, 2008), assuming an aluminum-free system. In addition to representing the simple phase assemblage that we model in this mixture, a low $K_D^{Pv/Mw}$ is required by this exercise in order to achieve reasonable densities for appropriate velocity decrements. In other words, too much iron in perovskite would create ULVZs denser than those consistent with observed heights, with velocities that are not low enough.

Other studies find the partitioning behavior to be less extreme, determining $K_D^{Pv/Mw} \approx 0.42$ for an assumed "pyrolite" mantle composition, or $K_D^{Pv/Mw} \approx 1.11$ in the presence of post-perovskite (*Sinmyo et al.*, 2011). Partitioning behavior is known to be a function of composition, pressure, and the presence of post-perovskite, but with opposite conclusions between even the most recent studies, $K_D^{Pv/Mw}$ is still an uncertainty (*Sinmyo et al.*, 2011; *Catalli et al.*, 2009).

If we assert that $(Mg_{.16}Fe_{.84})O$ exists at the core-mantle boundary, a coexisting perovskite in equilibrium would have the composition $(Mg_{.72}Fe_{.28})SiO_3$, using $K_D^{Pv/Mw} \approx 0.07$ (*Sakai et al.*, 2009; *Auzende et al.*, 2008). This resulting assemblage is very Fe-rich, and would require a formation mechanism capable of making such an exotic composition. We model the densities and sound velocities of perovskite using a finite-strain model given by *Li and Zhang* (2005), making a compositional correction to the density. Bulk and shear moduli have also been predicted to be compositionally-dependent (*Kiefer et al.*, 2002), but we found the resulting differences to be negligible (*Bower et al.*, 2011).

We calculate the Voigt and Reuss bounds for V_P, V_S and density for a given vol% of $(Mg_{.16}Fe_{.84})O$ and $(Mg_{.72}Fe_{.28})SiO_3$ perovskite at 135 GPa and 2700 and 4700 K (Figure 5.3).

The resulting mixing model is presented in Figure 5.3. Here, at $X_{(Mg,Fe)O} = 0$, we see the temperature dependence of the modeled perovskite in both velocities and densities of the silicate fraction. The range of expected perovskite velocity at the two extreme temperature estimates is

Table 5.2: Model parameters for mixing model "Mw+Pv"

	V_P (km/s)	V_S (km/s)	density (g/cc)
Pv (2700 K)	14.013	7.4287	5.7157
Pv (4700 K)	13.57	6.9129	5.4935
Mw84 (2700 K)	7.3014	2.705	8.3001
Mw84 (4700 K)	6.3734	1.935	8.2288

much larger than the difference between perovskite and PREM, which falls between the two. We conclude that the choice of silicate model (PREM vs (Mg,Fe)SiO_3) then is not distinguishable given the uncertainty in temperature of the CMB region.

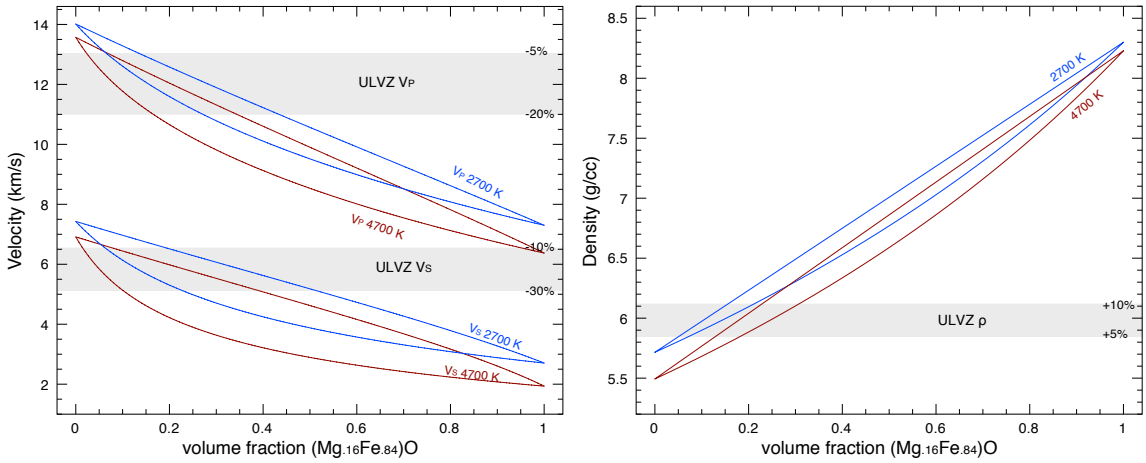

Figure 5.3: Voigt (upper)-Reuss (lower) bounds of V_P, V_S (left), and density (right) of $(Mg_{.16}Fe_{.84})O$ with (Mg,Fe)-perovskite. Gray shading same as in Figure 5.2

In both this model and in Mw+PREM, we find that only about 20% iron-rich magnesiowüstite is needed to drop the sound velocities of an assemblage. The density of perovskite is higher than PREM at 2700, but lower at 4700, so the density of Mw+Pv is greatly affected by temperature choice. As a result, the amount of Mw85 needed to match reported densities according to seismic studies jumps from 15% at 2700 K to 25% at 4700 K.

5.1.4 Dynamics of a Solid-state ULVZ

The mixing models described above show that ULVZ velocities and densities can be adequately represented by a mixture of iron-rich (Mg,Fe)O and perovskite or silicate-rich surrounding mantle. We can take this model one step further by interpreting these models in the context of dynamic

models (*Bower et al.*, 2011, specifically).

We explored the morphologies of solid-state ULVZs in a two-dimensional dynamic model, solving the steady-state thickness and shape of ULVZs as a function of prescribed initial thickness and chemical vs. thermal buoyancy (*Bower et al.*, 2011). By exploring a range of thicknesses and buoyancy numbers B, this study creates a range of candidate ULVZ sizes and shapes that can be mapped to mineral physics models via density and assumed temperature drop across the core-mantle thermal boundary layer, according to the definition of buoyancy number: $B = \frac{Rb}{Ra} = \frac{\Delta\rho_{ch}}{\rho\alpha\Delta T}$, where $\frac{Rb}{Ra}$ is the ratio of chemical to thermal Rayleigh numbers, $\Delta\rho_{ch}$ is the chemical density anomaly of the ULVZ layer, ρ and α are density and thermal expansion of the mantle, and ΔT is the temperature drop across the CMB. More detailed descriptions of the dynamic models are found in *Bower et al.* (2011).

Taking the density calculations of the two mixing models, and assuming a lower bound of ΔT_{CMB} of 500 K and an upper bound of ΔT_{CMB} =1500 K across the thermal boundary layer just above the core-mantle boundary, the range of dynamic models of *Bower et al.* (2011) map to volume fractions of $\sim 0.01 - 0.26$ of $(Mg_{.16}Fe_{.84})O$ for the Mw+PREM model, and $\sim 0.03 - 0.29$ for the Mw+Pv model. These models introduce a new kind of constraint: a much smaller density contrast, and therefore smaller amount of iron-rich (Mg,Fe)O, creates shapes with larger aspect ratios (height/width), whereas a larger density contrast and more iron-rich (Mg,Fe)O generally creates ULVZs that are flat yet wide. A seismic study that constrains the width and size of ULVZs now has a way to constrain density, assuming a solid mixed component.

A recent review of the core mantle boundary suggests that a CMB temperature of $\sim$ 4000 K and a temperature drop across the CMB thermal boundary layer of $\sim$1200-1800K (*Tackley*, 2012) best satisfies combined seismological and mineral physics constraints.Our mixing models, then, can be recalculated at a CMB temperature of 4000 K and ΔT_{CMB} of 1500 K to predict ULVZ morphologies. We plot the Voigt-Reuss-Hill curves in Figure 5.4.

It's important to note that the assumptions we made in these models can be revised as more is learned about the temperature and mineralogy of Earth's core-mantle boundary. The high-iron

Table 5.3: Model parameters for mixing model "Mw+PREM" and "Mw+Pv" at 4000 K

	V_P (km/s)	V_S (km/s)	density (g/cc)
PREM	13.714	7.2648	5.5613
Pv (4000 K)	13.712	7.0886	5.5795
Mw84 (4000 K)	6.6982	2.2045	8.23

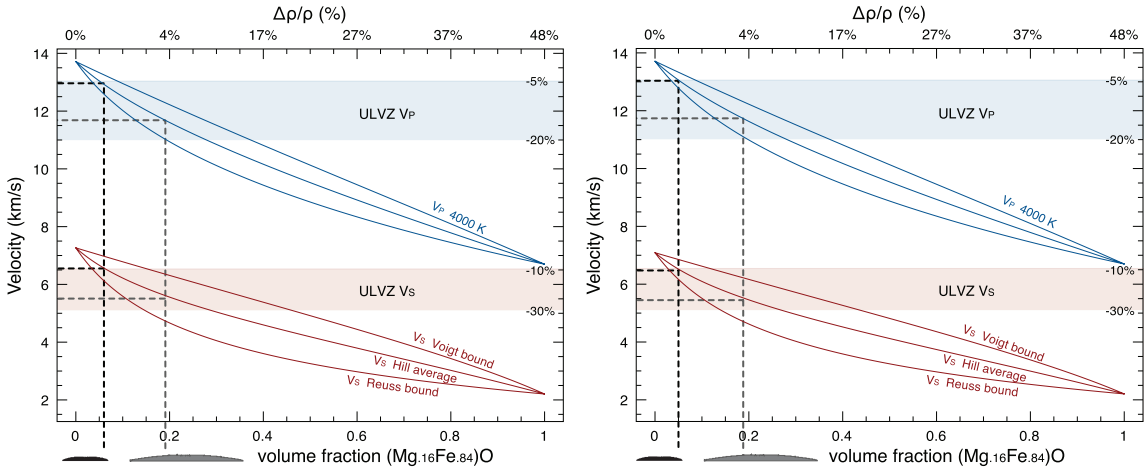

Figure 5.4: Voigt-Reuss-Hill curves of V_P and V_S of the mixing of $(Mg_{.16}Fe_{.84})O$ with PREM (left) and (Mg,Fe)SiO_3-perovskite (right), at T_{CMB} = 4000 K. Assuming an average temperature drop across the CMB thermal boundary layer of ΔT_{CMB} = 1500K (*Tackley*, 2012), ULVZs with moderate velocity drops are consistent with 5% (Mg,Fe)O, and are consistent with smaller structures with high aspect ratio from *Bower et al.* (2011). ULVZs with larger velocity drops are consistent with $\sim$ 20% (Mg,Fe)O, and are consistent with wider, flatter structures. At a CMB temperature of 4000 K, the ULVZ shapes predicted by PREM vs perovskite are indistinguishable (left and right panels, respectively).

content of a (Mg,Fe)O+Pv assemblage is too dense to explain ULVZs at cool temperatures, but adequately explains ULVZs at high temperatures (*Bower et al.*, 2011). Knowing both the absolute temperature and the temperature drop across the thermal boundary layer would allow us to compare different scenarios as a function of density.

Further studies on the mineral properties of mantle phases at high temperature are also required. One example is the extrapolation of sound velocities with temperature. Very few studies exist that measure the velocity derivatives of MgO at high temperature, and none exist in the iron-bearing system. The velocity derivatives we used, measured up to 20 GPa and 1650 K, $\partial V_P/\partial T = -4.64\times10^{-4}$ (km $s^{-1}K^{-1}$) and $\partial V_S/\partial T = -3.85\times10^{-4}$ (km $s^{-1}K^{-1}$) (*Kono et al.*, 2010), are slightly lower than those measured on MgO at room pressure, $\partial V_P/\partial T = -6\times10^{-4}$ (km $s^{-1}K^{-1}$) and $\partial V_S/\partial T = -5\times10^{-4}$ (km $s^{-1}K^{-1}$) (*Sinogeikin et al.*, 2000). Applying these velocity derivatives at

121 GPa is likely overestimating the velocity drop with temperature. The effect of applying these velocity derivatives to iron-rich (Mg,Fe)O rather than MgO is unknown.

5.2 Conclusions

In this work, we have experimentally determined the room temperature sound velocities of $(Mg_{0.16}Fe_{0.84})O$ and $(Mg_{0.06}Fe_{0.94})O$ as a function of pressure up to 121 GPa. We found that the trend in sound velocities was very strongly affected by magnetic transitions: by monitoring the magnetic state using synchrotron Mössbauer spectroscopy, we identified softening in the shear elastic properties of iron-rich (Mg,Fe)O preceding a magnetic transition.

We have also presented the pressure-volume-temperature equation of state of $(Mg_{0.06}Fe_{0.94})O$ up to 115 GPa and 1900 K, measured both with and without an in-situ Fe buffer, and showed that we could not conclusively distinguish the two equations of state. This result is consistent with other studies of the (Mg,Fe)O solid solution that propose pressure-induced exsolution of Fe^{3+}, essentially "self-buffering" (*Zhang and Zhao*, 2005; *McCammon et al.*, 1998). This result is important for practical reasons, as future high-temperature NRIXS studies will not need to have an in-situ buffer.

The work we have completed forms the foundation for future experiments at high temperature. The room temperature sound velocities as a function of pressure form the reference curve for high temperature comparison, and the equation of state as a function of pressure and temperature is required to determined in-situ pressure of a high temperature velocity measurement.

We combined the sound velocities and P-V-T equation of state to predict the properties of iron-rich (Mg,Fe)O at high temperature, and made mixing models to predict the properties of example phase assemblages. Our overall conclusion, with different choices of mixing model, stayed the same: mixing small amounts of iron-rich (Mg,Fe)O with mantle silicate reproduces the characteristic sound velocities and shapes of ultralow-velocity zones.

Bibliography

Akahama, Y., and H. Kawamura (2006), Pressure calibration of diamond anvil Raman gauge to 310 GPa, *J. Appl. Phys.*, *100*(4), 043,516, doi: 10.1063/1.2335683.

Angel, R. J. (2000), Equations of state, *High-Temperature and High-Pressure Crystal Chemistry, Rev. Mineral. Geochem*, *41*(1), 35–59, doi: 10.2138/rmg.2000.41.2.

Angel, R. J., and J. M. Jackson (2002), Elasticity and equation of state of orthoenstatite, $MgSiO_3$, *Am. Mineral.*, *87*(4), 558–561.

Auzende, A. L., J. Badro, F. J. Ryerson, P. K. Weber, S. J. Fallon, A. Addad, J. Siebert, and G. Fiquet (2008), Element partitioning between magnesium silicate perovskite and ferropericlase: New insights into bulk lower-mantle geochemistry, *Earth Planet. Sci. Lett.*, *269*(1-2), 164–174, doi: 10.1016/j.epsl.2008.02.001.

Berryman, J. G. (2000), Seismic velocity decrement ratios for regions of partial melt in the lower mantle, *Geophys. Res. Lett.*, *27*(3), 421–424, doi: 10.1029/1999GL008402.

Bower, D. J., J. K. Wicks, M. Gurnis, and J. M. Jackson (2011), A geodynamic and mineral physics model of a solid-state ultralow-velocity zone, *Earth Planet. Sci. Lett.*, *303*, 193–202, doi: 10.1016/j.epsl.2006.11.025.

Buffett, B. A., E. J. Garnero, and R. Jeanloz (2000), Sediments at the Top of Earth's Core, *Science*, *290*, 1338–1342, doi: 10.1126/science.290.5495.1338.

Catalli, K., S.-H. Shim, and V. Prakapenka (2009), Thickness and Clapeyron slope of the post-perovskite boundary, *Nature*, *462*, 782–786, doi: 10.1038/nature08598.

Chen, B., J. M. Jackson, W. Sturhahn, D. Zhang, J. Zhao, J. K. Wicks, and C. A. Murphy (2012), Spin crossover equation of state and sound velocities of ($Mg_{0.65}Fe_{0.35}$) O ferropericlase to 140 GPa, *J. Geophys. Res.*, *117*(B8), doi: 10.1029/2012JB009162.

Crowhurst, J. C., J. M. Brown, A. F. Goncharov, and S. D. Jacobsen (2008), Elasticity of (Mg, Fe) O through the Spin Transition of Iron in the Lower Mantle, *Science*, *319*(5862), 451–453, doi: 10.1126/science.1149606.

Dewaele, A., P. Loubeyre, F. Occelli, M. Mezouar, P. I. Dorogokupets, and M. Torrent (2006), Quasihydrostatic Equation of State of Iron above 2 Mbar, *Phys. Rev. Lett.*, *97*, 215,504, doi: 10.1103/PhysRevLett.97.215504.

Dewaele, A., F. Datchi, P. Loubeyre, and M. Mezouar (2008), High-pressure–high-temperature equations of state of neon and diamond, *Phys. Rev. B*, *77*, 094,106, doi: 10.1103/PhysRevB.77.094106.

Dewaele, A., A. B. Belonoshko, G. Garbarino, F. Occelli, P. Bouvier, M. Hanfland, and M. Mezouar (2012), High-pressure–high-temperature equation of state of KCl and KBr, *Phys. Rev. B*, *85*(21), 214,105, doi: 10.1103/PhysRevB.85.214105.

Dubrovinsky, L. S., and S. K. Saxena (1997), Thermal expansion of periclase (MgO) and tungsten (W) to melting temperatures, *Phys. Chem. Min.*, *24*(8), 547–550, doi: 10.1007/s002690050070.

Duffy, T. S., and T. K. Ahrens (1993), Thermal expansion of mantle and core materials at very high pressures, *Geophys. Res. Lett.*, *20*(11), 1103–1106, doi: 10.1029/93GL00479.

Duffy, T. S., and Y. Wang (1998), Pressure-volume-temperature equations of state, *Reviews in Mineralogy and Geochemistry*, *37*(1), 425–457.

Dziewonski, A. M., and D. L. Anderson (1981), Preliminary reference Earth model, *Phys. Earth Planet. Inter.*, *25*(4), 297–356, doi: 10.1016/0031-9201(81)90046-7.

Fei, Y. ., L. Zhang, A. Corgne, H. Watson, R. A., Y. Meng, and V. Prakapenka (2007a), Phase

transition and metallization of FeO at high pressures and temperatures, *Geophys. Res. Lett.*, *34*, L17,307, doi: 10.1029/2007GL030712.

Fei, Y., and H.-k. Mao (1994), In Situ Determination of the NiAs Phase of FeO at High Pressure and Temperature, *Science*, *266*(5191), 1678–1680, doi: 10.1126/science.266.5191.1678.

Fei, Y., H.-k. Mao, J. Shu, and J. Hu (1992), P–V–T Equation of State of Magnesiowüstite $(Mg_{0.6}Fe_{0.4})O$, *Phys. Chem. Min.*, *18*, 416–422, doi: 10.1007/BF00200964.

Fei, Y., A. Ricolleau, M. Frank, K. Mibe, G. Shen, and V. Prakapenka (2007b), Toward an internally consistent pressure scale, *Proc. Natl. Acad. of Sci.*, *104*(22), 9182–9186, doi: 10.1073/pnas.0609013104.

Fischer, R. A., and A. J. Campbell (2010), High-pressure melting of wüstite, *Am. Mineral.*, *95*, 1473–1477, doi: 10.2138/am.2010.3463.

Fischer, R. A., A. J. Campbell, O. T. Lord, G. A. Shofner, P. Dera, and V. B. Prakapenka (2011a), Phase transition and metallization of FeO at high pressures and temperatures, *Geophys. Res. Lett.*, *38*, L24,301, doi: 10.1029/2011GL049800.

Fischer, R. A., A. J. Campbell, G. A. Shofner, O. T. Lord, P. Dera, and V. B. Prakapenka (2011b), Equation of state and phase diagram of FeO, *Earth Planet. Sci. Lett.*, *304*, 496–502, doi: 10.1016/j.epsl.2011.02.025.

Frost, D. J., C. Liebske, F. Langenhorst, C. A. McCammon, R. G. Trønnes, and D. C. Rubie (2004), Experimental evidence for the existence of iron-rich metal in the Earth's lower mantle, *Nature*, *428*(6981), 409–412, doi: 10.1038/nature02413.

Frost, D. J., Y. Asahara, D. C. Rubie, E. Ohtani, M. Miyahara, and T. Sakai (2010), Partitioning of oxygen between the Earth's mantle and core, *J. Geophys. Res.*, *115*, B02,202, doi: 10.1029/2009JB006302.

Fujii, A., T. Kondo, T. Taniguchi, and T. Sakaiya (2011), Néel transition in (Mg,Fe)O: A possible change of magnetic structure, *Am. Mineral.*, *96*, 329–332, doi: 10.2138/am.2011.3534.

Fultz, B., and J. Howe (2008), *Transmission Electron Microscopy and Diffractometry of Materials*, Springer.

Glazyrin, K., L. Dubrovinsky, S. Klotz, M. Uhlarz, J. Wosnitza, T. Hansen, and N. Dubrovinskaia (2011), Effect of composition and pressure on phase transitions in Fe_xO at low temperature, *J. Appl. Phys.*, *110*, 026,109, doi: 10.1063/1.3605553.

Hammersley, A. O., S. O. Svensson, M. Hanfland, A. N. Fitch, and D. Hausermann (1996), Two-dimensional detector software: from real detector to idealized image or two-theta scan, *High Press. Res.*, *14*, 235–248, doi: 10.1016/j.pepi.2008.07.033.

Heinz, D., and R. Jeanloz (1987), Temperature measurements in the laser-heated diamond cell, *High-Pressure Research in Mineral Physics*, pp. 113–127, doi: 10.1029/GM039p0113.

Hernlund, J., and A. M. Jellinek (2010), Dynamics and structure of a stirred partially molten ultralow-velocity zone, *Earth Planet. Sci. Lett.*, *296*, 1–8, doi: 10.1016/j.epsl.2010.04.027.

Hernlund, J., and P. Tackley (2007), Some dynamical consequences of partial melting in Earth's deep mantle, *Phys. Earth Planet. Inter.*, *162*(1-2), 149–163, doi: 10.1016/j.pepi.2007.04.005.

Hier-Majumder, S., and M. E. Abbott (2010), Influence of dihedral angle on the seismic velocities in partially molten rocks, *Earth Planet. Sci. Lett.*, *299*, 23–32, doi: 10.1016/j.epsl.2010.08.007.

Holland, T. J. B., and S. A. T. Redfern (1997), Unit cell refinement from powder diffraction data: the use of regression diagnostics, *Mineral. Mag.*, *61*, 65–77.

Idehara, K., A. Yamada, and D. Zhao (2007), Seismological constraints on the ultralow velocity zones in the lowermost mantle from core-reflected waves, *Phys. Earth Planet. Inter.*, *165*(1), 25–46, doi: 10.1016/j.pepi.2007.07.005.

Irifune, T. (1994), Absence of an aluminous phase in the upper part of the Earth's lower mantle, *Nature*, *370*, 131–133, doi: 10.1038/370131a0.

Jackson, J. M., E. A. Hamecher, and W. Sturhahn (2009), Nuclear resonant X-ray spectroscopy of (Mg,Fe)SiO_3 orthoenstatites, *Eur. J. Min.*, *21*(3), 551, doi: 10.1127/0935-1221/2009/0021-1932.

Jacobsen, S. D., H.-J. Reichmann, H. Spetzler, S. J. Mackwell, J. R. Smyth, R. J. Angel, and C. A. McCammon (2002), Structure and elasticity of single-crystal (Mg,Fe)O and a new method of generating shear waves for gigahertz ultrasonic interferometry, *J. Geophys. Res.*, *107*(2), 5867–5871, doi: 10.1029/2001JB000490.

Jacobsen, S. D., H. Spetzler, H. J. Reichmann, and J. R. Smyth (2004), Shear waves in the diamond-anvil cell reveal pressure-induced instability in (Mg,Fe)O, *Proc. Natl. Acad. of Sci.*, *101*(16), 5867–5871, doi: 10.1073/pnas.0401564101.

Jacobsen, S. D., J. F. Lin, R. J. Angel, G. Shen, V. B. Prakapenka, P. Dera, H.-k. Mao, and R. J. Hemley (2005), Single-crystal synchrotron X-ray diffraction study of wüstite and magnesiowüstite at lower-mantle pressures, *J. Synchrotron Rad.*, *12*, 577–583, doi: 0.1107/S0909049505022326.

Kanda, R., and D. Stevenson (2006), Suction mechanism for iron entrainment into the lower mantle, *Geophys. Res. Lett.*, *33*(2), L02,310, doi: 10.1029/2005GL025009.

Kantor, A., L. S. Dubrovinsky, N. A. Dubrovinskaia, I. Y. Kantor, and I. N. Goncharenko (2005), Phase transitions in MnO and FeO at low temperatures: A neutron powder diffraction study, *J. Alloys Compounds*, *402*, 42–45, doi: 10.1016/j.jallcom.2005.04.155.

Kantor, I., L. Dubrovinsky, C. McCammon, A. Kantor, S. Pascarelli, G. Aquilanti, W. Crichton, M. Mattesini, R. Ahuja, J. Almeida, and V. Urusov (2006), Pressure-induced phase transition in $Mg_{0.8}Fe_{0.2}O$ ferropericlase, *Phys. Chem. Min.*, *33*, 35–44, doi: 10.1007/s00269-005-0052-z.

Kantor, I. Y., C. A. McCammon, and L. S. Dubrovinsky (2004), Mössbauer spectroscopic study of pressure-induced magnetisation in wüstite (FeO), *J. Alloys Compounds*, *376*, 5–8, doi: 10.1016/j.jallcom.2003.11.159.

Kiefer, B., L. Stixrude, and R. Wentzcovitch (2002), Elasticity of (Mg,Fe)SiO_3-perovskite at high pressures, *Geophys. Res. Lett.*, *29*(11), 34–1, doi: 10.1029/2002GL014683.

Knittle, E., and R. Jeanloz (1991), Earth's Core-Mantle Boundary—Results of Experiments at High Pressures and Temperatures, *Science*, *251*(5000), 1438–1443, doi: 10.1126/science.251.5000.1438.

Kondo, T., E. Ohtani, N. Hirao, T. Yagi, and T. Kikegawa (2004), Phase transitions of (Mg,Fe)O at megabar pressures, *Phys. Earth Planet. Inter.*, *143-144*, 201–213, doi: 10.1016/j.pepi.2003.10.008.

Kono, Y., T. Irifune, Y. Higo, T. Inoue, and A. Barnhoorn (2010), P-V-T relation of MgO derived by simultaneous elastic wave velocity and in situ X-ray measurements: A new pressure scale for the mantle transition region, *Phys. Earth Planet. Inter.*, *183*(1), 196–211, doi: 10.1016/j.pepi.2010.03.010.

Labrosse, S., J. Hernlund, and N. Coltice (2007), A crystallizing dense magma ocean at the base of the Earth's mantle, *Nature*, *450*(7171), 866–869, doi: 10.1038/nature06355.

Lay, T., E. J. Garnero, and Q. Williams (2004), Partial melting in a thermo-chemical boundary layer at the base of the mantle, *Phys. Earth Planet. Inter.*, *146*(3-4), 441–467, doi: doi:10.1016/j.pepi.2004.04.004.

Lay, T., J. Hernlund, and B. A. Buffett (2008), Core-mantle boundary heat flow, *Nature Geosci.*, *1*, doi: 10.1038/ngeo.2007.44.

Li, B., and J. Zhang (2005), Pressure and temperature dependence of elastic wave velocity of $MgSiO_3$ perovskite and the composition of the lower mantle, *Phys. Earth Planet. Inter.*, *151*(1), 143–154, doi: 10.1016/j.pepi.2005.02.004.

Lin, J. F., D. L. Heinz, H. Mao, R. J. Hemley, J. M. Devine, J. Li, and G. Shen (2003), Stability of magnesiowüstite in Earth's lower mantle, *Proc. Natl. Acad. of Sci.*, *100*(8), 4405–4408, doi: 10.1073/pnas.252782399.

Manga, M., and R. Jeanloz (1996), Implications of a metal-bearing chemical boundary layer in D" for mantle dynamics, *Geophys. Res. Lett.*, *23*(22), 3091–3094, doi: 10.1029/96GL03021.

Mao, H. K., P. M. Bell, J. W. Shaner, and D. J. Steinberg (1978), Specific volume measurements of Cu, Mo, Pd, and Ag and calibration of the ruby R_1 fluorescence pressure gauge from 0.06 to 1 Mbar, *J. Appl. Phys.*, *49*(6), 3276–3283, doi: 10.1063/1.325277.

Mao, H. K., J. Xu, and P. M. Bell (1986), Calibration of the ruby pressure gauge to 800 kbar under quasi-hydrostatic conditions, *J. Geophys. Res.*, *91*(B5), 4673–4676, doi: 10.1029/JB091iB05p04673.

Mao, H.-k., J. Shu, Y. Fei, J. Hu, and R. J. Hemley (1996), The wüstite enigma, *Physics of the earth and planetary interiors*, *96*(2), 135–145, doi: 10.1016/0031-9201(96)03146-9.

Mao, W., J. Shu, J. Hu, R. Hemley, and H. k. Mao (2002), Displacive transition in magnesiowüstite, *J. Phys.: Condens. Matter*, *14*, 11,349, doi: 10.1088/0953-8984/14/44/480.

Mao, W. L., H. Mao, W. Sturhahn, J. Zhao, V. B. Prakapenka, Y. Meng, J. Shu, Y. Fei, and R. J. Hemley (2006), Iron-Rich Post-Perovskite and the Origin of Ultralow-Velocity Zones, *Science*, *312*(5773), 564–565, doi: 10.1126/science.1123442.

McCammon, C., J. Peyronneau, and J.-P. Poirier (1998), Low ferric iron content of (Mg,Fe)O at high pressures and temperatures, *Geophys. Res. Lett.*, *25*(10), 1589–1592, doi: 10.1029/98GL01178.

McCammon, C. A., and L.-g. Liu (1984), The Effects of Pressure and Temperature on Nonstoichiometric Wüstite, Fe_xO: The Iron-rich Phase Boundary, *Phys. Chem. Min.*, *10*, 106–113, doi: 10.1007/BF00309644.

McNamara, A. K., E. J. Garnero, and S. Rost (2010), Tracking deep mantle reservoirs with ultra-low velocity zones, *Earth Planet. Sci. Lett.*, *299*(1), 1–9, doi: 10.1016/j.epsl.2010.07.042.

Murakami, M., K. Hirose, N. Sata, and Y. Ohishi (2005), Post-perovskite phase transition and mineral chemistry in the pyrolitic lowermost mantle, *Geophys. Res. Lett.*, *32*(3), L03,304, doi: 10.1029/2004GL021956.

Murakami, M., Y. Ohishi, N. Hirao, and K. Hirose (2009), Elasticity of MgO to 130 GPa: Implications for lower mantle mineralogy, *Earth Planet. Sci. Lett.*, *277*(1-2), 123–129, doi: 10.1016/j.epsl.2008.10.010.

Murphy, C. A., J. M. Jackson, W. Sturhahn, and B. Chen (2011), Melting and thermal pressure of

hcp-Fe from the phonon density of states, *Phys. Earth Planet. Inter.*, *188*, 114–120, doi: 10.1016/j.pepi.2011.07.001.

Nomura, R., H. Ozawa, S. Tateno, K. Hirose, J. Hernlund, S. Muto, H. Ishii, and N. Hiraoka (2011), Spin crossover and iron-rich silicate melt in the Earths deep mantle, *Nature*, *473*, 199–203, doi: 10.1038/nature09940.

Ozawa, H., K. Hirose, S. Tateno, N. Sata, and Y. Ohishi (2010), Phase transition boundary between B1 and B8 structures of FeO up to 210 GPa, *Phys. Earth Planet. Inter.*, *179*, 1157–163, doi: 10.1016/J.pepi.2009.11.005.

Ozawa, H., K. Hirose, K. Ohta, H. Ishii, N. Hiraoka, Y. Ohishi, and Y. Seto (2011), Spin crossover, structural change, and metallization in NiAs-type FeO at high pressure, *Phys. Rev. B*, *84*, 134,417, doi: 10.1103/PhysRevB.84.134417.

Prakapenka, V. B., A. Kuba, A. Kuznetsov, A. Kaskin, O. Shkurikhin, P. Dera, M. L. Rivers, and S. R. Sutton (2008), Advanced flat top laser heating system for high pressure research at GSECARS: application to the melting behavior of germanium, *High Press. Res.*, *28*, 225–235, doi: 10.1080/08957950802050718.

Richet, P., H.-k. Mao, and P. M. Bell (1989), Bulk Moduli of Magnesiowüstites From Static Compression Measurements, *J. Geophys. Res.*, *94*(B3), 3037–3045, doi: 10.1029/JB094iB03p03037.

Rivers, M., V. B. Prakapenka, A. Kubo, C. Pullins, C. M. Holl, and S. D. Jacobsen (2008), The COMPRES/GSECARS gas-loading system for diamond anvil cells at the Advanced Photon Source, *High Press. Res.*, *28*, 273–292, doi: 10.1080/08957950802333593.

Rost, S., E. J. Garnero, and Q. Williams (2006), Fine-scale ultralow-velocity zone structure from high-frequency seismic array data, *J. Geophys. Res.*, *111*, B09,310, doi: 10.1029/2005JB004088.

Sakai, T., E. Ohtani, H. Terasaki, N. Sawada, Y. Kobayashi, M. Miyahara, M. Nishijima, N. Hirao, Y. Ohishi, and T. Kikegawa (2009), Fe-Mg partitioning between perovskite and ferropericlase in the lower mantle, *American Mineralogist*, *94*(7), 921, doi: 10.2138/am.2009.3123.

Shen, G., M. L. Rivers, Y. Wang, and S. R. Sutton (2001), Laser heated diamond cell system at the Advanced Photon Source for *in situ* x-ray measurements at high pressure and temperature, *Rev. Sci. Instrum.*, *72*(2), 1273–1282, doi: doi:10.1063/1.1343867.

Shu, J., H.-k. Mao, J. Hu, Y. Fei, and R. J. Hemley (1998a), Single-Crystal X-ray Diffraction of Wüstite to 30 GPa Hydrostatic Pressure, *N. Jb. Miner. Abh.*, *172*(2/3), 309–323.

Shu, J., H.-k. Mao, J. Hu, Y. Fei, and R. J. Hemley (1998b), High-Pressure Phase Transition in Magnesiowustite $(Fe_{1-x}Mg_x)O$, in *Eos Trans. Am. Geophys. Union*, *Spring Meeting Suppl.*, vol. 79 (17), abstr. M21A-01.

Sidorin, I., M. Gurnis, and D. V. Helmberger (1999), Evidence for a Ubiquitous Seismic Discontinuity at the Base of the Mantle, *Science*, *286*, 1326–1331, doi: 10.1126/science.286.5443.1326.

Sinmyo, R., K. Hirose, D. Nishio-Hamane, Y. Seto, K. Fujino, N. Sata, and Y. Ohishi (2008), Partitioning of iron between perovskite/postperovskite and ferropericlase in the lower mantle, *J. Geophys. Res.*, *113*(B11), B11,204, doi: 10.1029/2008JB005730.

Sinmyo, R., K. Hirose, S. Muto, Y. Ohishi, and A. Yasuhara (2011), The valence state and partitioning of iron in the Earths lowermost mantle, *J. Geophys. Res.*, *116*, B07,205, doi: 10.1029/2010JB008179.

Sinogeikin, S. V., J. M. Jackson, B. O'Neill, J. W. Palko, and J. D. Bass (2000), Compact high-temperature cell for Brillouin scattering measurements, *Rev. Sci. Instrum.*, *71*, 201, doi: 10.1063/1.1150183.

Song, X., and T. J. Ahrens (1994), Pressure-temperature range of reactions between liquid iron in the outer core and mantle silicates, *Geophys. Res. Lett.*, *21*(2), doi: 10.1029/93GL03262.

Speziale, S., A. Milner, V. E. Lee, S. M. Clark, M. P. Pasternak, and R. Jeanloz (2005), Iron spin transition in Earth's mantle, *Proc. Natl. Acad. of Sci.*, *102*(50), 17,918–17,922, doi: 10.1073/pnas.0508919102.

Struzhkin, V. V., H. Mao, J. Hu, M. Schwoerer-Böhning, J. Shu, R. J. Hemley, W. Sturhahn, M. Y. Hu, E. E. Alp, P. Eng, and G. Shen (2001), Nuclear Inelastic X-ray Scattering of FeO to 48 GPa, *Earth-Science Reviews*, *110*, 1–25, doi: 10.1103/PhysRevLett.87.255501.

Sturhahn, W. (2000), CONUSS and PHOENIX: Evaluation of nuclear resonant scattering data, *Hyperfine Interactions*, *125*(1-4), 149–172, doi: 10.1023/A:1012681503686.

Sturhahn, W. (2004), Nuclear resonant spectroscopy, *J. Phys. Condens. Matter*, *16*(5), 497–530, doi: 10.1088/0953-8984/16/5/009.

Sturhahn, W., and J. M. Jackson (2007), Geophysical applications of nuclear resonant spectroscopy, *GSA Special Papers*, *421*, 157, doi: 10.1130/2007.2421(09).

Tackley, P. J. (2012), Dynamics and evolution of the deep mantle resulting from thermal, chemical, phase and melting effects, *Earth-Science Reviews*, *110*, 1–25, doi: 10.1016/j.earscirev.2011.10.001.

Takafuji, N., K. Hirose, M. Mitome, and Y. Bando (2005), Solubilities of O and Si in liquid iron in equilibrium with (Mg,Fe)SiO_3 perovskite and the light elements in the core, *Geophys. Res. Lett.*, *32*, L06,313, doi: 10.1029/2005GL022773.

Thomas, C. W., Q. Liu, C. B. Agee, P. D. Asimow, and R. A. Lange (2012), Multi-technique equation of state for Fe_2SiO_4 melt and the density of Fe-bearing silicate melts from 0 to 161 GPa, *J. Geophys. Res.*, *117*, B10,206, doi: 10.1029/2012JB009403.

Thorne, M. S., and E. J. Garnero (2004), Inferences on ultralow-velocity zone structure from a global analysis of *SPdKS* waves, *J. Geophys. Res.*, *109*, doi: 10.1029/2004JB003010.

Toellner, T., M. Hu, W. Sturhahn, G. Bortel, E. Alp, and J. Zhao (2001), Crystal monochromator with a resolution beyond 10^8, *J. Synchrotron Radiat.*, *8*(4), 1082–1086, doi: 10.1107/S0909049501007257.

Watt, J. P., G. F. Davies, and R. J. O'Connell (1976), The Elastic Properties of Composite Materials, *Rev. Geophys.*, *14*(4), 541–563, doi: 10.1029/RG014i004p00541.

Wen, L., and D. V. Helmberger (1998), Ultra-low velocity zones near the core-mantle boundary from broadband PKP precursors, *Science*, *279*(5357), 1701–1703, doi: 10.1126/science.279.5357.1701.

Westrenen, W. v., J. Li, Y. Fei, M. R. Frank, H. Hellwig, T. Komabayashi, K. Mibe, W. G. Minarik, J. A. V. Orman, H. C. Watson, K.-i. Funakoshi, and M. W. Schmidt (2005), Thermoelastic properties of $(Mg_{0.64}Fe_{0.36})O$ ferropericlase based on in situ X-ray diffraction to 26.7 GPa and 2173 K, *Phys. Earth Planet. Inter.*, *151*, 163–176, doi: 10.1016/j.pepi.2005.03.001.

Wicks, J. K., J. M. Jackson, and W. Sturhahn (2010), Very low sound velocities in iron-rich (Mg,Fe)O: Implications for the core-mantle boundary region, *Geophys. Res. Lett.*, *37*, L15,304, doi: 10.1029/2010GL043689.

Williams, Q., and E. Garnero (1996), Seismic evidence for partial melt at the base of Earth's mantle, *Science*, *273*(5281), 1528, doi: 10.1126/science.273.5281.1528.

Williams, Q., J. Revenaugh, and E. Garnero (1998), A Correlation Between Ultra-Low Basal Velocities in the Mantle and Hot Spots, *Science*, *281*(5376), 546, doi: 10.1126/science.281.5376.54.

Wimert, J., and S. Hier-Majumder (2012), A three-dimensional microgeodynamic model of melt geometry in the Earth's deep interior, *J. Geophys. Res.*, *117*, doi: 10.1029/2011JB009012.

Yagi, T., T. Suzuki, and A. S.-i. (1985), Static Compression of Wüstite ($Fe_{0.98}O$) to 120 GPa, *J. Geophys. Res.*, *90*(B10), 8784–8788, doi: 10.1029/JB090iB10p08784.

Zhang, J. (2000), Effect of pressure on the thermal expansion of MgO up to 8.2 GPa, *Phys. Chem. Min.*, *27*, 145–148, doi: 10.1007/s002690050001.

Zhang, J., and P. Kostak Jr (2002), Thermal equation of state of magnesiowüstite $(Mg_{0.6}Fe_{0.4})O$, *Phys. Earth Planet. Inter.*, *129*(3), 301–311, doi: 10.1016/S0031-9201(01)00296-5.

Zhang, J., and Y. Zhao (2005), Effects of defect and pressure on the thermal expansivity of Fe_XO, *Phys. Chem. Min.*, *32*, 241–247, doi: 10.1007/s00269-005-0447-x.

Zhuravlev, K. K., J. M. Jackson, A. S. Wolf, J. K. Wicks, J. Yan, and S. M. Clark (2010), Isothermal compression behavior of (Mg,Fe)O using neon as a pressure medium, *Phys. Chem. Min.*, *37*, 465–474, doi: 10.1007/s00269-009-0347-6.

Appendix A

A.1 Synthesis and Characterization

A.1.1 $(Mg_{0.16}Fe_{0.84})O$

MgO was dried at 1100°C overnight, then stoichiometrically combined with 95% enriched $^{57}Fe_2O_3$ (Advanced Materials Techonologies Ltd.) to produce an Fe/(Mg+Fe) ratio of 0.85. After being ground in an agate mortar, the oxide mixture was pressed into a pellet and reduced to form $(Mg,Fe^{2+})O$ in a gas-mixing 1 atm furnace. The pellet was equilibrated at 1400°C for two runs of 20 hours each just above the iron-wüstite fugacity buffer (an oxygen potential of $10^{-9.6}$ atm). Sample composition and homogeneity were measured using a JEOL JXA-8200 electron microprobe $(Mg_{.158(2)}\ Fe_{.842(2)})O$, where the number in parentheses is the error on the last digit and the oxygen is assumed to be stoichiometric. Ambient pressure unit cell volume was measured with X-ray diffraction (9.79(4) Å/atom), resulting in a density determination of 5.69(7) g/cm^3. The magnetic signature of iron in our sample was determined by Mössbauer analysis at ambient pressure (Figure 2.6). The absence of a magnetically ordered component indicates that our sample is free of metallic iron and magnetite. Although the black color of the sample indicates that there may be trace amounts of trivalent iron, its concentration is below detection limits of Mössbauer (less than 3%). This will translate to vacancy concentrations of 0-3%, which we include in the density error bar.

In June 2012, a re-measurement of the sample composition revealed the presence of Ti contamination in the sample, previously missed. A revised chemical formula is $(Mg_{0.18}Fe_{0.78}Ti_{0.04})O$, which would correspond to a revised density of 5.7(1) g/cm^3. With likely errors on each subscript to be

0.01, a more thorough analysis is required to reduce the error bars.

A.1.2 $(Mg_{0.06}Fe_{0.94})O$

$(Mg_{0.06}Fe_{0.94})O$ was synthesized by the same methods as above, using ^{57}Fe metal from Isoflex. Microprobe analysis of the synthesized material gives a sample composition of $(Mg_{.0580(9)}Fe_{.9420(9)}Si_{.0021(9)})O$, assuming that the oxygen is stoichiometric. A conventional Mössbauer spectrum (Figure 2.3) taken of the synthesized sample is consistent with divalent iron, and shows no indication of Fe^{3+}. A secondary electron image (Figure A.1) taken of the sample before microprobe analysis shows no indication of compositional heterogeneities.

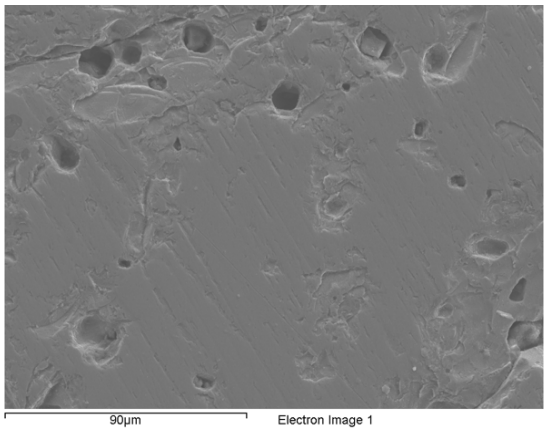

Figure A.1: Secondary electron image of $(Mg_{0.06}Fe_{0.94})O$.

A.1.3 $Fe_{1-x}O$

$Fe_{1-x}O$ was synthesized in March 2011 using the methods above, at 1300°C, a lower temperature to account for the melting point of FeO of 1395°C. The synthesis was carried out twice, using both the $^{57}Fe_2O_3$ source and the ^{57}Fe metal source, as it had been determined that the $^{57}Fe_2O_3$ source was contaminated with Ti. The aim of synthesizing with and without Ti was to determine whether or not the vibrational spectra and subsequent sound velocities were affected by the presence of minor Ti. Room pressure lattice parameter and density are listed in Table A.3.

A.2 Additional Thermodynamic Parameters

Key thermodynamic information can be directly derived from the partial projected Phonon Density of States using the PHOENIX software (*Sturhahn*, 2000, www.nrixs.com). More detailed descriptions can be found in *Sturhahn* (2004).

A.2.1 $(Mg_{0.16}Fe_{0.84})O$

$Pressure^a$ (GPa)	f_{LM}	E_K (meV/atom)	D_{av} (N/m)	$f_{LM,Z}$	$E_{K,Z}$ (meV/atom)	C_{vib} (k_B/atom)	S_{vib} (k_B/atom)
0	0.7129(8)	14.0(1)	145(5)	0.9069(3)	6.15(9)	2.75(1)	3.57(1)
4.0(3)	0.717(2)	14.0(2)	145(11)	0.9071(7)	6.1(2)	2.8(3)	3.59(3)
11.4(3)	0.713(2)	14.1(3)	169(10)	0.9090(8)	6.3(2)	2.74(4)	2.45(2)
15(3)	0.731(2)	14.2(3)	167(14)	0.9112(8)	6.4(3)	2.73(4)	3.44(3)
21.0(4)	0.727(2)	14.3(3)	183(12)	0.9138(7)	6.7(2)	2.71(3)	3.33(3)
28(2)	0.730(2)	14.2(3)	171(12)	0.9136(8)	6.6(2)	2.72(4)	3.36(3)
41(1)	0.751(2)	14.0(3)	142(14)	0.9153(8)	6.3(2)	2.76(4)	3.36(3)
46(4)	0.778(3)	14.2(3)	177(15)	0.9208(8)	6.9(2)	2.71(4)	3.16(3)
55(3)	0.760(3)	14.2(3)	173(15)	0.9189(9)	6.8(3)	2.72(5)	3.22(3)
65(5)	0.801(3)	14.5(3)	222(12)	0.9263(7)	7.5(2)	2.65(4)	2.95(3)
80(5)	0.814(3)	14.6(3)	229(17)	0.9281(7)	7.7(3)	2.64(4)	2.90(3)
88(4)	0.815(2)	14.9(2)	281(8)	0.9306(5)	8.3(2)	2.59(3)	2.75(2)
97(5)	0.826(2)	15.3(2)	345(13)	0.9336(5)	9.0(2)	2.52(3)	2.61(2)
102(5)	0.834(3)	15.2(4)	326(19)	0.9340(8)	8.8(3)	2.54(4)	2.61(3)
110(4)	0.840(2)	15.4(2)	360(12)	0.9359(4)	9.2(2)	2.50(2)	2.53(2)
121(7)	0.848(2)	15.6(3)	388(16)	0.9377(6)	9.5(2)	2.47(3)	2.45(2)

Table A.1: Thermodynamic parameters calculated directly from the partial-projected phonon density of states of $(Mg_{0.16}Fe_{0.84})O$. ^{a}Pressures were determined from ruby fluorescence before and after the NRIXS measurement, from Table 2.1. f_{LM} is the Lamb-Mössbauer factor. E_K is the kinetic energy per resonant atom. D_{av} is the average force constant of the resonant atom. $f_{LM,Z}$ is the Lamb-Mössbauer factor at zero Kelvin. $E_{K,Z}$ is the kinetic energy per resonant atom at zero Kelvin. C_{vib} is the vibrational specific heat. S_{vib} is the vibrational entropy per atom.

A.2.2 $(Mg_{0.06}Fe_{0.94})O$

$Pressure^a$ (GPa)	f_{LM}	E_K (meV/atom)	D_{av} (N/m)	$f_{LM,Z}$	$E_{K,Z}$ (meV/atom)	C_{vib} (k_B/atom)	S_{vib} (k_B/atom)
0	0.700(1)	14.2(1)	162(5)	0.9076(4)	6.18(8)	2.75(2)	3.57(2)
9.61(2)	0.714(3)	[14.2(3)]	[186(10)]	0.9119(9)	[6.6(2)]	2.72(4)	3.39(4)
42.7(7)	0.773(2)	[14.7(2)]	[261(8)]	0.9237(6)	[7.8(2)]	2.6(3)	2.95(2)
55(1)	0.788(2)	[14.7(2)]	[264(8)]	0.9267(5)	[7.9(1)]	2.61(3)	2.86(2)
64(2)	0.813(2)	[14.8(2)]	[281(8)]	0.9306(5)	[8.3(1)]	2.58(3)	2.73(2)
81.1(8)	0.826(1)	[15.5(2)]	[371(10)]	0.9339(3)	[9.2(1)]	2.50(1)	2.61(1)
81.6(7)	0.828(2)	15.0(2)	300(8)	0.9330(5)	8.6(1)	2.56(2)	2.66(2)

Table A.2: Thermodynamic parameters calculated directly from the partial-projected phonon density of states of $(Mg_{0.06}Fe_{0.94})O$. [a]Pressure determined from in-situ X-ray diffraction, from Table 3.1. f_{LM} is the Lamb-Mössbauer factor. E_K is the kinetic energy per resonant atom. D_{av} is the average force constant of the resonant atom. $f_{LM,Z}$ is the Lamb-Mössbauer factor at zero Kelvin. $E_{K,Z}$ is the kinetic energy per resonant atom at zero Kelvin. C_{vib} is the vibrational specific heat. S_{vib} is the vibrational entropy per atom. E_K and D_{av} reported in brackets denotes values possibly affected by higher energy vibrations not sampled by our limited energy range.

A.3 Sound Velocities of FeO from Nuclear Resonant Inelastic X-ray Scattering

This section describes the determination of FeO Debye velocities presented in Figure 3.12. NRIXS spectra were taken at Sector 3 of the Advanced Photon Source in August 2011 and March 2012. The volume of FeO at ambient pressure was measured at Sector 12.2.2 of the Advanced Light Source. Using the (111), (200) and (220) reflections, the cubic volume was refined using the *Unit Cell* software. The resulting lattice parameter $a = 4.306(1)$ corresponds to a composition of $Fe_{0.941}O$ (*McCammon and Liu*, 1984). The volume of FeO at high pressure was measured at Sector 13-ID-D, GSECARS of the Advanced Photon Source in February 2012. Unit cell volumes at high pressure were determined using the rhombohedral reflections: (003), (101), (012), (104), and (110). Density was calculated assuming 0.5(5)% vacancies.

Figure A.2 shows the raw NRIXS spectra of FeO. At ambient pressure, the energy scan range was -60 $\rightarrow$ +80 meV. At higher pressures, the scan range was increased to -65 $\rightarrow$ +80 meV and -70 $\rightarrow$ +100 meV. The partial projected phonon density of states was extracted for each pressure point using the PHOENIX software (*Sturhahn*, 2000) and are presented in Figure A.3.

As described previously, Debye sound velocities were determined using *psvl*. Table A.3 summarizes the density and Debye sound velocities of FeO in addition to the refined unit cell parameters from X-ray diffraction.

ρ (g/cc)	$E_{min} - E_{max}$ meV	V_D (km/s)	Vol/atom Å^3	a Å	c Å
5.99(6)[a]	3.7 – 16.3[a]	2.87(1)[a]	10.06(2)[a]	4.318(8)[a]	
6.05(2)	3.2 – 17.1	2.88(1)	9.98(4)	4.306(2)	
8.3(1)	4.5 – 14.8	3.73(4)	7.3(1)	2.64(2)	7.26(9)
8.4(1)	4.2 – 19.8	3.88(3)	7.2(1)	2.63(2)	7.21(9)

Table A.3: Summary of FeO density, energy range used to calculate Debye velocities, and Debye velocities. Volume and lattice parameters were refined using the program *Unit Cell* (*Holland and Redfern*, 1997). [a]Density calculated for Ti-containing oxide, estimated to have the chemical formula $(Fe_{0.959}Ti_{0.041(1)})O$ (*Chen et al.*, 2012).

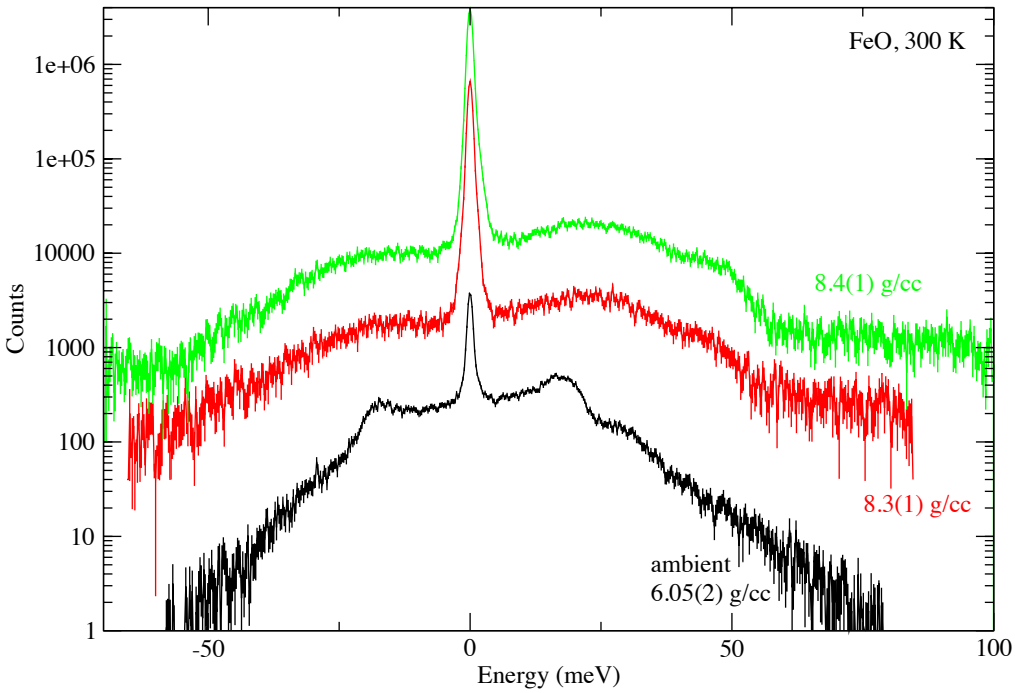

Figure A.2: Raw NRIXS spectra of FeO at 300 K at three pressures.

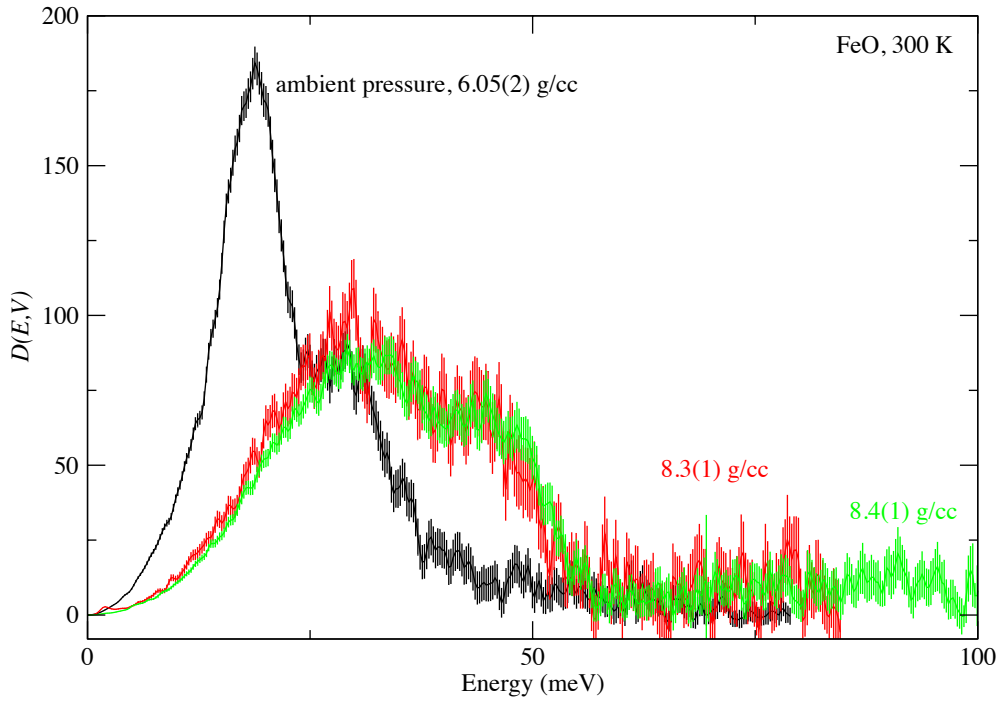

Figure A.3: Partial projected density of states (PDOS) of FeO, extracted from the energy scan using the PHOENIX software (*Sturhahn*, 2000). There is a marked difference in the distribution of vibrations between the ambient pressure spectrum and the high pressure spectra, which is also reflected in the calculated sound velocities. Debye sound velocities determined from the low-energy region of these PDOSs are plotted in Figure 3.12.

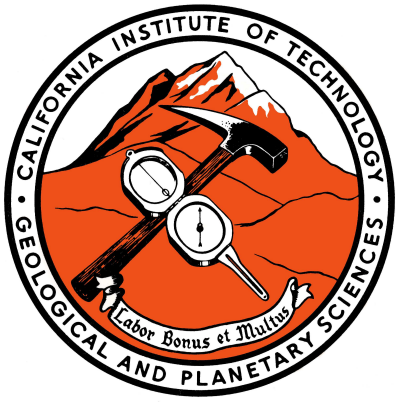
CALIFORNIA INSTITUTE OF TECHNOLOGY
GEOLOGICAL AND PLANETARY SCIENCES
Labor Bonus et Multus